THE MECHANICAL PROPERTIES OF NATIVE PORCINE AORTIC AND PULMONARY HEART VALVE LEAFLETS

by

Thanh Vi Lam

B.S., The Johns Hopkins University, 2001

Submitted to the Graduate Faculty of

School of Engineering in partial fulfillment

of the requirements for the degree of

Master of Science

University of Pittsburgh

2004

UNIVERSITY OF PITTSBURGH

SCHOOL OF ENGINEERING

This thesis was presented

by

Thanh Vi Lam

It was defended on

December 3, 2004

and approved by

Richard Debski, Ph. D., Assistant Professor
Department of Bioengineering

Hai Lin, Ph. D., Assistant Professor
Department of Bioengineering

Thesis Advisor: Michael Sacks, Ph. D., Professor
Department of Bioengineering

MACRO- AND MICROMECHANICAL BEHAVIOR OF THE AORTIC AND PULMONARY HEART VALVE LEAFLETS

Thanh Vi Lam, MS

University of Pittsburgh, 2004

Aortic heart valves and their replacements fail *in vivo* for reasons that are not fully understood. Mechanical evaluation and simulations of the function of native aortic valves and their replacements have been limited to tensile and biaxial tests that seek to quantify the behavior of leaflet tissues as a homogenous whole. However, it is widely understood that valvular tissues are multi-layered structures composed of collagen, elastin, and glycosaminoglycans. The mechanical behavior of these layers within intact valve leaflet tissues and their interactions are unknown. In addition, pulmonary valves have been used as substitutes for diseased aortic valves without any real understanding of the mechanical differences between the aortic and pulmonary valves. The pulmonary valve operates in an environment significantly different than that of the aortic valve and, thus, mechanical behavioral differences between the two valve leaflets may exist. In this study, we sought to determine the mechanical properties of the porcine aortic and pulmonary valves in flexure, and to determine the mechanical relationship between the leaflet layers: the fibrosa, spongiosa, and ventricularis. This was accomplished by developing a novel flexure mechanical testing device that allowed for the determination of the flexural stiffness of the leaflet tissue was determined using Bernoulli-Euler bending. Moreover, transmural strains were quantified and used to determine the location of the neutral axis to determine if differences existed in the layer properties of the fibrosa and ventricularis. To contrast the flexural studies, biaxial experiments were also performed on the aortic and pulmonary valves to determine the mechanical differences in the tensile behavior between the two leaflets.

Results indicated that the pulmonary valve is stiffer than the aortic valve in flexure but less compliant than the aortic valve in biaxial tensile tests. The interactions between the layers of the leaflets suggest an isotropic mechanical response in flexure, but do so through mechanisms that are not fully understood. For heart valve leaflet replacement therapy, this study illustrates the biomechanical differences between the aortic and pulmonary valve leaflets and emphasizes the need to fully characterize the two as separate but related entities. Understanding the interactions of microscopic structures such as collagen and elastin fibers is critical to understanding the response of the tissue as a whole and how all these elements combine to provide a functioning component of the organ system.

TABLE OF CONTENTS

LIST OF TABLES

LIST OF FIGURES

ACKNOWLEDGMENTS

Many thanks are due to the members of the Engineered Tissue Mechanics Lab for their help and assistance in making this project successful. Particularly, I must acknowledge Wei Sun for his help with calculations, Daniel Hildebrand for his advice and help with building the device, Brett Zubiate for his technical assistance, Jon Grashow for his help with Labview, and David Merryman and Jiro Nagatomi for their help with biaxial testing. I also must thank Dr. Hai Lin and Dr. Richard Debski for agreeing to be a part of my committee and providing me with insightful comments and advice regarding my work. Dr. Michael Sacks has been quite the driving force behind this thesis work with his advice, guidance, and financial support. I would like to acknowledge Sarah Russ of St. Jude Medical, Inc. for her assistance in providing me with images of the SJM Regent® and Toronto SPV® valves. Lastly, I must thank Jessica Lin for staying the course and keeping it all in perspective.

1.0 INTRODUCTION

In cardiovascular surgery and regenerative medicine, the search for innovations and improvements in the field is fueled by the 61.8 million adult Americans who suffer from some cardiovascular disease. Of these adults, 19,737 have died from heart valve diseases [1]. To prevent such deaths, research and development has been conducted to treat heart valve disease in adults yielding promising valve substitutes such as bioprosthetic and mechanical valves.

Currently, the treatment of aortic valve disease is usually complete valve replacement. First performed successfully in 1960, surgical replacement of diseased human heart valves by valve prostheses is now commonplace and enhances survival and quality of life for the estimated 75,000 US and 275,000 patients worldwide done annually [2]. However, treatment for children has not received the same attention and most treatments are derived from adult treatments that cannot compensate for factors specific to children such as growth and remodeling. Children under the age of fifteen account for approximately 50% of the 4100 deaths attributed to congenital heart defects in 2001 [1] and of those approximately 3-8% of deaths can be attributed to aortic insufficiency or stenosis [3]. Pediatric cases of heart valve disease are treated through medication and surgical repair before replacement therapy is sought because of the lack of a suitable replacement [4]

The vast majority of prosthetic valve designs are either mechanical prosthesis and bioprosthetic heart valves (BHV). Mechanical prostheses are fabricated from synthetic materials, mainly pyrolytic carbon leaflets mounted in a titanium frame. BHV are fabricated from either porcine aortic valve or bovine pericardium, chemically treated with glutaraldehyde to remove immunogenicity and improve durability, and usually mounted onto a flexible metal frame (stent) which is covered with Dacron to facilitate surgical implementation. BHVs are subject to calcification and long-term durability issues and mechanical valves require chronic anti-coagulant therapy that severely affects the quality of life of the patient and both valves require frequent re-operation to account for patient growth, introducing further complications and morbidity. Improvements in either form of treatment addressing failure issues fails to compensate for a lack of remodeling and growth of the valve with the patient. Thus, most pediatric aortic valve replacements performed are done so using the Ross procedure where the deficient aortic valve is replaced by the patient's pulmonary valve which is usually then replaced with a bioprosthetic valve. Current results with the procedure show good results, however, more research should be conducted to confirm the feasibility of using the pulmonary valve in the aortic position.

The underlying issue with treating valve disease in the pediatric patient is a lack of understanding of the physiology and function of the pulmonary and aortic valves resulting in the absence of a truly acceptable valve replacement. Current replacement strategies that rely upon mechanical or BHV prosthesis technology is insufficient in fulfilling the needs of a growing patient. By expanding knowledge about the pulmonary valve, functional endpoints for new pulmonary valve replacements can be defined. Concurrently, these endpoints can then be compared and contrasted to current knowledge about aortic valves elucidating further their anatomical and physiological differences. Though the two valves share a common function, they do so under vastly different operating environments and this difference alludes to some unknown differences that may explain the success of the Ross procedure. By understanding the physiology of the valves, other treatment alternatives such as tissue engineered heart valves will also benefit by having a known archetype as a design endpoint.

1.1 BASIC CARDIAC ANATOMY

The circulatory system provides the body with a means of moving nutrients and wastes in an efficient manner through the system. The centerpiece of the circulatory system is the heart. The human heart is divided into four chambers whose walls are primarily composed of cardiac muscle. The upper chambers are referred to as atriums and the lower two chambers are referred to as the ventricles. They are further differentiated by what side of the heart they are located upon (i.e. right atrium, left atrium, right ventricle, left ventricle) as seen in Fig. 1. The atrium and ventricle of each side of the heart are divided by one-way valves. The valve between the atrium and ventricle on the right side is termed the tricuspid valve and on the left side the mitral valve. The aortic valve is located at the intersection of the aorta and the left ventricle and the pulmonary valve is located where the pulmonary artery attaches to the right ventricle.

Electrical stimulation. The heart is partially auto-regulated by the sequential firing of a network of nervous fibers. The sino-atrial (SA) node is located in the wall separating the two atriums. The SA node then stimulates the atrio-ventricular (AV) node located at the intersection of the atriums and ventricles. The AV node propagates the action potentials downwards through the wall separating the ventricles in the bundle of His. At the apex of the heart, the activation then spreads outwards through the walls of the ventricles through the Purkinje fibers. Activation of the SA node occurs through slow leak Ca^{2++} channels. When the activation threshold is reached, an action potential is triggered and propagated throughout the cardiac muscle of the heart.

Cardiac muscle. Cardiac muscle is unique for its auto-excitatory abilities, intercalated discs, and the presence of gap junctions. Upon electrical stimulation, cardiac muscle is capable of maintaining its own rhythmic contractions. The intercalated discs are structures located between individual cardiac muscle cells which assist in binding the cells together and transmitting force amongst them. Gap junctions are pores that connect individual cardiac muscle cells and enhance the propagation of action potentials [5].

Circulation. Blood leaving from the heart is pumped through a system of arteries and veins before it returns to the heart and lungs for oxygenation and further circulation. Nutrients are found in high concentration in the blood and diffuse out into the tissue whereas wastes undergo the opposite gradient. Erythrocytes carry oxygen molecules bound to hemoglobin to oxygen deficient tissue where conditions favor the release of the bound oxygen from the heme groups. Arteries are the main oxygen carrying vessels that emanate from the heart. They are relatively thick-walled and are capable of expanding and contracting because of the presence of smooth muscle in their walls. Arteries subdivide into arterioles and then further into capillaries. Arterioles are responsible for the resistance to flow in the circulatory system. Exchange of nutrients and wastes occur solely in the capillaries because only they possess the single cell thick walls required for exchange. The capillary beds drain into venules and then into veins which are then responsible for returning the deoxygenated blood to the heart. Veins are relatively thin walled and do not possess the same degree of smooth muscle control as the arteries do. Movement of blood through the veins is accomplished primarily through the contraction of surrounding skeletal muscle. Retrograde blood flow is prevented in the veins by the presence of one-way valves [5].

Cardiac cycle. Blood from the vena cava initially enters the heart in the right atrium. The right atrium then contracts and pushes blood through the tricuspid valves into the right ventricle. From the right ventricle, the blood is pumped through the pulmonary valve into the pulmonary arteries that lead to the lungs where the blood is oxygenated. The blood returns through the pulmonary veins into the left atrium and then through the mitral valve into the left ventricle. The left ventricle contracts and pumps the blood through the aortic valve and into the aorta where it is then distributed throughout the systemic circulation. During the cardiac cycle, a healthy aortic valve withstands pressures that ranges between 80 and 120 mmHg and does so approximately 3 billion times throughout its lifetime (Fig. 2). The pulmonary valve is also a tri-leaflet valve that performs the same function in the right ventricular outflow tract. Because of the decreased pressure gradient across the pulmonary valve, about a seventh of that in the aorta, the structure of the pulmonary leaflet differs from that of the aortic valve. The pressure within the pulmonary artery circulation varies between 25 and 8 mmHg at systole and diastole with an average of about 15 mmHg [5].

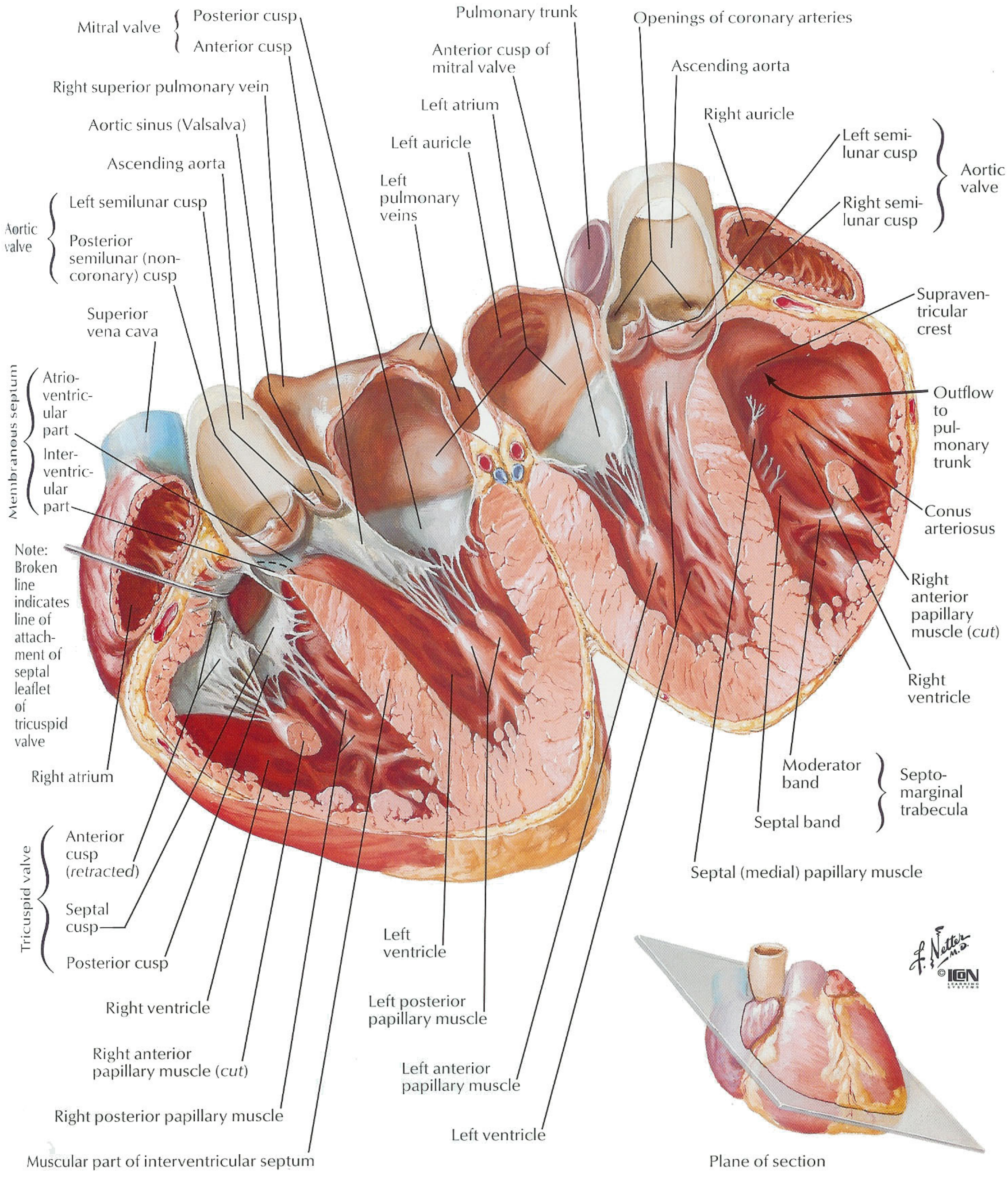

Figure 1, Schematic depicting major features of the heart. Reproduced from Netter, Atlas of Human Physiology, 1997[6].

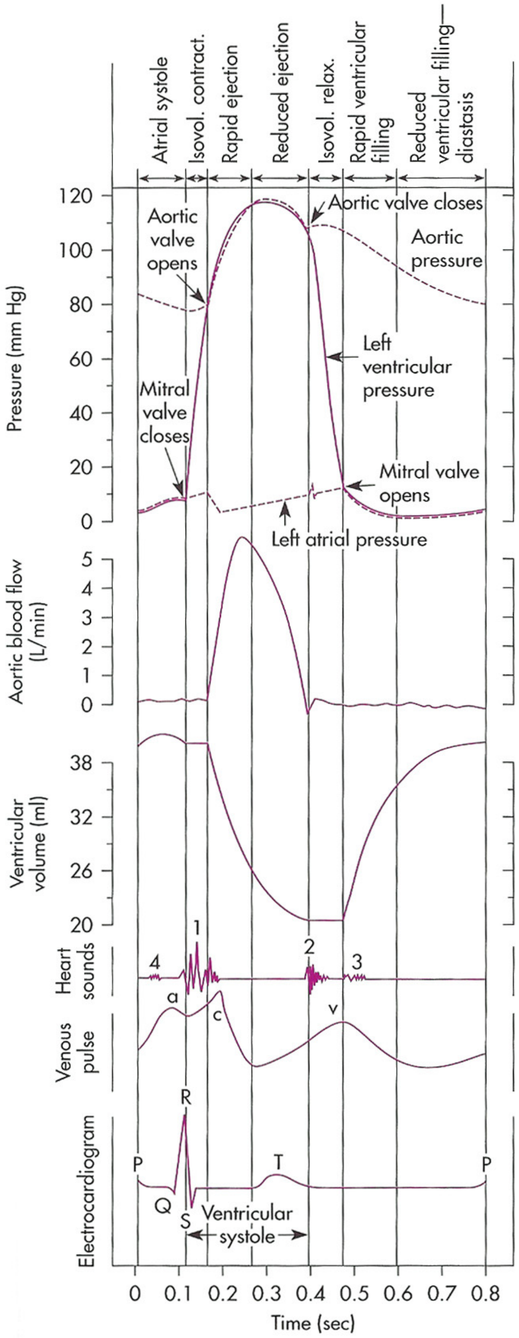

Figure 2, Diagram showing the pressures, flow, ventricular volume, and electrical stimulation experienced by the heart during the cardiac cycle. Reproduced from Berne and Levy, <u>Physiology</u>, 1998 [5].

1.2 HEART VALVE ANATOMY

Atrioventricular valves. The tricuspid and mitral valves are referred to as atrioventricular valves because they serve to separate the atrium and ventricle of the right and left sides of the heart. The tricuspid has three leaflets and the mitral or bicuspid valve has two leaflets. The leaflets are attached via chordae tendanae to the papillary muscles located within the interior of the ventricle wall and serve to stabilize the valves.

Semi-lunar valves: The aortic valve and pulmonary valve, also known as semi-lunar valves, are both composed of three approximately equal sized leaflets that close to form an effective barrier against the retrograde flow of blood. The aortic valve is located within the left ventricular outflow tract between the aorta and the left ventricle. The pulmonary valve is located within the right ventricular outflow tract between the left ventricle and the pulmonary arteries. The leaflets are enclosed within a sinus that bulges out at the center of each leaflet (Fig. 3). The attachment between the leaflet and the sinus wall is referred to as the basal region and it is where the leaflet is thickest. On the aortic valve, the transition between the valve sinus and the aorta is referred to as the sinotubular junction. Similarly, the border between the valve sinus and the left ventricle is referred to as the aortic annulus. When the valve closes, the lip along the edge of each leaflet overlaps with the lip of each of the adjacent leaflets. This area is called the coaptation surface or free edge and provides an area for the leaflets to seal against each other to prevent regurgitation. It has also been hypothesized that this surface alleviates and supports some of the stress associated with the closing of the valve. The commissure refers to the section of the leaflet that borders along with its neighboring leaflets so thus every leaflet has a commissure on its side. The commissures also define the borders between the sinus bulges surrounding the leaflet.

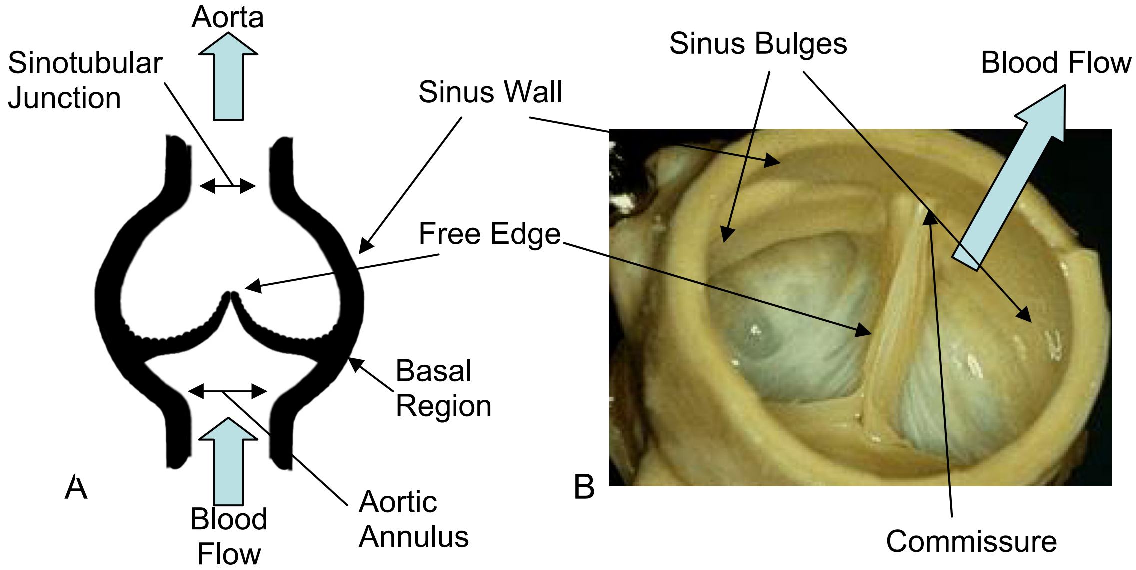

Figure 3, (A) is a schematic of the major features of the aortic valve. (B) is photo of an intact porcine aortic valve. Each of the three leaflets of the valve is located within its own sinus which is essentially a large bulb. The sinotubular junction is located where the sinuses terminate and the aorta begins. Likewise, the aortic annulus is located between the left ventricular opening and the beginning of the sinuses. The basal region is the thickened portion of the leaflet closest to its attachment edge on the sinus wall.

The sinuses are differentiated from each other by coronary arteries that originate from two of the sinuses. Thus one sinus is referred to as the noncoronary or posterior sinus and the other two are the right and left coronary sinuses. The leaflets are also differentiated by these references as the left, right, and posterior leaflets (Fig. 4). The coronary arteries provide the blood flow required by the heart itself to function [7]. The pulmonary valve does not benefit from the same level of study as the aortic valve but structural definitions such as the sinuses, commisures, basal region, and free edge are applicable.

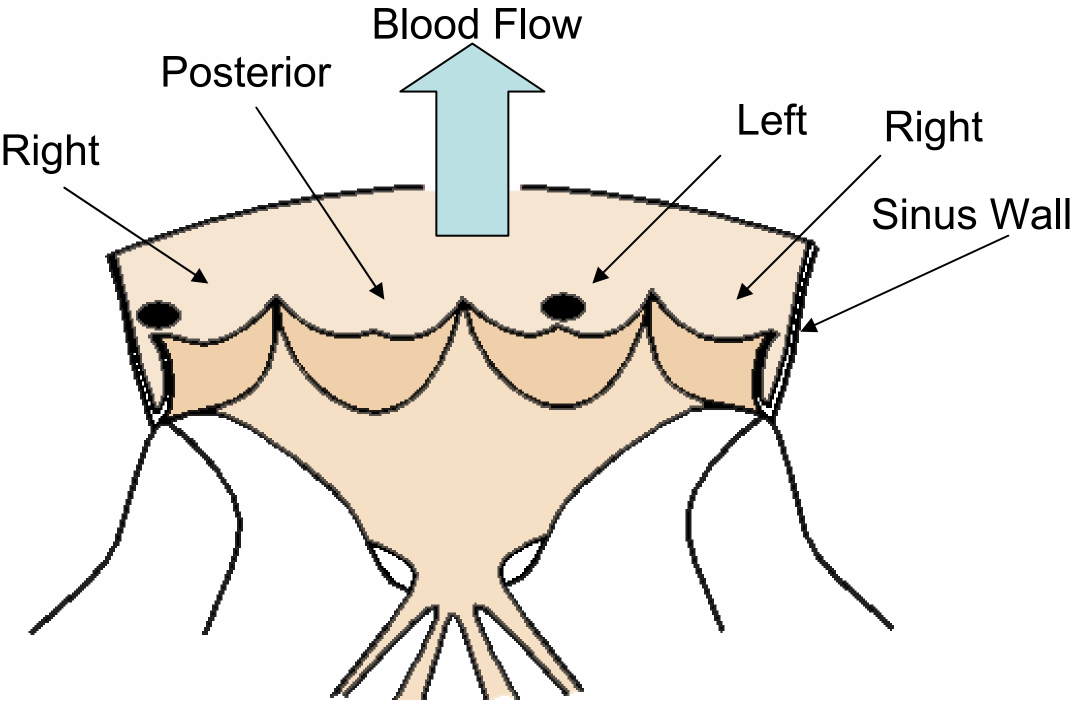

Figure 4, Schematic of a cross-section of the leaflet cut through the right coronary sinus and leaflet showing the relative positions of the other sinuses and the presence of the coronary arteries.

The center of the leaflet is referred to as the belly region (Fig. 5). In the middle of the leaflet where the belly meets the coaptation surface or free edge is located the nodulus of Arantii, a thick knot of tissue. The coaptation surface, as discussed above, is the area of the leaflet that overlaps with its neighboring leaflets to seal the valve closed. In fig. 4 the fibrous nature of the leaflet is evident. The attachment edge is the thickest portion of the leaflet and, along with the commissures, demarks the end of the leaflet and the beginning of the sinus. Compared to the length of the free edge, the attachment edge (including the commissures) is approximately 1.5 times longer. The noncoronary or posterior leaflet is very slightly larger than the right and left coronary leaflets [7].

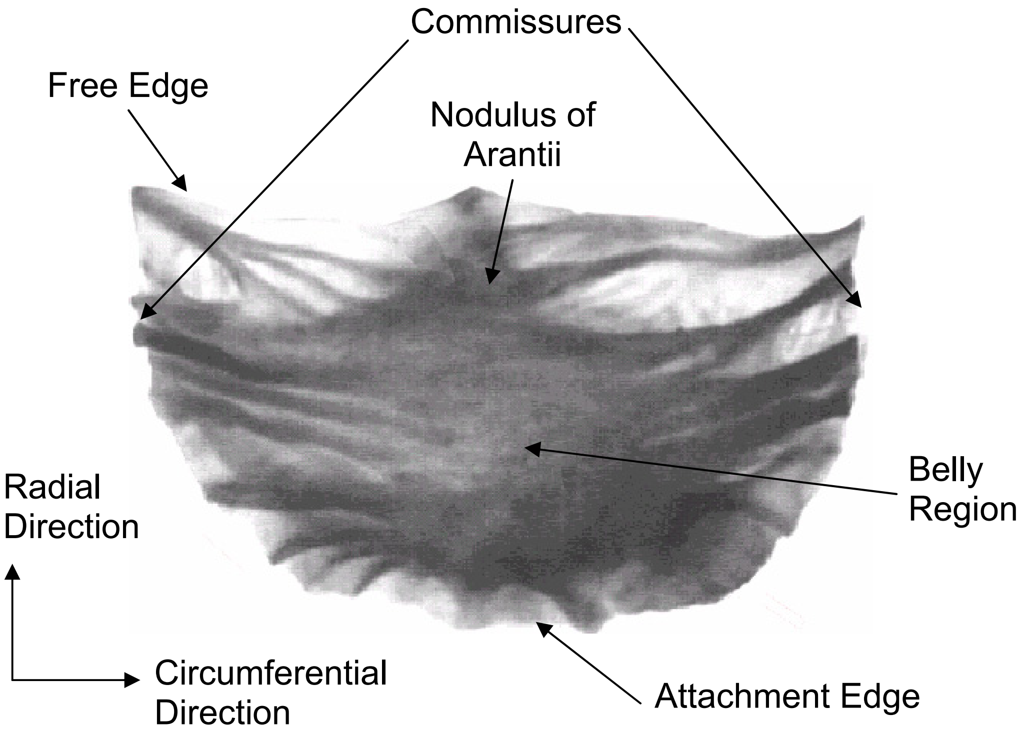

Figure 5, Schematic of a single valve leaflet and its major components. The circumferential and radial directions coincide with the circumference and radius of the aorta, respectively. The free edge is the part of the leaflet that meets with the other two leaflets to form a seal against blood flow. The Corpus Arantii or nodulus of Arantii is located in the middle of the leaflet at the free edge where it meets the noduli of the other leaflets. The commissures are located at the sides of the leaflet where the leaflet is joined with the adjacent leaflet.

1.3 SEMI-LUNAR VALVE LEAFLET MICROSTRUCTURE

Both the aortic and pulmonary valve leaflets are composed of three distinct layers: the fibrosa, spongiosa, and ventricularis [7]. Each of these three layers has different compositions that contribute to functional differences between them for valve function. The three primary components of each of the leaflet layers are collagen, elastin, and glycosaminoglycans (GAGs).

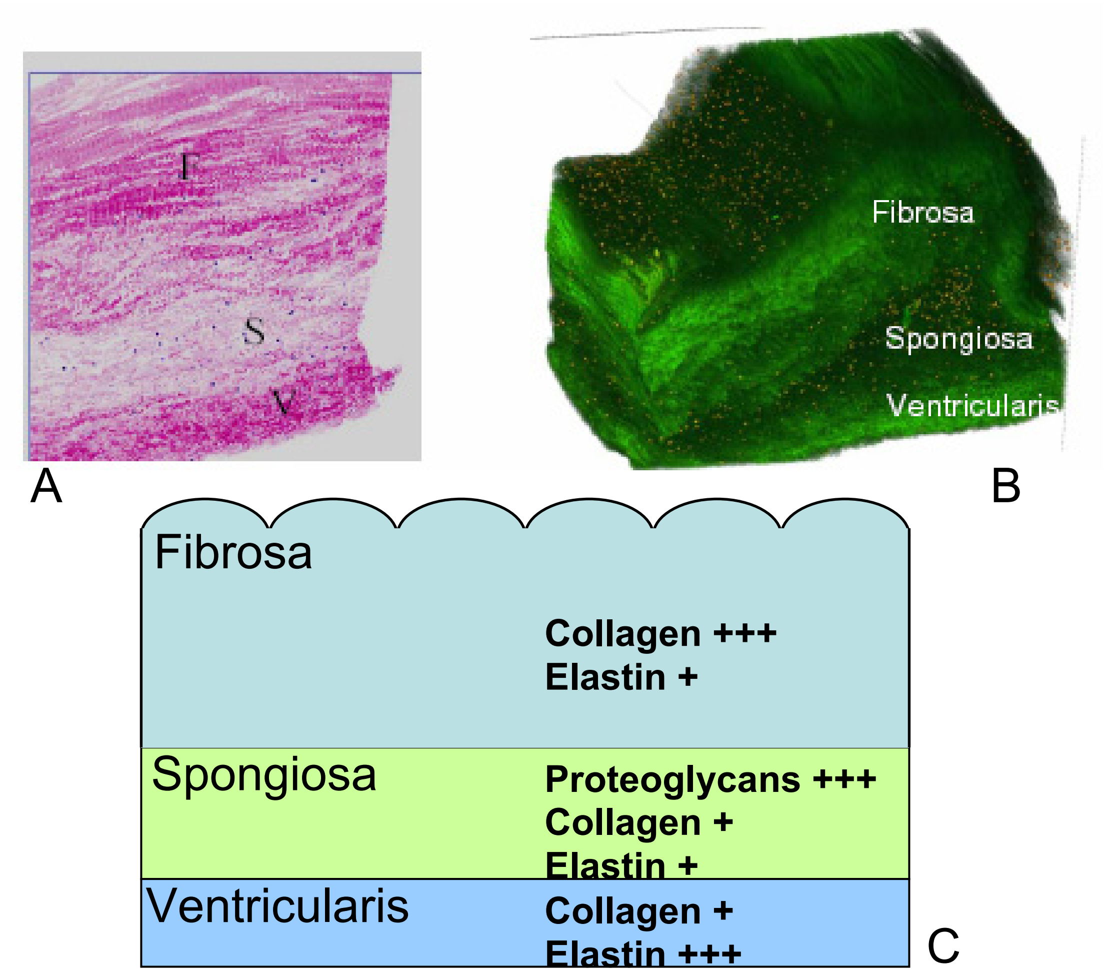

Figure 6, Schematics showing the detail of the layers of the aortic valve. 2A is a H&E histology section showing the relative thicknesses of the three layers (F, S, V for fibrosa, spongiosa, and ventricularis respectively). 2B is a 3D reconstruction of a section of aortic valve showing the three layers. Human aortic valves consist of primarily 43-55% collagen and 11-13% elastin (dry weight ratio) [8].

Collagen. Collagen fibers are common fibrous proteins composed of a triplet of α chains wound around each other in a super helix (Fig. 7). This helical structure relies upon the abundance of proline and glycine for stabilization and compactness, respectively. Some proline and lysine residues are hydroxylated with some hydroxylysines undergoing further glycosylation to form stabilizing hydrogen bonding sites. Collagen molecules are assembled into nanometer diameter fibrils which are then organized further into micrometer diameter fibers. Although an abundance of collagen fibers types are present in the body, leaflets are composed mainly of type I collagen with some type III collagen. Collagen excels as a tensile stress bearing relatively inelastic fiber (1-2% strain) [9].

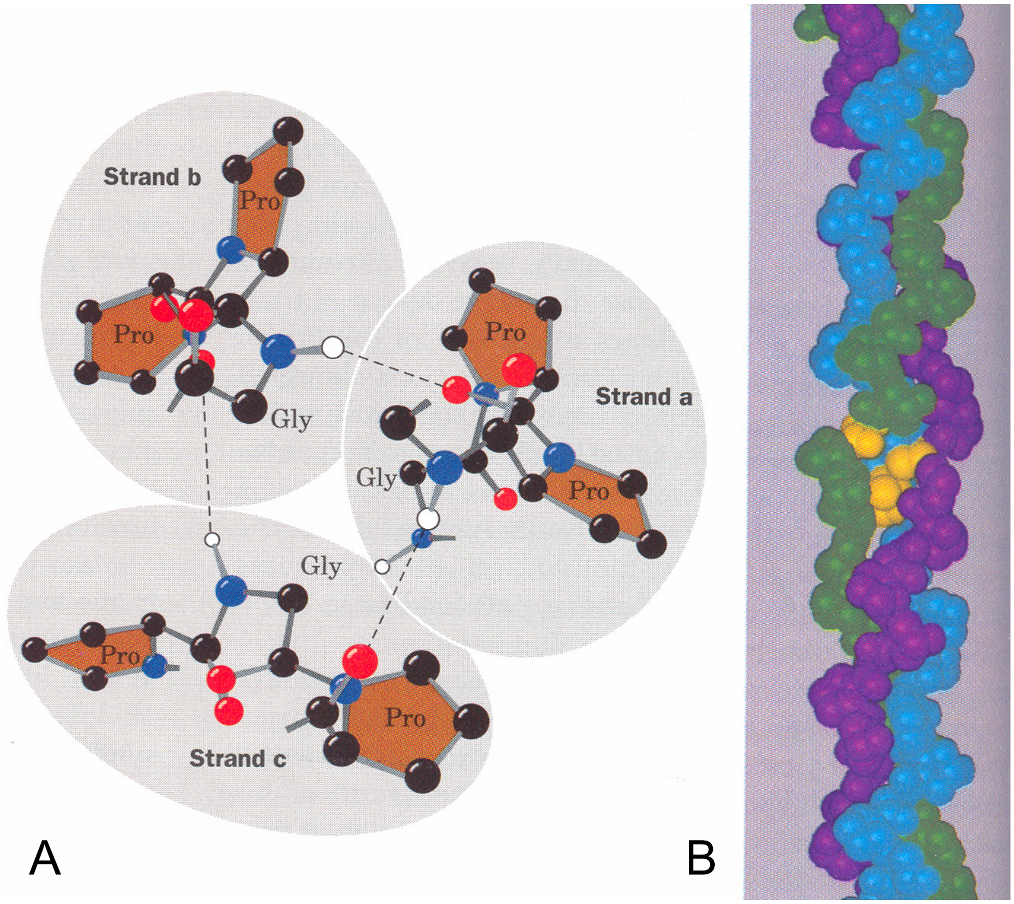

Figure 7, Schematic showing the hydrogen bonding between strands that is responsible for collagen's strength (A) and the tri-helical structure that the three collagen strands take when they assemble into a collagen fiber (B). Reproduced from Voet, Biochemistry, 1995. [10]

Elastin. Elastin fibers are composed of proline and glycine rich hydrophobic proteins that, unlike collagen, do not possess hydroxylated or glycosylated residues. These hydrophobic elements are cross-linked with alanine and lysine rich alpha helixes to form the elastin protein. As another contrast to collagen, elastin specializes as a fiber possessing elastic properties, permitting large extensions of the molecule as a rubber band would. The structure of elastin is highly branched and coiled and is hypothesized to be the mechanism which endows elastin fibers with their elasticity (Figs. 8 & 9) [9].

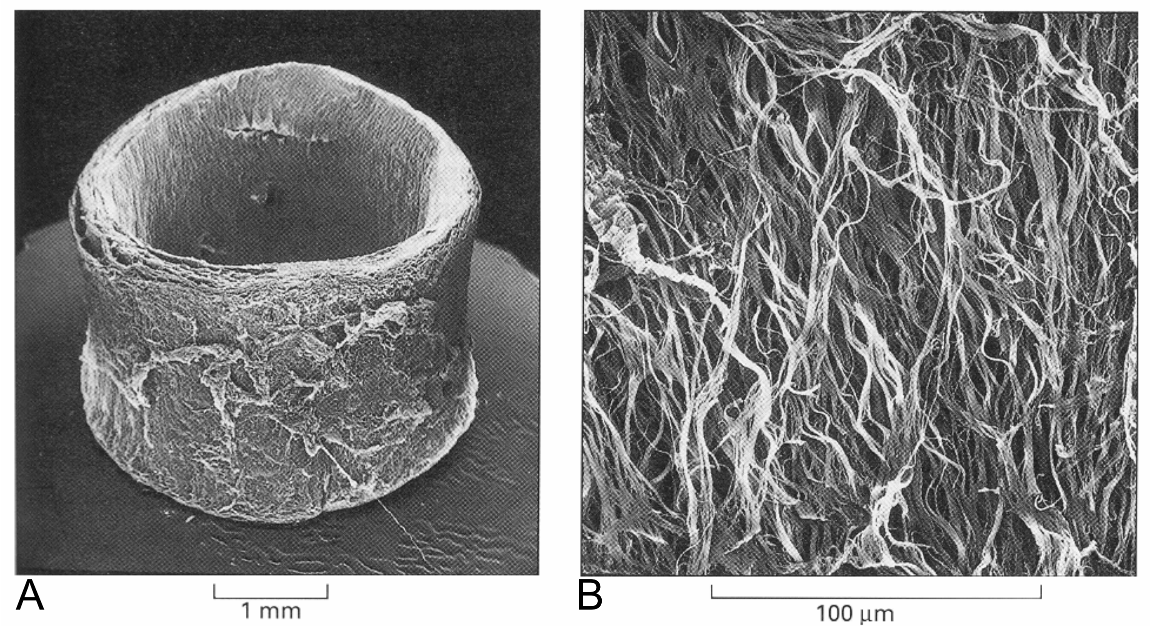

Figure 8, (A) shows a macro-scopic view of a canine aorta and (B) shows a microscopic view of the same aorta after all other components excepting elastin have been digested and removed. Reproduced from Alberts, Molecular Biology of the Cell, 1994. [9]

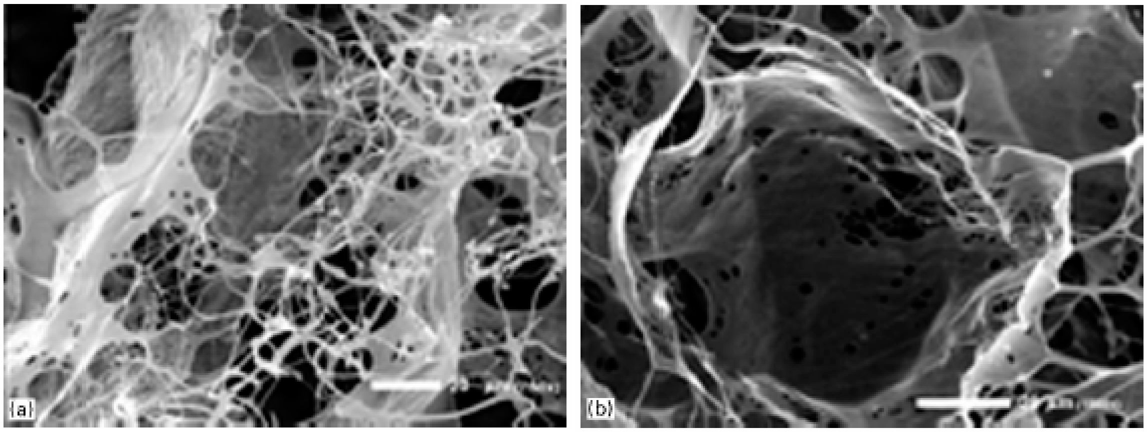

Figure 9, SEM pictures of elastin structures obtained from aortic valves after being digested with NaOH. (A) shows fibers forming a sheet and (B) details an elastin tube. Reproduced from Vesely, 1998 [11].

Glycosaminoglycans (GAGS). The third component, GAGs, are negatively charged unbranched polysaccharides formed from repeating units of disaccharides (Fig. 10). The negative charge of the GAG promotes the accumulation of cations and the subsequent osmotic attraction of water. The hydrophilicity of GAGs accounts for their relatively large volume given their molecular weight. This property also enables them to provide resistance to compressive forces due to the incompressibility of water [9].

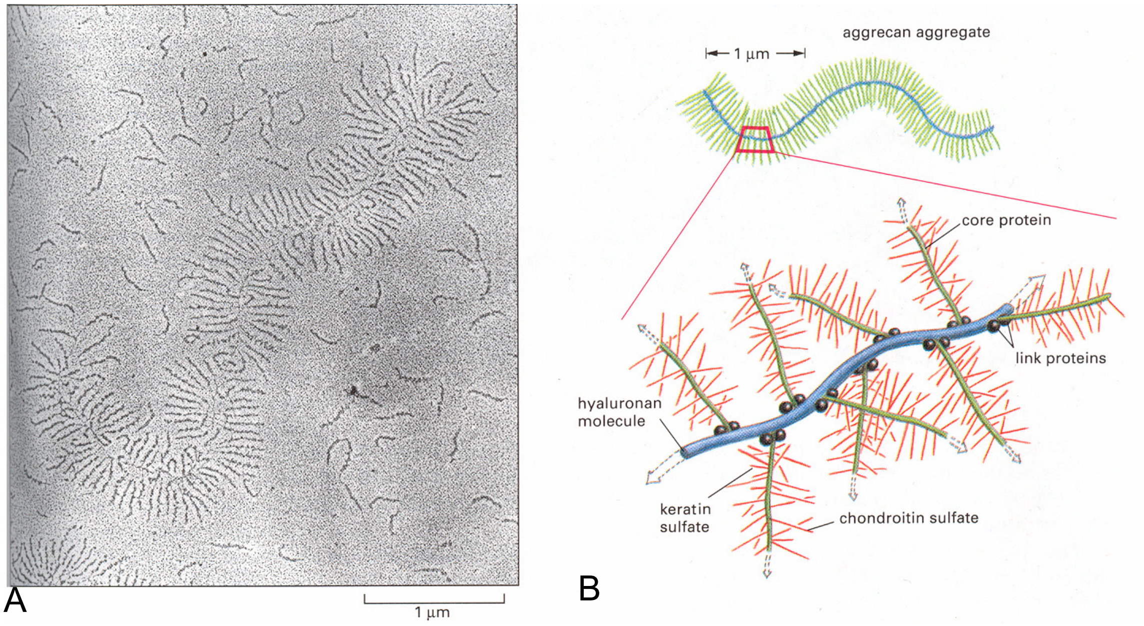

Figure 10, Picture in (A) shows an electron micrograph of a typical GAG molecule. (B) illustrates the extensive branching characteristic of GAG molecules which account for their ability to attract and retain water molecules to enhance their molecular volume. Reproduced from Alberts, Molecular Biology of the Cell, 1994. [9]

Lamina fibrosa. The fibrosa lies along the surface facing towards the aorta. Its surface is uneven in contrast to the ventricularis because it does not contact blood flow during ventricular ejection (Fig. 6). The fibrosa can be considered the strongest of the three layers. Its structure consists mainly of dense collagenous fibers woven circumferentially. As mentioned before, ridges and a generally uneven surface characterize the surface of the fibrosa. The belly of the leaflet does not have as tightly a woven fibrous structure as the base and free edges of the fibrosa layer [7]. Elastin fibers are randomly found within the fibrosa but do not form any sort of organized structure such as that found in the ventricularis [12].

Lamina spongiosa. The spongiosa is located between the fibrosa and the ventricularis. This structure has been postulated to be responsible for the plasticity of the leaflet and for dampening vibrations caused by leaflet opening and closing. The spongiosa layer contrasts the other two layers and has a relatively watery unorganized structure. Some collagenous fibers are present in a radial orientation and have been observed to be attached to the fibers in the fibrosa. Otherwise, the spongiosa consists mainly of water and glycosaminoglycans or GAGs [7]. Its spongy nature may act as a transition between the stiff fibrosa layer and the elastic ventricularis layer [13]. The GAG has also been described as viscoelastic and responsible for some level of energy absorption during deformations of the valve cusp [14].

Lamina ventricularis. The ventricularis lies along the surface of the leaflet facing the left ventricle. This surface is smooth, attributing to the necessity of maintaining laminar blood flow. The ventricularis is made of an elastic sheet over a collagenous sheet that apparently is a continuation of the exit orifice of the left ventricle. The elastin fibers in the elastic sheet are oriented radially in contrast to the circumferentially orientated collagenous fibers. The ventricularis thickens towards the leaflet nodule where the leaflets meet each other to close [7].

1.4 CURRENT STUDIES REGARDING THE AORTIC AND PULMONARY VALVES

There have been a very limited number of studies performed examining the pulmonary valve with intentions of studying its structure and mechanical properties. There have been an even lesser number of studies directly comparing the pulmonary and aortic valves. Testing methods are also usually limited to tensile testing or biaxial testing which do not accurately capture the range of motion possible for a leaflet *in vivo*.

Broom performed an examination of the structure of porcine aortic and pulmonary leaflets using Nomarski differential-contrast imaging to avoid the altering effects of scanning electron microscopy and histology. His results demonstrated that the structure and makeup of the pulmonary valve was similar to that of the aortic valve and possessed the same elastin rich ventricularis and collagen dense fibrosa. Collagen crimp was observed to permit the gross extension of the tissue to the limit where the crimp was straightened. Elastin was shown to form convoluted networks that defied efforts to visualize them under stress but seemed to abide by Poisson's ratio. The tissues were fixated with glutaraldehyde for preservation purposes, however, resulting in the cross-linking known to alter the natural behavior of the tissue [15]. The use of innovative imaging techniques is an essential step in determining mechanical properties at the tissue level where conventional means of observation and measurement are insufficient.

Using circumferentially and radially oriented test strips obtained from porcine aortic and pulmonary leaflets, David et al performed tensile tests to determine their mechanical behavior. They tested fresh tissue and tissue that had been fixated in glutaraldehyde and confirmed the difference in thickness between the two leaflet types. Elastic properties were found to be similar between the leaflets with regard to their native or fixated state and their orientation. Based upon their findings, they determined that pulmonary valves were sufficiently mechanically similar to aortic valves to justify their use as their replacements. However, their experiments were limited to tensile modes of deformation that were incapable of faithfully simulating physiological conditions [16].

Christie et al performed a study examining the biaxial behavior of porcine aortic and pulmonary valve leaflets in extension before and after fixation with glutaraldehyde. Square tissue specimens were dissected and mounted using four hooks on each side of the tissue to ensure a homogenous force application on each edge. A suture was made in the center of specimen to mark the geometric center and location of strain measurements. Tissue markers were provided by silicone carbide markers that were placed around the center of the specimen. All of the specimens were tested under a stress controlled protocol yielding tractions of 60 Nm^{-1}. Their results from tests on fresh samples showed that pulmonary valves were more extensible in the radial direction but similar in the circumferential direction to aortic valves. They also reported a decrease in strain in the circumferential direction in pulmonary leaflets as the load increased [17].

1.4.1 Heart valve flexural mechanical properties

To achieve the combination of low flexural rigidity necessary to allow normal valve opening, nature has evolved a tri-layered cuspal structure: the ventricularis, spongiosa, and fibrosa [8]. The ventricularis layer is composed of a dense network of collagen and elastin fibers, the spongiosa layer contains a high concentration of proteoglycans, while the fibrosa layer is composed predominantly of a dense network of collagen fibers, and is thought to be the major stress-bearing layer [7]. *Thus, any biomechanical study of heart valve leaflets must be designed to elucidate the unique mechanical properties of the tri-layered aortic cuspal structure.* This is especially important when determination of the layer mechanical properties of the compliant cuspal tissue in the low stress-strain region is considered. For example, while our biaxial mechanical testing technique successfully quantified the in-plane stress-strain response [18], it cannot determine the contributions of individual layers since all the fibers through the thickness are loaded simultaneously. Further, although the cuspal displacements are large the tissue strains are actually small, so that the low strain region of stress-strain curve is of interest. Mechanical properties in the low strain region are notoriously difficult to obtain accurately from tensile studies [19], which also cannot measure compressive stiffness. Vesely and Noseworthy [20] have demonstrated that the ventricularis layer preloads the fibrosa. Uniaxial characterization of separated fibrosa and ventricularis layers were also conducted and indicated substantial differences. However, uniaxial testing and uni-dimensional strain analyses cannot be used to characterize the anisotropic mechanical properties of biological tissues, including the low-strain region.

Flexure represents not only a natural deformation mode of the valve leaflet, it also introduces a deformation mode in which the different layers (unlike uni- or biaxial tensile experiments), experience different strains. Further, the stress-strain response of the individual cuspal layers in the low strain region under *both tension and compression can be obtained without the need for dissection or other interventional approaches*. Previous biomechanical studies have attempted to determine leaflet bending properties. While elucidating some important tissue mechanical principles, the methods employed forced the specimen into non-physiologic loading states [21, 22]. More direct methods of measuring the shear behavior of the cusp using two moving plates have been attempted with intriguing results [23]. However, the effects of unavoidable tissue compression by the plates on the highly undulated aortic surface of the cusp and the non-physiologic nature of the induced tissue deformations make physical interpretation of the results unclear. Our laboratory has pioneered the use of a 3-point bending to elucidate the mechanical properties of native [24], bioprosthetic [25, 26], and engineered valve tissues [27, 28]. However, the micro-mechanical basis underlying the observed response has yet to be elucidated.

1.4.2 Aortic valve biaxial mechanical behavior and structural constitutive model.

In the University of Pittsburgh, we developed experimental techniques to determine the mechanical properties of the AV cusp under biaxial loading [29, 30]. Briefly, cuspal specimens were subjected to biaxial tests utilizing seven loading protocols to provide a wide range of load states (Figure 12). The cusps demonstrated a complex, highly anisotropic mechanical behavior, including pronounced mechanical coupling between the circumferential and radial directions. Mechanical coupling between the axes produced negative strains along the circumferential direction and/or non-monotonic stress-strain behavior in many samples subjected to equi-biaxial tension. This study provided new insights into the AV cusp structure-function relationship. Next, Billiar and Sacks formulated the first constitutive model for the AV to describe its biaxial data [31]. A structural approach was used, in which we demonstrated that *only three parameters were needed to describe cusp's complex behavior and predict a wide range of responses (Figure 11).* In addition to providing a means to accurately simulate AV response, the structural model was also able to demonstrate that the complex cross-coupling is a result of the narrow angular distribution of collagen fibers of the AV cusp. This was particularly evident with the presence of negative strains in the circumferential direction when the angular distribution of fibers was <20°. *These results underscored the importance of understanding the role of tissue structure in understanding and modeling cuspal tissue mechanical properties.*

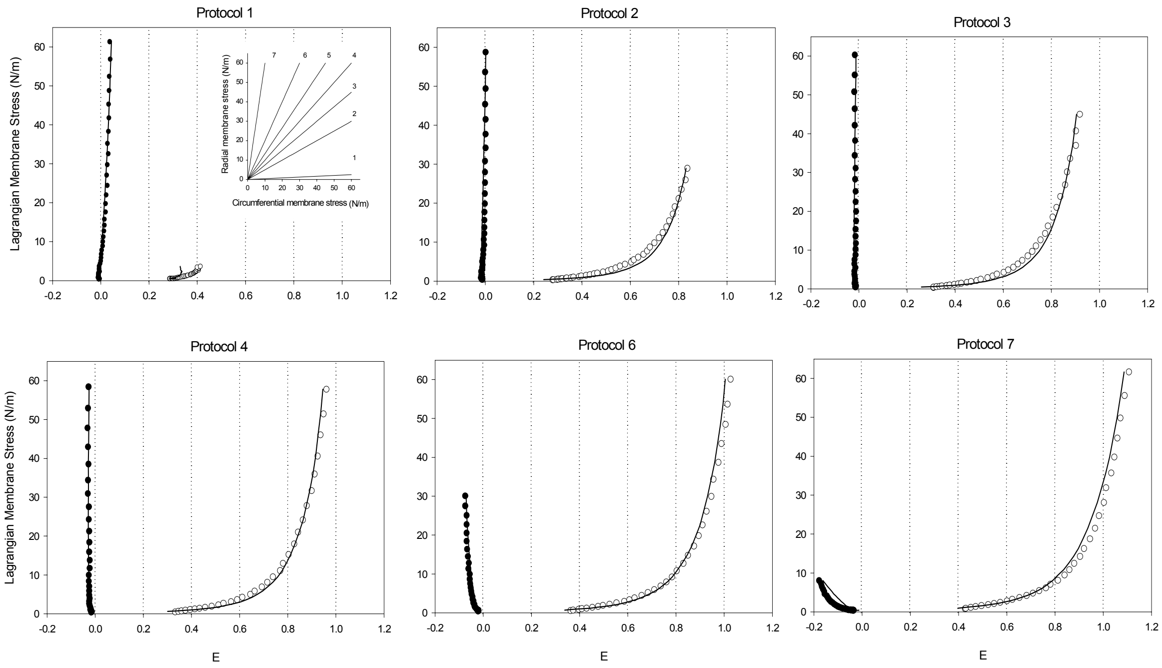

Figure 11, a) The seven loading protocols used to characterize the biaxial stress-strain response, and (b) response to all loading protocols for a AV cusp (open circles), along with the structural model fit, demonstrating an excellent fit. Taken from [31]

1.4.3 Mechanical properties of the aortic valve cuspal layers

In our previous model of the aortic valve, the relative contributions from each layer were unknown. To ascertain if there are differences on how fibers within the fibrosa and ventricularis layers contribute to the overall tissue planar biaxial response, the layers of two native aortic valve cusps that were previously biaxial tested were separated. Following methods used in [32], each cusp biaxial test specimen was laid flat under a dissecting microscope, then the the fibrosa and ventricularis layers were carefully separated with a pair of straight iris micro-scissors. Each separated layer was then retested under biaxial stretch (Fig. 12). Results indicated that substantial differences in layer mechanical properties were present, and suggest the need to incorporate these important structural/mechanical properties into future computational models of the aortic valve.

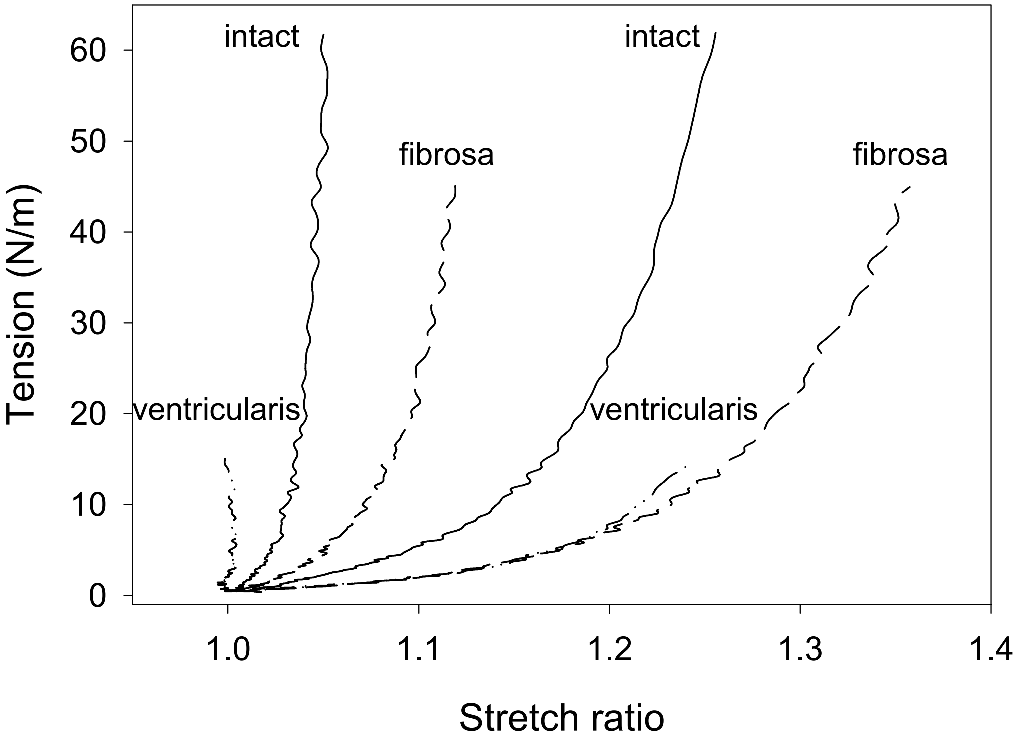

Figure 12, Biaxial mechanical properties of the intact (i.e. original), fibrosa, and ventricularis layers of the native aortic valve cusp. Note the substantial differences in mechanical properties of the individual layers.

1.5 HEART VALVE DISEASE

Pediatric. Disease of the aortic valve and pulmonary valve in children and adults can be a result of congenital defects or from a contracted disease such as rheumatic fever. Cardiovascular congenital defects claimed the lives of over 4100 people in 2001 with 2100 of those individuals being under the age of 15. Diagnosis of congenital defects can be difficult and some cases, such as those of bicuspid (two-leaflet) aortic valves which occur in 13.7 of 1000 people, are not found until they cause later complications at an advanced age. Out of 1000 live births per year, 9.0 defects are expected with a total number of cardiovascular defects being about 36,000 babies annually. Of these babies, 2.3 babies per 1000 require invasive treatment or die within the first year. Overall inpatient mortality for cardiovascular defect related surgery was 4.7 percent [1]. Pulmonary valve deficiencies, such as tetralogy of Fallot (TOF), are congenital defects which affect pulmonary valve function and usually result in either the total removal of the pulmonary valve (pulmonary valvotomy), or the use of a replacement valve. TOF itself accounts for approximately 10% of all cardiac malformations [33]. Diagnosis of these deficiencies can occur via echocardiography while the baby is still a fetus or after birth if the baby exhibits blueness.

Adult. Rheumatic fever remains a significant cause of cardiovascular disease in developed countries and occurs to between 100 and 200 school age children per 100,000 but also affects adults. Heart valve damage occurs when the body’s immune response to the viral infection attacks causes inflammation and damage to the myocardium [34]. Bacteria can also damage the heart valves in a condition known as infective endocarditis. Treatment is normally undertaken with the administration of antibiotics but valve replacement is also indicated when the damage to the valve is too extensive [35]. Adults are also susceptible to those congenital heart defects that do not manifest themselves until after childhood. Amongst adults with these defects, 26% suffered sudden death, 21% died from progressive heart failure, and 18% from peioperative death. In the United States alone there are approximately 800,000 people with significantly life expectancy lowering congenital heart defects [36]. Deficiency of the heart valve in children and adults normally occurs via two primary pathways, stenosis (obstruction) or regurgitation.

Stenosis. Stenosis of the valve obstructs the flow of blood from the left ventricle to the aorta and systemic circulation. As a consequence, blood delivery is retarded and symptoms of insufficient circulation are experienced. Stenosis occurs when the patients are born with problems such as a bicuspid or other malformed valve. The defective valve does not possess the excellent hemodynamics of the normal valve and turbulent blood flow is a result. Thus, calcium deposits may begin to grow upon the valve and the possibility of bacterial infection is encountered. Calcification and the growth of scar tissue aggravate the stenosis by further misshaping the valves and altering their mechanical properties. Insufficient blood flow through the valve stimulates the left ventricle to hypertrophy, or increase in size, to compensate for the smaller orifice. This worsens the condition of the patient by damaging the entire heart, leading to eventual morbidity through heart failure or through failure of the stenotic valve.

Regurgitation. Regurgitation is a condition that afflicts similarly malformed valves and can be coincident with stenosis. When the pressure in the aorta exceeds that of the left ventricle, blood begins to flow backward and pushes the leaflets of the normal valve to coapt and shut. However, if the valve does not close completely, blood will flow back into the left ventricle, sabotaging the advancement of blood through the aorta. Severe cases of regurgitation will produce results similar to stenosis. Hypertrophy of the heart is also a result of regurgitation for the same reasons as in stenosis, inadequate blood flow and delivery. Diagnosis of these conditions can be accomplished by finding a heart murmur that results from the turbulent flow or through echocardiography [37].

1.6 TYPES OF VALVE REPLACEMENTS

Regardless of the dysfunction pathway taken by the valve, repair or replacement of the valve is necessary to maintain an acceptable quality of life. Currently, valves can be replaced with either a mechanical or bioprosthetic prosthesis, each with its own advantages and disadvantages. Another option gaining in some popularity amongst younger patients is the Ross procedure (mentioned above) [38-41]. Tissue engineered heart valves are another form of replacement being researched but will not be discussed because they remain in development and are not currently considered standard treatment.

1.6.1 Mechanical heart valve replacements

Mechanical valves are produced by a number of different companies offering different advantages and benefits. The majority of the designs in use are bileaflet or unileaflet tilting disk valves (Fig. 13) [42]. Because these valve alternatives are manufactured commercially, there are no concerns about availability and scarcity. When mechanical valves were first introduced there were some mishaps with design and manufacture, leading to some initial deaths. However, with advancing designs and improved standards and testing, mechanical valves have established themselves as a reliable replacement for adults aged 65 years and above according to guidelines set forth by the American College of Cardiology and the American Heart Association [43].

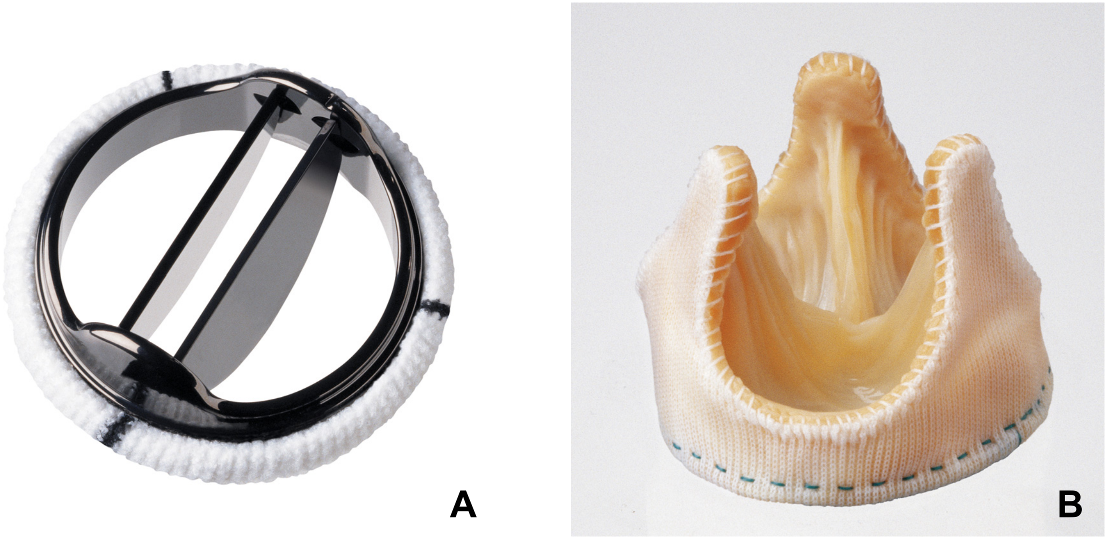

Figure 13, The SJM Regent® mechanical valve (A) and the Toronto SPV® bioprosthetic valve (B) are shown. Copyright St. Jude Medical, Inc. 2004. These images are provided courtesy of St. Jude Medical, Inc. All rights reserved. SJM Regent and Toronto SPV are registered trademarks of St. Jude Medical, Inc.

The disadvantage to having a mechanical valve implanted is, in some cases, severe. The blood that continually passes through the valve will be affected by its presence and by the difference in hemodynamics. Mechanical valves do not possess the same hemodynamics the native valves possess so that some damage to blood cells, also known as hemolysis, will occur. Significant hemolysis will result in anemia and its coincident symptoms. The hemolysis of red blood cells will release a number of factors involved in the clotting system. This results in the development of blood clots upon the valve, hindering its operation. As clots form on the valve they are also released into the blood stream as emboli where they can potentially block vessels downstream. This can result in poor circulation in extremities to the more serious consequences of a cerebrovascular event such as a stroke [44-46].

To prevent the initiation of clot formation in the presence of a mechanical heart valve, anti-coagulants are administered to the patient. The most common anti-coagulant prescribed to patients is Coumadin. These anti-coagulants prevent the formation of clots at the mechanical valve and throughout the entire body. As a consequence, hemorrhage or bleeding internally and externally will not be stopped by the body as readily with the anti-coagulation treatment. This is the primary disadvantage of the anti-coagulation treatment. Patients are susceptible to possibly fatal and uncontrollable bleeding when undergoing anti-coagulant treatment. Too much anti-coagulant will result in excessive bleeding whereas too little anti-coagulant treatment will result in the formation of dangerous clots and emboli. To gauge the level of anti-coagulant treatment a patient is to receive, the patient must undergo regular tests to determine their blood's clotting capability and whether administration of anti-coagulant should be increased or decreased. For example, in a study by Change et al, the level of anti-coagulant therapy was modified closely to reduce the occurrences of thromboembolisms and did so successfully by increasing 5-year freedom from thromboembolism from 96.7% to 99.0%. However, bleeding fell from 99.3% to 96.1% [42]. In addition, anti-coagulant treatment itself brings with it many undesirable side-effects that lower the quality of life of the patient. Adherence to the treatment and regular blood tests are vital to the successful implementation of this option and thus its application to pediatric cases is severely limited [47]. The use of mechanical valves may be feasible in adult patients who are not physically active but children are almost always partaking in physical activity of some sort or more often susceptible to cuts, bruises, or other injuries. The implication of anti-coagulant therapy in such cases would lead to uncontrolled and fatal hemorrhaging and severely limit the freedom a child or young adult has. The inability of the mechanical valve to grow with the younger patient requires that several re-operations be performed to replace the mechanical valve in order to avoid aortic stenosis and manage somatic growth of the child [48].

1.6.2 Bioprosthetic heart valve replacements

Bio-prosthetic heart valves (BHVs) are made in primarily two varieties, a chemically treated porcine aortic valve and a chemically treated valve made of bovine pericardium (Fig. 11). Pigs are chosen for their heart valves because of the anatomic similarities between them and humans. Their valves are harvested and treated chemically to remove living tissue and prevent any possibility of rejection by the human body. Untreated implanted tissue will normally be broken down and degraded by the body, whereas xenotypic implants, those from another species, will illicit an immune and inflammatory response that will result in the rejection and breakdown of the tissue [49]. The chemical treatment with glutaraldehyde also fixates the tissue, preventing degradation and stiffening it.

The valves can be mounted on a stent and then sewn in by the surgeon. They can also come intact in the pig's aorta and be sewn in by the surgeon with more difficulty. The other types of BHVs are made of bovine pericardium. The valve is put together from pieces taken from sheets of bovine pericardium. The pieces of pericardium are also chemically treated to remove antigens and stabilize the tissue. The BHV is a good alternative for adults to the natural valve in terms of its hemodynamics and, in contrast to the mechanical valves, its absence for any anti-coagulant therapy. In pediatric cases, however, the BHV must inevitably be re-operated upon to compensate for the growth of the patient resulting in further surgical complications [38].

There are also some issues concerning the hemodynamics of the BHV because of the requirement for a stent in some installations and the difficulties in installing the valve into the patient. The primary drawback to a BHV is the relatively low durability of the valve *in vivo*. In spite of the chemical fixation, the valve will begin to degrade inside of the body and fall apart with time. Glutaraldehyde treatment itself has been implicated by some to be responsible for the onset of calcification [50]. As the valve deteriorates, the same mechanisms that caused stenosis will begin to affect the BHV and calcification begins to decrease its efficiency as a valve [51]. The deposition of calcium upon the tissue and its subsequent effects upon the mechanical properties of the tissue greatly affect its durability [12]. This deposition, located on the exterior of the leaflets is referred to as extrinsic calcification. Calcification also occurs within the leaflet, amongst the ventricularis, spongiosa, and fibrosa. This form of calcification is referred to as intrinsic calcification.

In spite of what is known about the effects of glutaraldehyde cross-linking, a great deal of understanding about the mechanical and fatigue properties of the tissue have not been fully evaluated. Cross-linked and fatigued BHV have exhibited deteriorating collagen I [50]. It has been established in previous studies that glutaraldehyde treatment does not preserve the lamina spongiosa and its rich water and GAG content [26]. Vyavahare et al's study provides data showing a depreciation of mechanical properties with time and a proportional loss of GAG content in the spongiosa layer [50]. Some studies have also shown other factors contributing to the failure of BHV under long-term use. Deterioration and delamination of collagen fiber bundles have been observed in flexed valve cusps [14]. Failure of connective tissue has contributed to tearing and the break down of tissue leading to failure. Failure through regurgitation has also been observed in BHV constructed using bovine pericardium. The edges of the leaflets degrade with time and eventually do not seal properly to prevent blood from leaking back from the aorta to the left ventricle [7].

Inevitably, re-operation is required in many cases to replace the failing bio-prosthesis with some other alternative or another bio-prosthesis. In one study, approximately 20% of patients required re-operation to their valves within the first eight years after replacement. The percentage increased subsequently thereafter. The bio-prosthetic heart valve finds its use in patients who cannot abide by anti-coagulant therapy for one reason or another or who are not expected to outlast the projected service time of the bio-prosthesis [44-46]. Thus, BHV replacement follows the same 65 years of age or older guideline as mechanical replacements [43].

1.6.3 The Ross procedure

An innovative alternative to the use of either of these replacement valves is the Ross procedure. Also known as the pulmonary autograft, the pulmonary valve is used as a replacement for the aortic valve within the same patient. The pulmonary valve is then replaced with a pulmonary homograft, a valve taken from a cadaver donor. The Ross procedure, as it is called nowadays, is a complicated surgical operation performed by only a handful of skilled surgeons in the world. The procedure transforms what would normally be a one-valve operation into a two-valve operation. At first, the aorta and pulmonary artery are transected and the diseased aortic valve is removed. The pulmonary root is then removed from the pulmonary artery and attached to the left ventricular outflow tract. The pulmonary homograft is prepared and then attached to the right ventricular outflow tract. The pulmonary arteries are then attached to complete the reconstruction of the right ventricular outflow tract. The coronary arteries followed by the aorta are attached to the autograft pulmonary root [52].

The rationale behind such a complicated procedure is the idea of using an autograft or tissue from the same human body. This negates the concern about negative immune responses to the transplant and also retains living viable tissue, enabling the transplant to grow, remodel, and repair with time. This means that the Ross procedure implanted valve does not require the debilitating anti-coagulant therapy that mechanical valves require. In addition Ross procedure implanted valves do not have the potential durability issues that bio-prosthetic valves have because they are living implants. Thus, the pulmonary autograft presents an alternative that supercedes the two greatest drawbacks of the other implantation options. The Ross implant is thus particularly attractive to use in pediatric, young adult, and active patients (Fig. 14) [53]. As a more complicated procedure, Ross operations cost more than single valve operations. However, statistics have shown that shorter post-operative stays incurred by pulmonary autograft patients offset these operative costs, leveling their costs with mechanical and bio-prosthetic replacements [54]. A successful Ross procedure can provide an almost perfect replacement for the diseased aortic valve, barring complications.

As with almost all medical procedures there are complications that can arise. In the case of the Ross procedure, serious complications may arise during surgery. When Mr. Ross first pioneered the operation, his initial morbidity after surgery was approximately 20% [55]. His procedure was limited by the amount of time he was allowed to retain the patient under cardiopulmonary bypass. When advancements were made in the technique of cardiopulmonary bypass in the 1980's the Ross procedure began to be performed by surgeons worldwide exclusive of Mr. Ross. Presently, the surgery presents the same rate of initial morbidity as much simpler valve operations. However, the difficulty of the operation results in greater morbidity for those surgeons first performing the technique. Thus, the “learning curve” for a surgeon inevitably results in some unnecessary deaths [54, 56, 57]. As more procedures are performed, however, improvements in surgeon experience and technique result in increased success with the procedure [58].

If the surgery were to be completed successfully, other complications may occur. The homograft that is used to replace the pulmonary root is susceptible to degradation just as bio-prostheses are vulnerable to degradation in the aortic position. The rationale behind placing a degradable valve in the pulmonary position is due to the different environments of the aortic and pulmonary valve positions. The lower pressures in the pulmonary circulation do not stress the substitute valve as greatly as it would if it were to be in the aortic position. In younger patients a greater immune response to the aortic homograft results in faster degradation whereas in the pulmonary position the homograft is more tolerated. Thus, the durability of the homograft in the pulmonary position is improved and the autograft in the aortic position lasts longer [59]. However, despite these assumptions, the homograft in the pulmonary position does occasionally fail. Valve failure in the pulmonary position is relatively well tolerated by the heart so the complication is not immediately fatal as an aortic valve failure would be. Re-operations to replace a failing pulmonary homograft account for approximately 1.3% of re-operations. The pulmonary autograft itself is susceptible to failure in some cases. Approximately 3.2% of pulmonary autografts must be re-operated because of total failure. These failures can be a result of degradation, infection, or surgical errors. One pathway of valve failure is due to the dilation of the pulmonary autograft root with time. As the root begins to dilate, the leaflets of the valve will no longer mate as well as before, leading to valve insufficiency. In other cases of pulmonary autograft re-operation, 2.2% were re-operated and the autograft was successfully repaired and retained. In total, 6.9% of Ross procedure patients have required re-operation for problems pertaining to the surgery or some other non-Ross procedure related complications (Table 1) [60].

Most opponents of the Ross procedure cite as one of their objections to the procedure the lack of long term results [57]. Mechanical valves and bio-prosthetic valves have been characterized in their long term behavior either through mechanical testing and simulations or long-term clinical and animal studies. Both of these alternatives also provide some level of quality assurance from the engineers who design them. The autograft used in the Ross procedure, however, does not offer any of these benefits. As it is obtained from the donor almost immediately before use, there is no opportunity to run tests to determine its quality as an aortic valve substitute. However, some mid-term results have shown that the autograft is capable of growth and remodeling along with the patient to possibly provide a viable permanent replacement [38-41].

The Ross procedure has been performed in hundreds of patients since its first use in 1967 by its innovator, Donald N Ross [60]. Most mid-term results present an optimistic outlook for the use of the Ross procedure in patients, netting a success rate approximately equal to that of mechanical and bioprosthetic replacements [54]. However, the evidence supporting the Ross procedure does not include any quantitative comparisons between the two valves or any clear understanding of any mechanisms that may influence the pulmonary valve in the aortic position. Obtaining valves after implantation for testing requires the cooperation of patients for significant follow-up procedures and has yet to be done. The feasibility of observing changes to the pulmonary valve *in vivo* is low because of the limited means of determining mechanical properties non-invasively and a poor understanding of baseline properties.

Table 1, Table showing postoperative morbidity statistics from 1,656 total Ross operations. Chart reproduced from Oury et al, "The Ross Procedure: Current Registry Results," 1998 [60].

Complications	No. of Patients	% of Total
Cardiac dysrhythmia	32	11.9
Postoperative bleeding	22	8.2
Endocarditis (new)	18	6.7
Sepsis	15	5.6
Myocardial infarction	10	3.7
Stroke	10	3.7
Thrombus	9	3.3
Endocarditis (recurrent)	7	2.6
Transient ischemic neurologic complications	5	1.9
Other complications	141	52.4
Total	269	

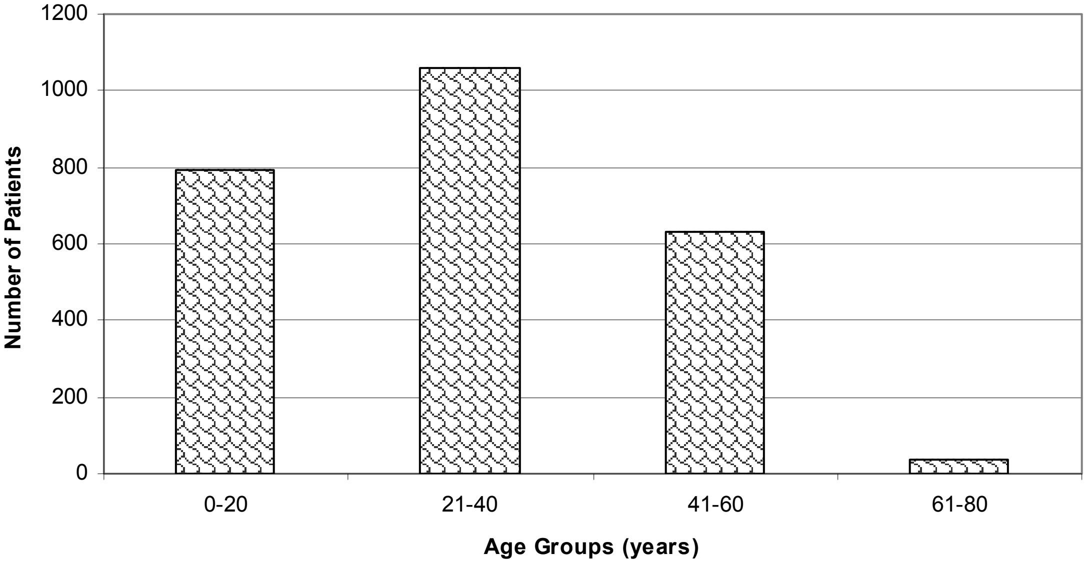

Figure 14, Chart showing number of Ross operations performed that have been registered with the International Registry of the Ross Procedure. Data taken from Oury et al, "The Ross Procedure: Current Registry Results," 1998 [60].

For the pediatric patient, the Ross procedure remains the most effective and safe replacement for the aortic valve. In a study by Turrentine et al, the re-operation rate for Ross procedures was the lowest at 11.9% compared to mechanical valve re-operations at 15.2%, BHV re-operations at 70%, and homograft re-operations at 50% [61]. In an analysis by Takkenberg et al, the Ross procedure proved to have a re-operation free life expectancy of 16 years from a patient population of 380 [62]. The homograft is the most suitable replacement for the ailing pulmonary valve because of its reduced immunogenic response compared to BHV in younger patients [42].

1.7 MOTIVATION FOR PRESENT STUDY AND STUDY AIMS

To be able to develop the best treatments for heart valve replacement, the basic science and mechanisms that are responsible for the success or failure of devices must be understood. To be able to properly design such devices to minimize the chances of failure, a complete understanding of the ultimate design goals is required. With heart valve replacements, the ultimate goal would be to design a permanent and functional prosthesis that would match the performance of the native valve. Thus, the key to development would be to dissect the inner-workings of the native valve and understand completely the relationship between its form and function. The tensile, biaxial, and bending properties of the aortic valves have already been established but an appreciation of the micromechanics has yet to be really explored. The relationship between the different layers and components of the valve obviously play a significant role in its gross behavior and should be explored. Analogously, by determining the behavior of the pulmonary valve in a parallel fashion, the two valves can be compared to each other. This comparison and contrast between the two valves will explain some of the adaptations undertaken by the native system to withstand low and high intravalvular pressures. The comparison will also benefit the paradigm behind the Ross procedure by helping to explain the relative success of the pulmonary valve in the aortic position.

No study yet performed has directly compared the native properties and states of the aortic and pulmonary valves with intent upon determining some of the differences inherent amongst its different layers. Most of the biological tissues that must be tested are very small in size and not conducive to normal testing methods such as tensile testing. Tensile tests are limited because of their single mode of deformation and the inability to accurately determine the cross-sectional area of tissues confounds what limited results may be found through these tests. It is intuitively obvious that the deformation of the valve leaflets *in vivo* are significantly more complicated than simple tension. For example, the heart valve leaflets do not undergo strictly tensile loading but experience a complex load that can be most accurately simplified as bending. Bending tissue thus provides a test more accurate to *in vivo* conditions while allowing for the physical constraints of small biological specimens. Fixation of tissues before experimentation irreparably damage and affects the tissue such that any properties that may be determined are vastly different from native properties and are applicable solely to the use of glutaraldehyde for fixative purposes.

To determine micromechanical tissue properties, new experimental approaches must be developed. Currently available tools such as tensile testers and biaxial devices are suitable for determining gross tissue behavior and allowing inferences to be made of micromechanical behavior. However, to make meaningful measurements towards determining micromechanical behavior, direct observation of changes in the structure of the tissue with deformation must be made. This is especially important when dealing with a composite material such as the heart valve leaflet because compositional changes most likely dictate the overall behavior.

To expand upon the biomechanical studies on the aortic and pulmonary leaflets, this study was designed to explore the behavior of the leaflets as a whole as well as a level of complexity between the gross behavior of the entire leaflet and the microscopic happenings of their cells. By understanding the mechanics of the leaflet and the influence its internal components have upon the mechanics of the entire leaflet, an appreciation of their contributions to its remarkable function can drive future developments by prioritizing the critical components.

The use of flexure in these experiments in addition to biaxial deformation sought to emphasize the behavior and deformation of the valve *in vivo*. During its normal operation, the leaflets deform significantly in flexure to accommodate the flow of blood or the presence of the other leaflets when sealed. The exploration of the differences in the bending and biaxial properties of the aortic and pulmonary leaflets stems from a desire to compare how the properties vary with respect to mechanical load. Because of the great difference in operating environments between the two leaflets, some differences must be inherent in their behavior to account for this.

The specific aims for this Thesis are:

1. Development of a novel flexural testing device for heart valve leaflets.
2. Application of the flexural device to the study of the micromechanics of the native AV and PV leaflet tissues.
3. To compare tensile and flexural responses, conduct the first study of the native PV under biaxial loading using a comprehensive biaxial mechanical protocol.

2.0 METHODS

As discussed in Chapter 1, the design of this study was aimed towards the determination of the behavior of the aortic and pulmonary valve leaflets in flexure as a whole, the interactions between the three different layers of the leaflet, and the biaxial behavior of the pulmonary valve. As a mode of deformation, flexure was determined to be capable of capturing a higher level of complexity than simple tensile and biaxial testing.

Three-point bending is a testing method that attempts to duplicate a more intuitive mode of deformation of the *in vivo* leaflet . Figure 15 shows the setup of a three-point bend test. Two posts support the specimen while a bending bar at the center of the tissue applies force to flex the tissue. The load is measured by recording the displacement of the pre-calibrated bending bar. A reference rod is located within view of the bending bar so that the displacement of the bar can be measured relative to a fixed point. Markers are affixed to the specimen with cyanoacrylate so that they can be tracked using a video camera system. Markers are also affixed to the bending bar, reference rod, and first and second posts and are all tracked by the marker tracking software [26]. This method of flexure testing is effective at causing large deformations in the tissue but does so by generating a large artifact where the tissue contacts the bending bar leading to inaccuracies in measurements made around the center of the tissue. The bending bar also alters natural flexural behavior of the tissue by forcing the leaflet strip to flex around the bar.

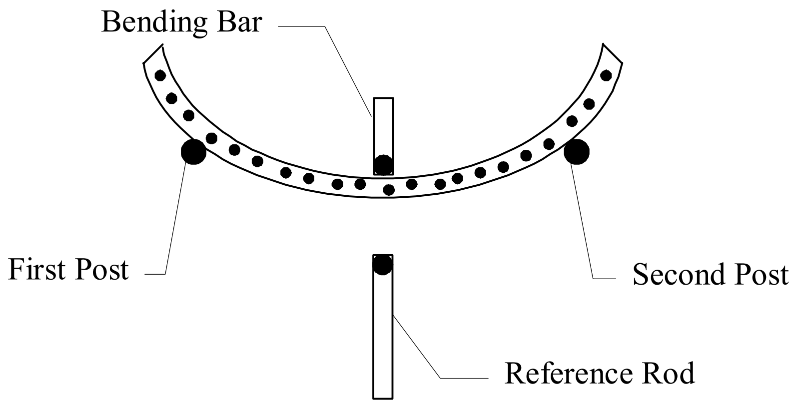

Figure 15, Schematic illustrating the concept of three-point bending and its application in testing soft tissues in flexure in previous studies. The reference rod provides a marker to reference the initial position of the bending bar for the calculation of the force applied. The bending bar cannot be referenced to the post markers because it is mounted upon a moving stage along with the reference rod. The black dots on the beam are markers for determining the curvature of the beam.

No study performed has directly compared the native properties and states of the aortic and pulmonary valve with intent upon determining some of the differences inherent amongst its different layers. Most of the biological tissues that must be tested are very small in size and not conducive to normal testing methods such as tensile testing. Tensile tests are limited because of their single mode of deformation and the inability to accurately determine the cross-sectional area of tissues confounds what limited results may be found through these tests. It is intuitively obvious that the deformation of the valve leaflets *in vivo* are significantly more complicated than simple tension For example, the heart valve leaflets do not undergo strictly tensile loading but experience a complex load that can be most accurately simplified as bending. Bending tissue thus provides a test more accurate to *in vivo* conditions while allowing for the physical constraints of small biological specimens. Fixation of tissues before experimentation irreparably damages and affects the tissue such that any properties that may be determined are vastly different from native properties and are applicable solely to the use of glutaraldehyde for fixative purposes.

Modification of the above flexural method, as described below, allowed for the measurements to be taken to determine the micromechanical behavior of the tissue and consequently the behavior of the leaflet layers. Biaxial experiments were performed on pulmonary valve, as well as the aortic valve for completeness, to determine base-line biaxial behavior that was not thoroughly established enough in the literature.

2.1 BENDING BEAM THEORY

2.1.1 Experimental rationale

For practical reasons, the intact leaflet was not tested as a whole in flexure but was simplified and idealized with a circumferentially oriented strip of tissue that was removed from the leaflet (Fig. 28). The leaflet strips used in testing were modeled using an elastic beam capable of large deformations and referred to in general as an 'elastica' [63]. Through experimentation the stiffness of the leaflet specimen was determined along with information about the relative movement of the layers of the tissue.

2.1.2 Elastic beam theory

When a column buckles under an end-load directed along its long axis, the beam will bend into a shape referred to as an elastica if allowed to freely rotate at both ends [63]. This buckling beam configuration was adapted for use as a horizontally oriented beam to permit the application of a load (P) along the long axis of the beam (Fig. 16). With increasing load, the elastica would flex in an approximately parabolic shape and the straight-line distance between its two ends, L, would decrease and the vertical distance between the midpoint of the beam and the ends, y, would increase.

The stiffness of the elastica was computed from the moment applied to the beam and the curvature attained by the beam. In the following we employed the moment-curvature relationship established by Bernoulli and Euler (Eq. 1):

$$M = E_{eff} I(\kappa - \kappa_0) \qquad (1)$$

Here: M: the moment applied to the elastica, E_{eff}: the effective stiffness of the tissue, I: the second moment of the area, κ and κ_0: curvature and initial curvature. The moment applied to the beam was determined at the middle of the beam and was defined as the product of the load applied with the vertical displacement of the midpoint, M=Py. The second moment of the area was defined for a rectangular cross-section and calculated using the following where: t: specimen thickness, and W: specimen width.

$$I = \frac{1}{12} t^3 W \qquad (2)$$

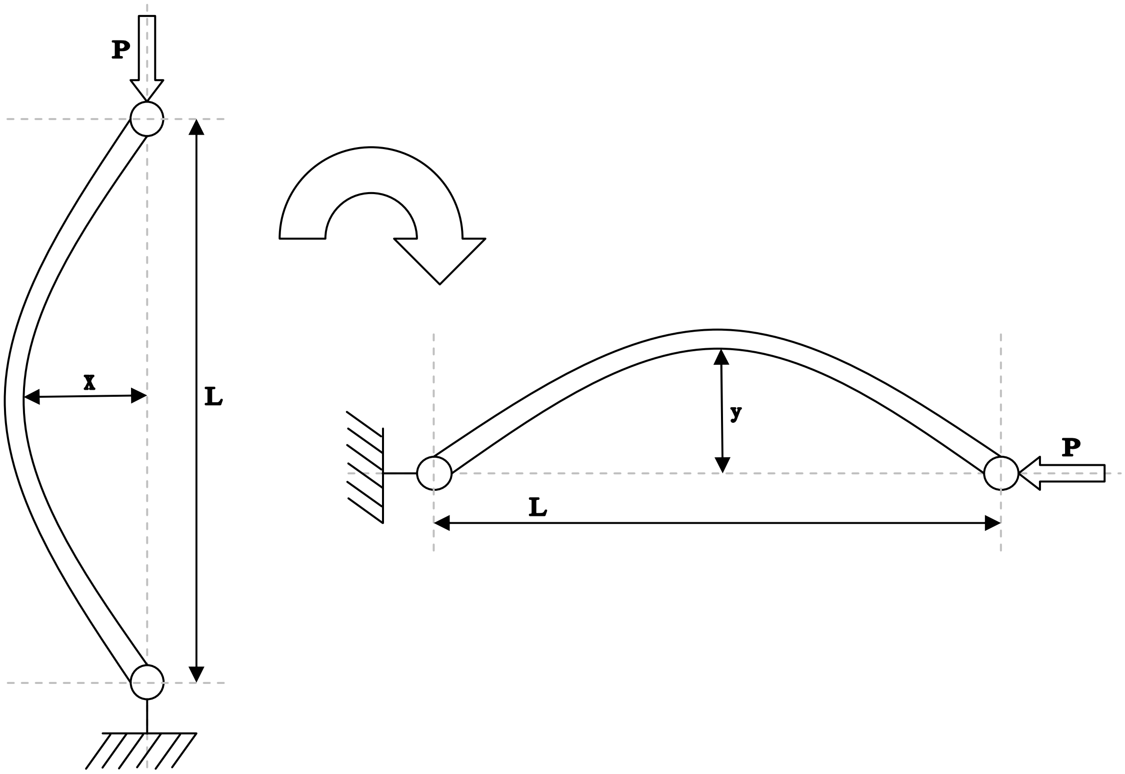

Figure 16, A free body diagram depicting the idealized tissue mounted in the testing device with a force applied to its free end, P, via a pre-calibrated bending bar. The other end of the tissue is securely affixed to the specimen bath. The moment arm for the center of the tissue is represented as y and the horizontal distance between the two ends of the tissue is L.

2.1.3 Composite bending beam theory

The effects of tissue mechanical property heterogeneity can be more easily understood by assuming the leaflet specimens to be idealized as a composite beam consisting of two layers. These layers are attributable to the ventricularis and fibrosa layer with the spongiosa layer omitted since it likely contributes negligibly to leaflet stiffness. Composite beams in flexure behave differently than isotropic beams because of the differences in material response between the layers (Fig. 17).

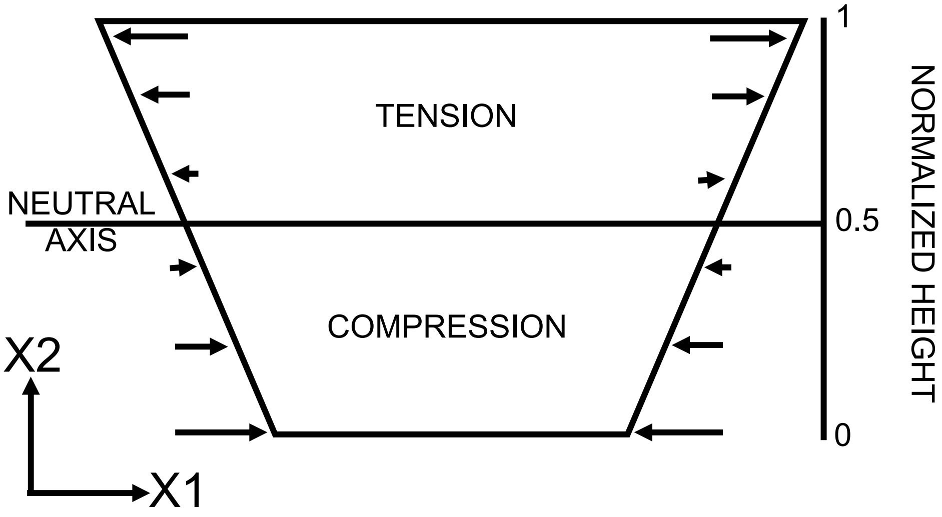

Figure 17, Schematic showing the distribution of forces throughout an isotropic beam. In this orientation, the beam is flexed upwards to form an upside-down U.

Following the conventions of figure 15, the top half of the beam experiences compressive forces while the bottom half of the beam experiences tensile forces. If the beam were to bend towards the opposite direction, the compressive and tensile forces would subsequently be reversed. The location along the thickness of the beam where no strains are present was referred to as the neutral axis. Thus, for the isotropic beam in figure 13, the neutral axis was located halfway through the beam because every layer of the beam possessed the same compressive and tensile moduli. As the material properties of the different layers deviated from each other, the location of the neutral axis and the distribution of strains through the thickness of the beam also changed. The neutral axis tends to move towards the stiffer layer (higher compressive and tensile moduli) because the stresses shared amongst the layers in the beam shift away from the weaker layers. Thus, the location of the neutral axis provides information about the relative stiffnesses of the layers found in the beam. The beam can also be flexed in both directions to subject all the layers of the beam to variations of tension and compression. Changes in the location of the neutral axis between bending directions reveal any differences that may be present between the compressive and tensile moduli of each of the layers [63]. Thus, the relative differences in layer stiffness may be obtained without any direct modification to the layers. A novel bending device was developed to investigate these phenomena in the leaflet tissues, as described in the next section.

2.2 BENDING DEVICE DESIGN

A new material testing device was designed and built in order to investigate the flexural behavior of native aortic and pulmonary porcine valve leaflets. This device was engineered to automatically perform several complicated tasks simultaneously to reduce the interaction of the user with the testing protocol to reduce the possibility of user-induced artifacts, expediting tests to increase efficiency and throughput, and enhancing the accuracy, resolution, and repeatability of tests.

2.2.1 Imaging

The bending device consists of two modules that work simultaneously via computer control to capture macroscopic and microscopic digital images (Fig. 18). The macroscopic images were processed in real-time to determine the effective modulus of the tissue specimen as a whole. The microscopic images were captured and stored in the computer so that they could be processed later to determine the transmural strains. The side of the tissue imaged by the macroscopic lens system will be referred to as the macroscopic side and the side of the tissue imaged by the microscopic lens system will be referred to as the microscopic side.

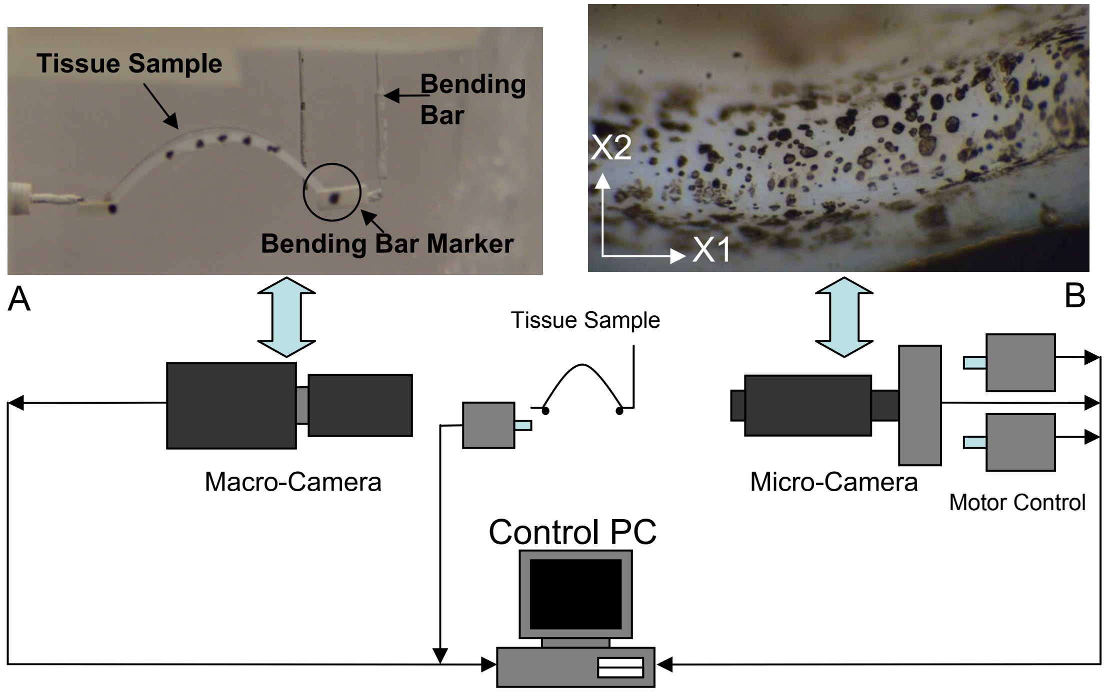

Figure 18, A schematic detailing the major components of the new bending device. The macro camera is securely affixed to the platform the device is mounted upon. 'A' represents the view obtained from the macro camera during testing. The image is thresholded to isolate black objects from the white background. Two metal sleeves are glued to the ends of the tissue so that it can be mounted onto a post attached to the sample bath and onto a post located on the bending bar. The vertical bar located next to the bending bar is used to mark the location of the bending bar marker when the tissue is not attached. The tissue sample is contained within a bath and mounted on a computer controlled servo stage. The micro camera is mounted to two servo stages to enable it to move in a plane parallel with the view seen in the macro camera. 'B' represents one of the images obtained using the micro camera. The black markers seen on the edge of the tissue have been applied using an airbrush. The image is post-processed to identify and locate the markers so that their displacement from the reference state to the deformed state can be quantified and used for strain analysis. The X1 axis coincides with the circumferential direction of the leaflet. The X2 axis coincides with the thickness of the leaflet.

2.2.1.1 Macroscoping imaging The macroscopic imaging system takes images of the macroscopic side of the tissue as it is flexed as illustrated in figure 19. A tele-centric lens attached to a 640 by 480 pixel resolution CCD camera (Sony XC-1) is used to image the tissue along the macroscopic edge. A National Instruments (PCI-1407) video capture board is used to feed the video images into the computer and controlling Labview program. Through Labview provided image thresholding routines, black markers are isolated from a white background and identified by the computer as seen in figure 20.

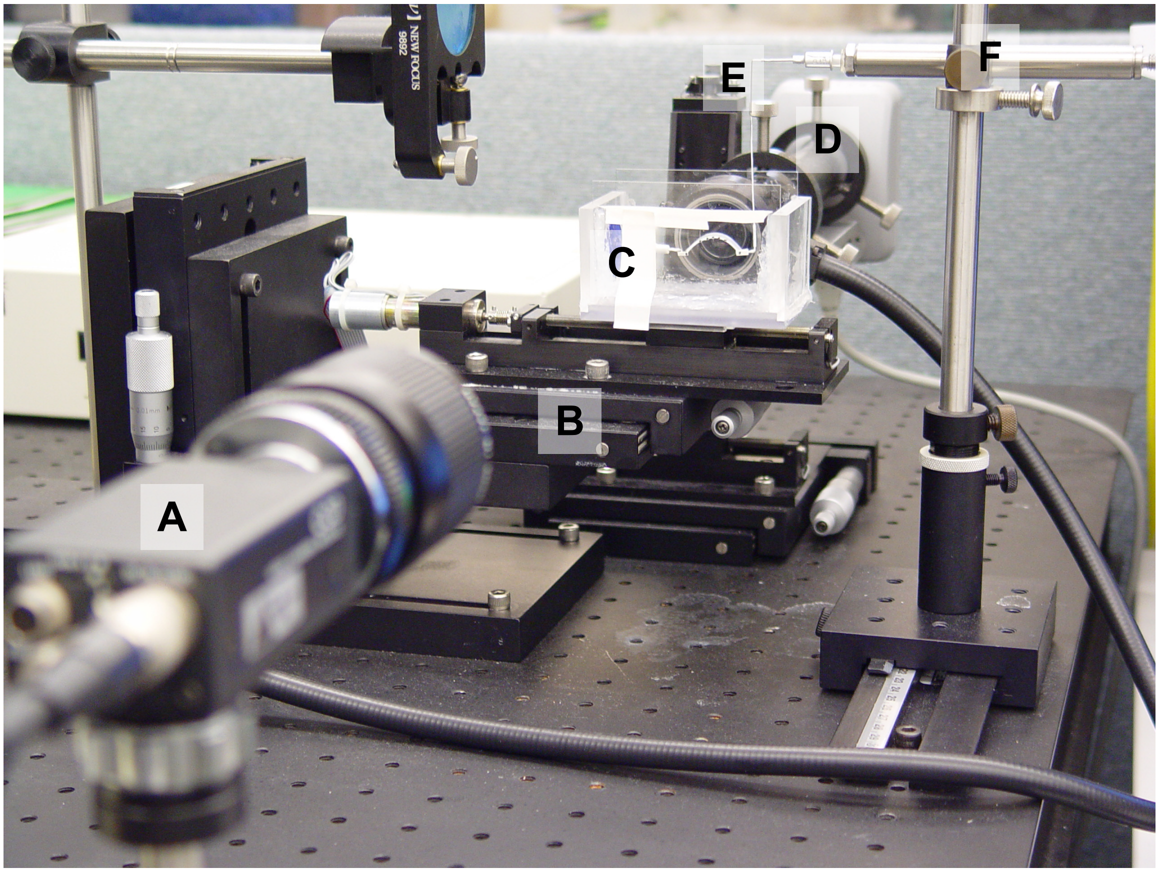

Figure 19, Photograph of actual device from the point of view of the (A) macro-imaging camera which is located in the foreground. The (B) testing stage and the (C) specimen bath are located directly in front of the macro-imaging camera's line of sight and the (D) micro-imaging camera is located directly behind the specimen bath. The (E) bending bar is suspended into the specimen bath from the (F) crane assembly located at the right.

Two different groups of markers are located in each image. The first group of markers represents the posts that are attached to the ends of the specimen. The first post is located at the left end of the tissue specimen and is fixed to the specimen bath. The second post is affixed to the right end of the tissue specimen and is attached to the bending bar. The remaining markers are those that are attached to the specimen and are used to determine the shape of the specimen throughout testing. The tissue specimen mounted upon the posts and suspended within the bath can be seen in figure 21. Both posts were either attached to the ends of the specimen or attached upon the surface of the specimen. The location of the posts was deemed to be insignificant according to previous tests that were completed comparing different post attachment locations. Agreement was found between the data obtained from specimens with posts attached to the end and to the surface of the specimen.

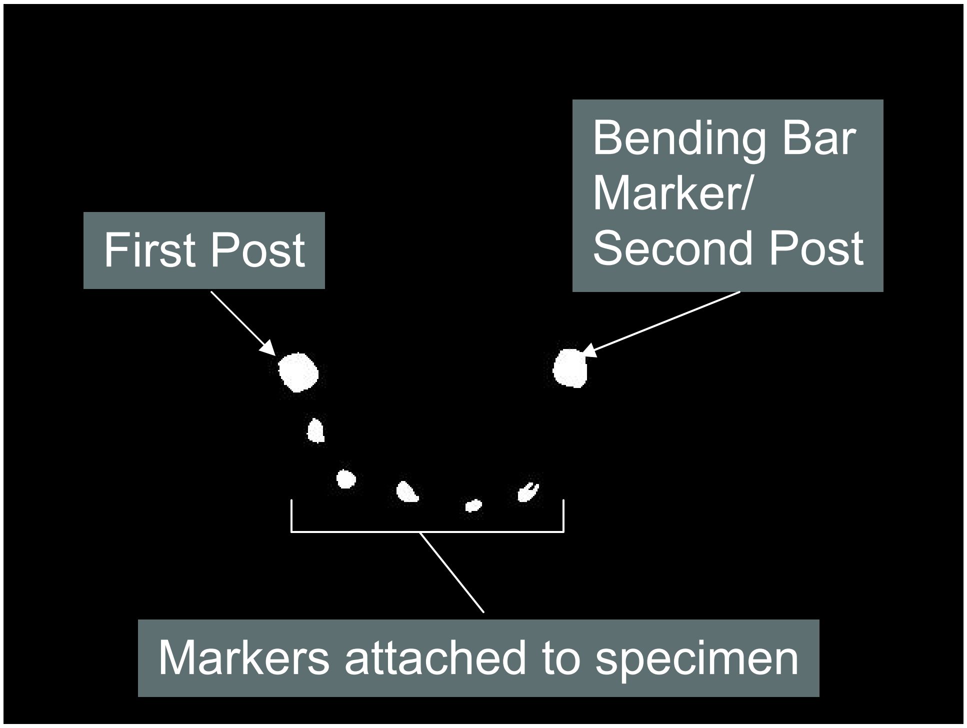

Figure 20, Digitized photograph illustrating the different markers detected and tracked by the computer software.

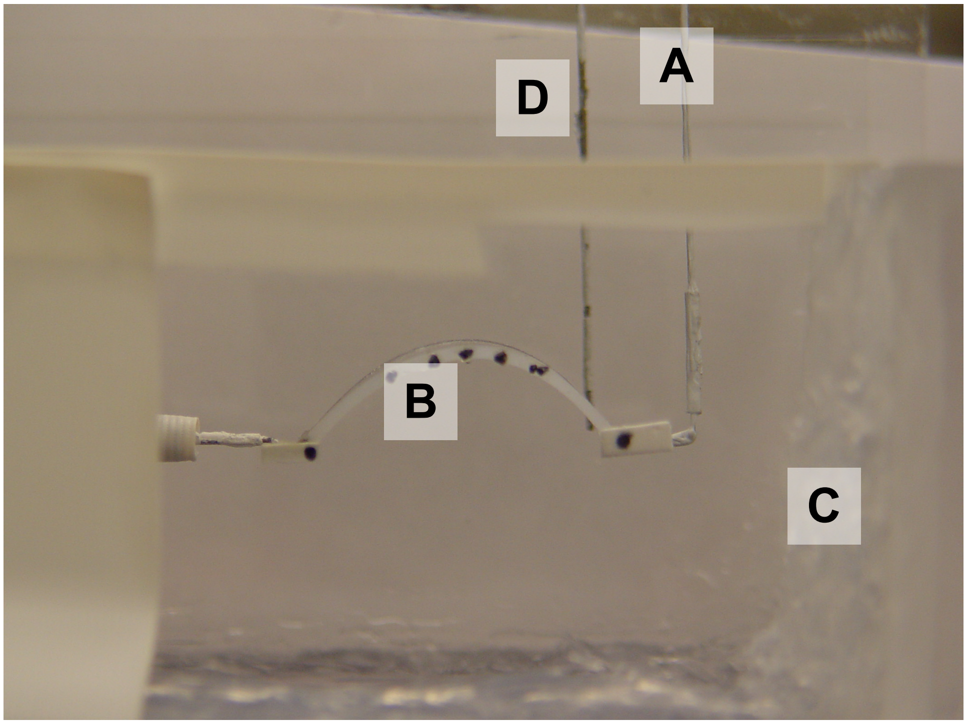

Figure 21, Photograph demonstrating the view from the macro-imaging camera. Note that this is not an actual image taken by the camera. The (A) bending bar is attached to the (B) sample and is suspended into the (C) bath on the right. The (D) bar to the left of the bending bar was used for initializing the initial position of the bending bar marker.

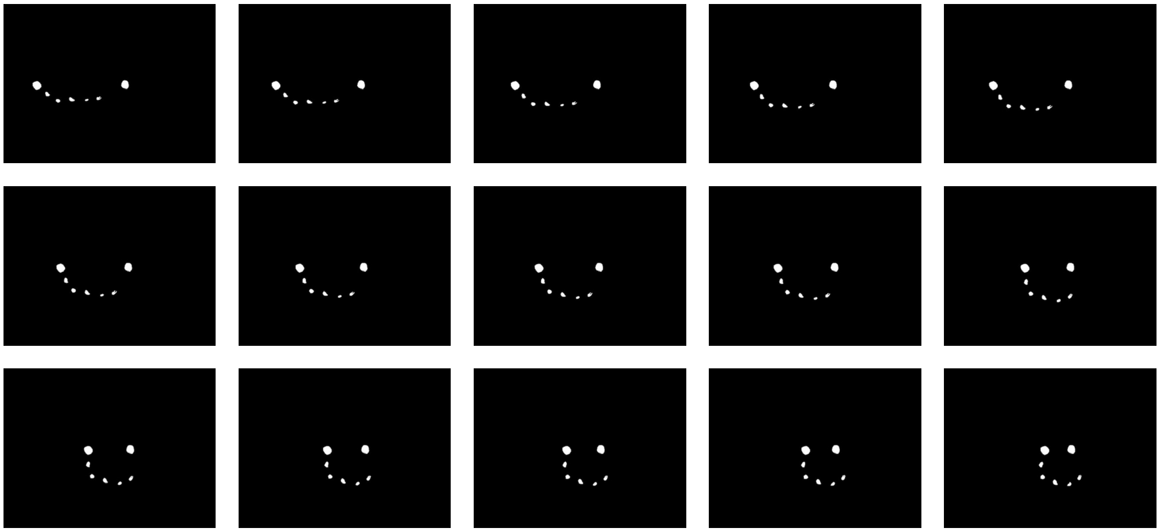

Figure 22, Image sequence demonstrating the markers detected by the imaging software as well as the movement of the markers and the shape of the tissue during the flexure test. Progression of the test begins at the upper left and moves towards the lower right.

The two groups of markers were tracked throughout the experiment and were identified according to a set of algorithms. The subroutines used by Labview to find particles in an image do so from top to bottom, so that the markers must be sorted accordingly to work with the Labview software. Before the experiment begins, the tissue is approximately straight but does not necessarily have to be perfectly straight (Fig. 22). Thus the markers and the two posts are roughly collinear. As the specimen bath moves towards the bending bar and the tissue deforms, it begins to take upon a curved shape. The direction the tissue bends towards is pre-determined and specified by the user. The coordinates of all the identified markers are translated into polar coordinates for differentiation and identification. These coordinates are then referenced to a specific point which roughly translates to the center or focus of the curve formed. This point is determined by taking the x coordinate component as the average between the maximum and minimum of the x coordinates detected. The y coordinate component is taken to be either the lowest y value if the tissue was flexed upwards or the greatest y value if the tissue were to be flexed downwards (Fig 23). Using this focal point as a reference for all of the polar coordinate marker positions, the points can be identified by the theta component of the polar coordinate. The second post is found within the first quadrant (I) and the first post is found roughly within the fourth quadrant (IV). The remaining markers detected are those affixed to the tissue are ordered according to the magnitude of their theta component.

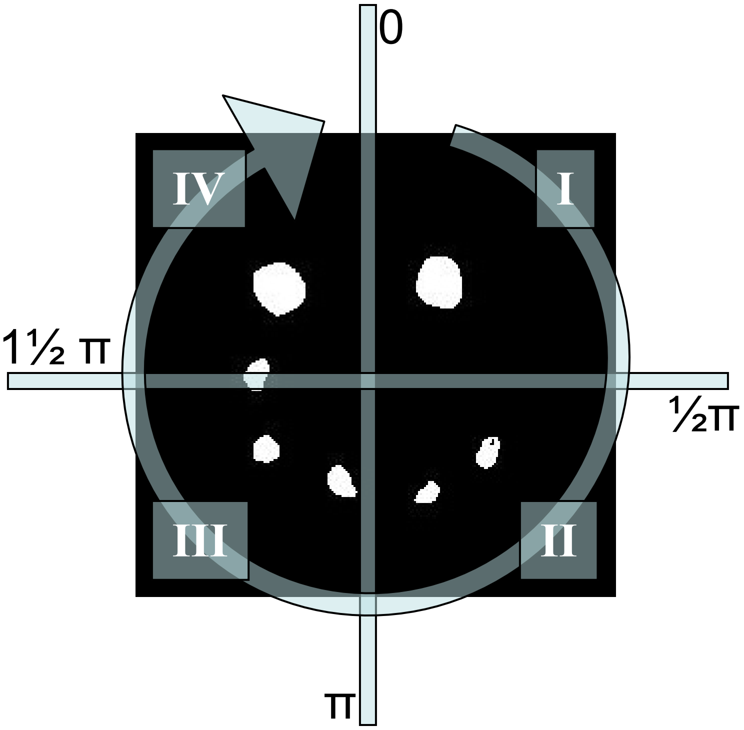

Figure 23, Schematic illustrating the algorithm used to sort the markers detected by the marker detection software included with Labview.

2.2.1.2 Microscopic imaging The microscopic images are taken with a high magnification lens (Edmund Optics, VZM-1000i) mounted to a one megapixel resolution (1280 pixels by 1024 pixels) color CMOS camera (PixeLink PL-A662) attached to the computer via a IEEE-1394 interface. As the tissue is flexed, the user prompts the system to pause and control of the system diverts from the real-time marker tracking to the microscopic lens. The images are taken of the microscopic side of the tissue.

When tests are performed, the tissue bends from its initial position to a curved shape approximated by the analysis software as a quadratic. The tissue is moved horizontally towards the bending bar by the movement of the entire tissue bath which is mounted upon a motorized stage (National Aperture MM-4M-EX-80) which will be referred to as the testing stage. This motorized stage and two others are responsible for all of the computer controlled movement performed by the testing software. They are all stepper motors connected to an amplifier unit (National Aperture MC-4SA MicroMini) that is then interfaced to the computer via a National Instruments NI-7344 board. The two other motorized stages (National Aperture MM-4M-EX-50 and MM-4M-F-50) are mounted upon each other and onto a custom machined mount for the high magnification lens as can be seen in figure 24. These two motors allow the computer to control the exact location of the camera throughout the test.

Because the area of interest on the microscopic side of the tissue moves throughout the test, it must be tracked accordingly so that it will remain within the field of view of the camera. This is accomplished by establishing the location of the high magnification lens camera as a function of the location of a specific marker on the tissue. In this study, strain measurements on the microscopic side of the tissue were taken at the center of the specimen. Thus, the marker placed on the macroscopic side of the tissue was designated as the tracking marker. At the onset of testing, the position of the tracking marker was determined by the software and stored. As the tissue moves throughout the test, the location of the marker is continually updated within the system. Its translation in the x and y axes is converted to steps for the x and y stepper motors to move. To determine the conversion from millimeters of movement on camera to motor steps, a calibration program was written that counted the number of steps moved by a motor for a given amount of displacement on-camera. Thus, after initially positioning the lens to the appropriate area of interest, the motors will move the lens and camera assembly throughout the test, maintaining the same area of interest.

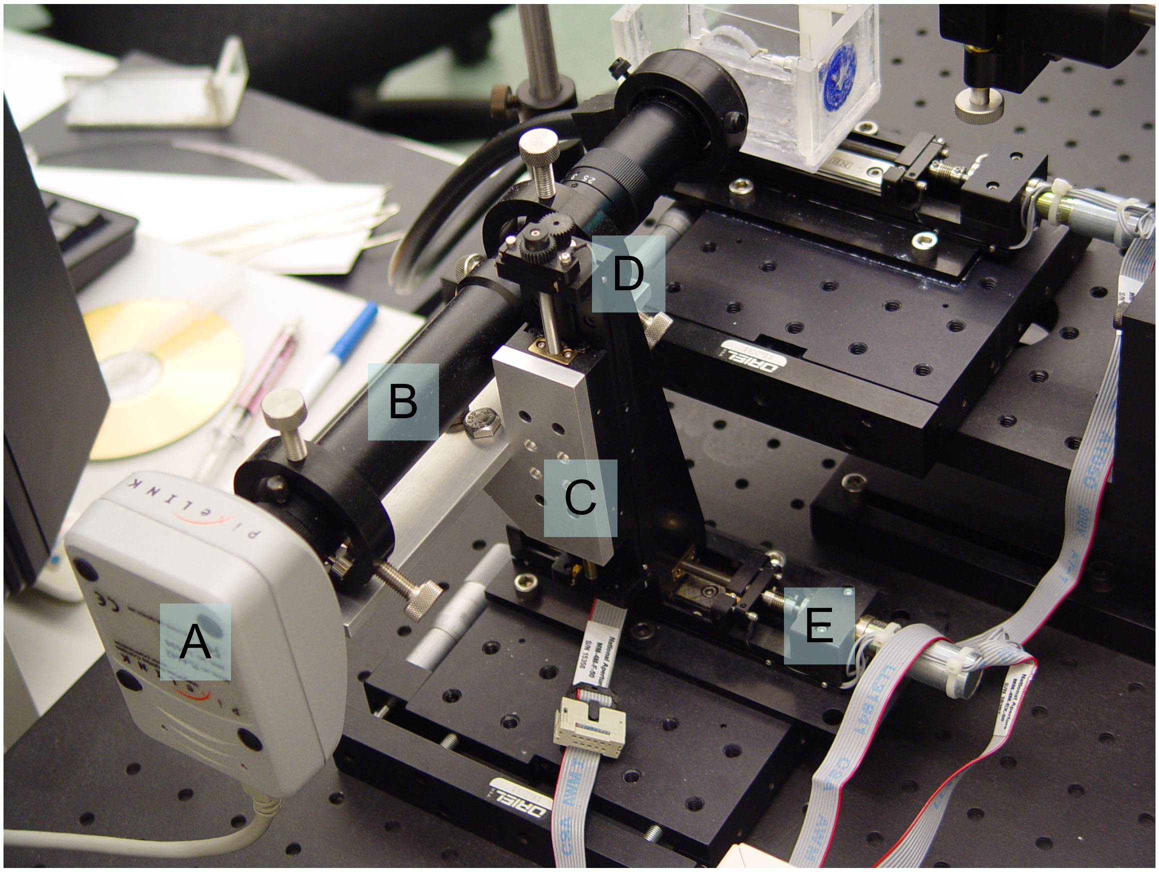

Figure 24, Photograph detail of the micro-camera imaging system. The gray box at the left is the Firewire CMOS camera. It is attached to the magnification tube which is then attached to an aluminum bracket attached to a vertically mounted servo stage. The vertical servo stage was then mounted upon another servo stage at the bottom for left and right movement.

2.2.2 Testing software

A screenshot of the testing software GUI can be seen in figure 25. This custom Labview software walks the user through three different stages to complete a single test. The first stage involves the initialization of testing parameters. The algorithms used for determining and classifying marker positions requires that the user stipulate towards which direction the tissue is being flexed. The tissue can either be flexed upwards, so that it is concave down, or flexed downwards so that it is concave up. Repeatability experiments were performed to confirm that bending the tissue upwards or downwards did not affect the results obtained. The condition for ending the test must also be provided by the user. Tests are terminated when the two posts reach a predetermined distance from each other or when the tissue attains a predetermined curvature. All of the tests performed in this study were done so under curvature control so that tissue properties could be determined as a function of the curvature of the tissue. The testing stage can be adjusted at this point to ensure that no force is being exerted upon the bending bar by the tissue and vice versa. This is accomplished by using a thin steel bar that can be dropped in and out of the testing bath by using a high-accuracy swivel mount. The placement of the steel bar is matched with that of the unloaded bending bar in the macroscopic image. When the tissue is attached to the bending bar, the displacement of the bar changes from its unloaded state. The testing stage is manually adjusted via the software so that the bending bar will again coincide with the drop-down calibration bar. This ensures that the tissue is at an unloaded state.

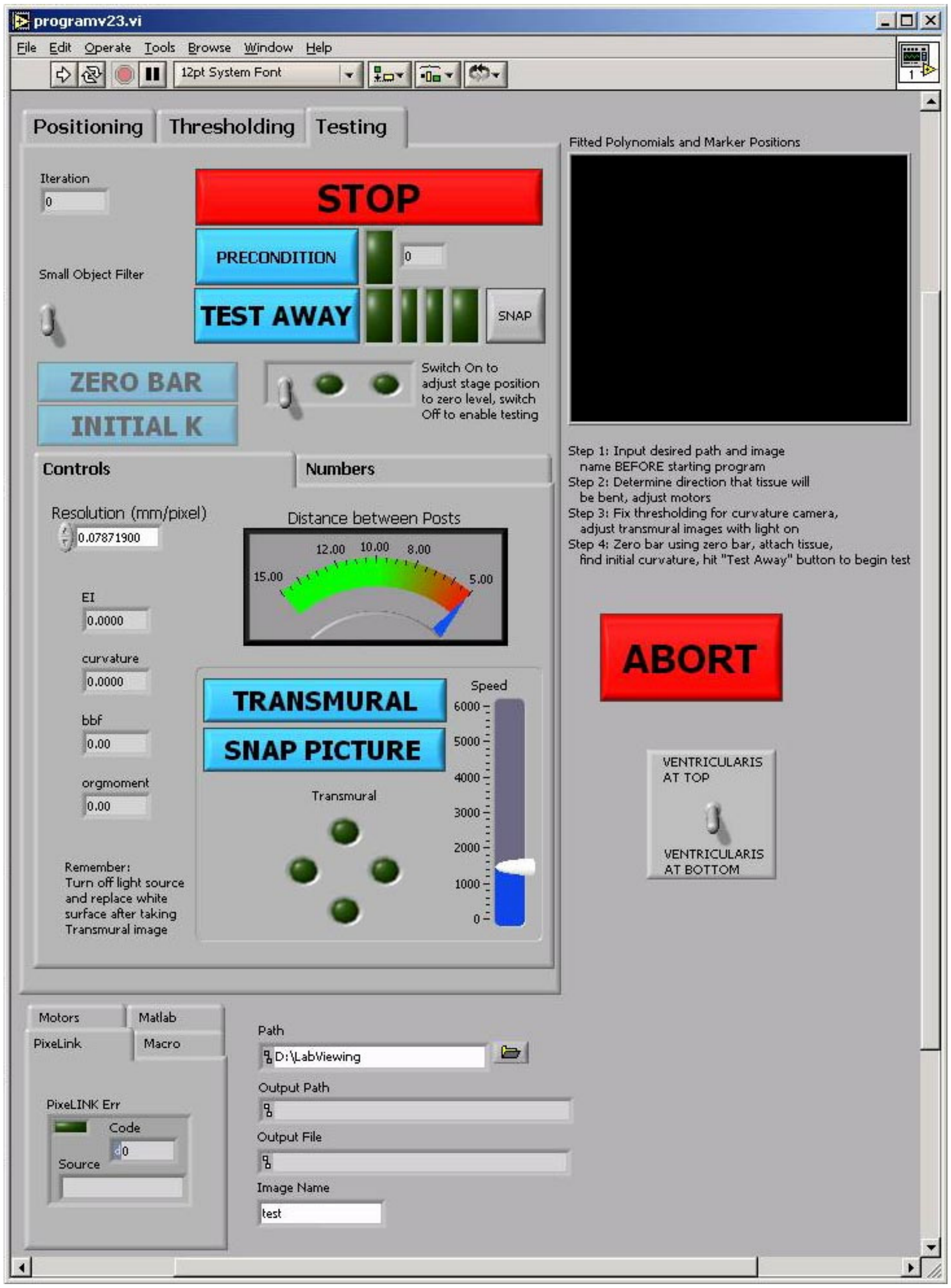

Iteration: 0

Switch On to adjust stage position to zero level, switch Off to enable testing

Resolution (mm/pixel): 0.07871900

EI: 0.0000

curvature: 0.0000

bbf: 0.00

orgmoment: 0.00

Remember: Turn off light source and replace white surface after taking Transmural image

Step 1: Input desired path and image name BEFORE starting program
Step 2: Determine direction that tissue will be bent, adjust motors
Step 3: Fix thresholding for curvature camera, adjust transmural images with light on
Step 4: Zero bar using zero bar, attach tissue, find initial curvature, hit "Test Away" button to begin test

Code: 0

Source:

Path: D:\LabViewing

Image Name: test

Figure 25, A sample screen shot of the testing software GUI developed to control and orchestrate the different components of the testing device.

The second step of testing involves the setup of the video in the macroscopic and microscopic cameras. A live video feed is displayed from the CMOS camera and control of the two positioning motors is surrendered to the user. This allows for the precise positioning of the high magnification lens at the area of interest. The exposure length of the CMOS can be adjusted through the software. The high magnification lens possesses a manual iris adjustment for depth of field and lighting corrections. It is also at this stage that an initial image of the microscopic side of the tissue is taken. This image serves as the reference state for all of the markers that will be subsequently identified. Imaging thresholds can be adjusted at this point to obtain an appropriate image for the macroscopic camera. The markers placed upon the tissue must be isolated from the background. This is accomplished by keeping the tissue bath white. The tissue is naturally white as well and whatever components that are present and that are not white are masked away from the image. The thresholding isolates all of the black objects in the image so that Labview subroutines can then identify them. It is these identified objects that are then passed to the marker identification and sorting routines.

The third stage of testing is the part of the test program where the test is performed. The initial curvature of the tissue is stored by the program into memory so that the difference in curvature throughout the test can be properly computed. The force exerted by the bending bar upon the tissue is determined by the location of the second post marker. This marker is physically attached to the bending bar and its translation in the x direction can be detected by the testing software. The position of the bending bar marker is recorded and initialized to zero so that subsequent movement of the marker away from the other marker will be recorded as a displacement. As previously discussed, each individual bending bar is pre-calibrated so that it will exert a force proportional to its displacement. Thus, the displacement detected by the software can be interpreted into a proportional load. Initiation of testing transfers control to the software and the testing regimen. The testing stage stepper motor begins to move in increments towards the bending bar. At the pause between every increment, the software records a thresholded image of the markers detected by the macroscopic camera. Measurements of force, curvature, and marker positions are all obtained with every repetition of the testing loop. These values are saved to a file for future analysis. When the tissue reaches the pre-determined test termination condition (ie the pre-determined distance between the two posts or the set curvature of the tissue) than the software ceases movement of the testing stage and displays the video image from the microscopic side of the tissue. The position of the high magnification lens may be adjusted to ensure that the entire area of interest is captured. Adjustments to the focus may then be necessary to maintain the same distance between the tissue specimen and the high magnification lens. Images are captured by the user and referred to as the deformed state for later analysis. When the deformed images have been stored, the program is allowed to terminate whereupon it will return the high magnification lens and the testing stage to their initial positions.

2.2.3 Load measurement

The measurement of the miniscule forces encountered with native tissue was accomplished in an accurate and dependable manner by adapting the bending bar method used in three-point bending. The bending bars were made of 316V stainless steel in varying diameters. The diameter of the bar determined the amount of force produced by the bar as a function of the bar's displacement. This method of measuring force was convenient because it avoided the necessity of using expensive load cells that had to be constantly calibrated and maintained. The bending bars were also repeatedly accurate as determined by calibrations performed before and after testing regimens. The tissue was attached to the ends of the bending bars by sliding the sleeve attached to the tissue over a post attached to the end of the bending bar. The steel wire used to make the posts was chosen to be significantly thicker than that of the bending bar to ensure any deformations in the bar would not occur in the post assembly. These posts were attached to the bending bar by crimping them using another length of steel tubing. Calibrations of the bending bars were performed with the entire post assembly attached to ensure accuracy.

2.2.4 Repeatability, sensitivity, and accuracy

The difficulty in performing accuracy studies was encountered in locating reference materials possessing similar traits as the native leaflet material. The novelty of exploring material behavior and characteristics using flexure was in itself a difficulty because of the lack of any materials whose bending properties had been fully established. To this researcher's knowledge, there were no materials available that possessed a similar tensile strength and extensibility that were not themselves biological materials as well. In addition the availability of such a material possessing significantly different layer properties was also non-existent. Thus, a silicone rubber was obtained that possessed a relatively low modulus as well as dimensions approximating those of the native aortic leaflet.

The load displacement relationship of the bending bars was pre-determined using a microscale and a moveable platform that had been calibrated to a micrometer. Figure 26 illustrates the setup used to calibrate the bending bars. The force the bar exerted upon the scale was determined at zero displacement of the bar. The bar was then displaced along regular intervals and force measurements were taken. The load displacement response of the bars was linear so a linear equation was fit (Figure 27). Thus, for any given amount of bar displacement, the load could be accurately determined. The calibration for each bending bar was determined before and after batteries of tests to ensure that repeated deformations of the bar did not influence the load-displacement relationship and alter data.

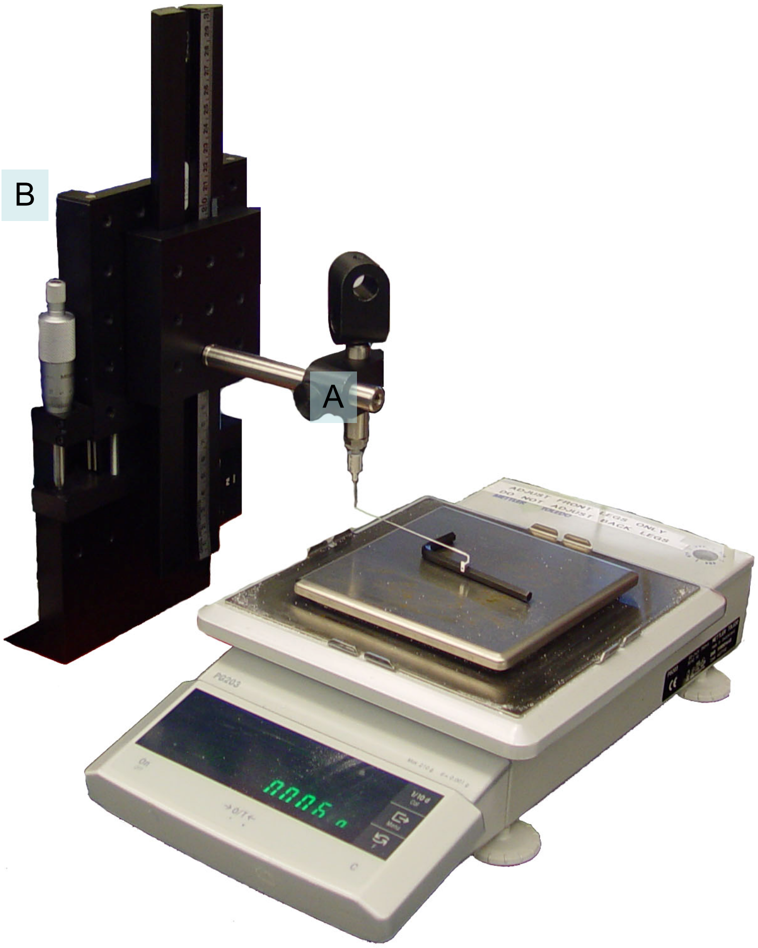

Figure 26, Picture of the setup used to calibrate the bending bars (A) used for load measurement. The deflection of the bending bar was increased by adjusting the caliper (B) attached to the stage.

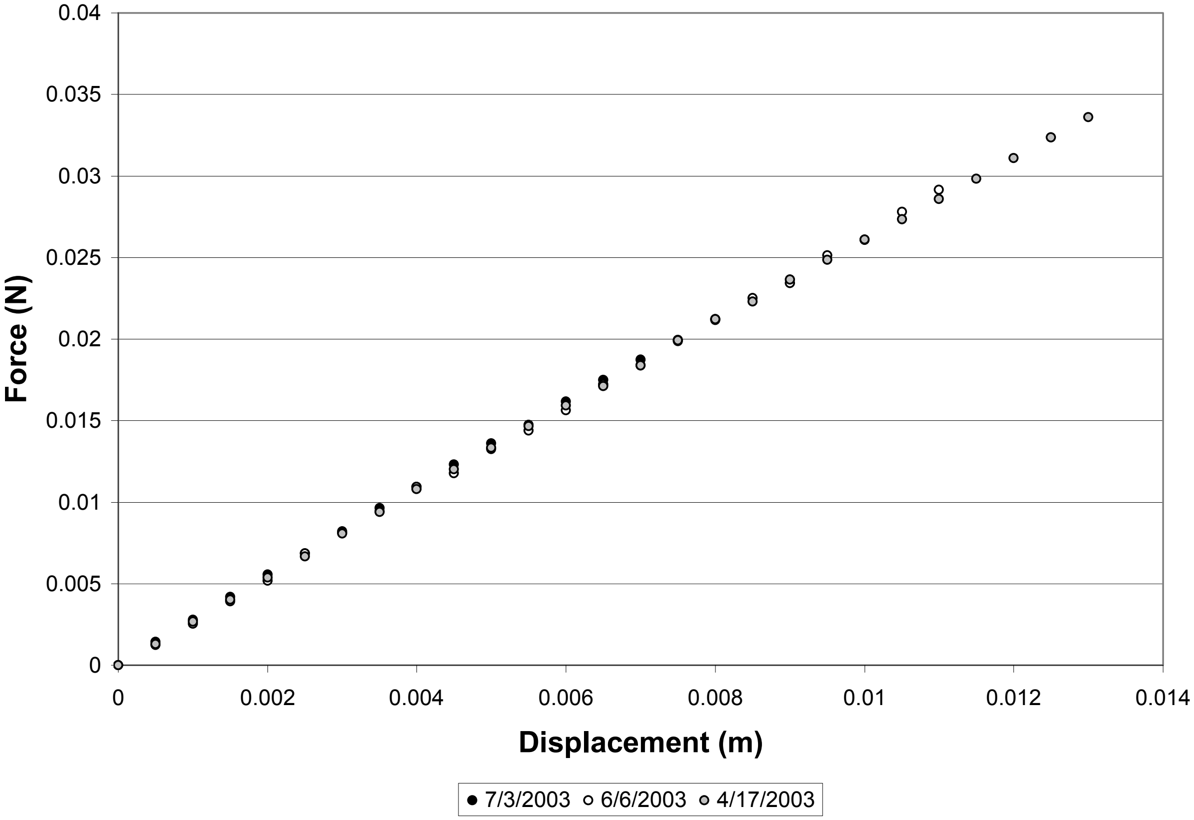

Figure 27, Example plot demonstrating the linear trends determined from calibrating bending bar displacement with force exerted upon them. Calibrations were made at three different time points during which tests were being run on the flexural device.

Studies were performed to ensure the data obtained from the testing device was accurate and repeatable. To do so, the translucent silicone material was tested with the bending device and a tensile testing device to compare and confirm the accurate prediction of the effective stiffness. Strips of the silicone rubber with a thickness of approximately 790 microns were tested using a MTS Tytron 250 Mechanical Test System. The silicone sheets were prepared to the same dimensions used for the valve studies and markered identically. Repeatability was determined by flexing silicone specimens in different bending directions (specimen flexed upwards and downwards for each side of the specimen) forty times and averaging the moduli obtained. This ensured that results obtained from one bend test to another were identical and that mounting and unmounting the samples from the bending device did not influence its accuracy.

2.3 TESTING METHODS

Aortic and pulmonary valve leaflet specimens used for bend testing were obtained from porcine hearts harvested at a local abattoir. Within five hours of acquiring the hearts, the aortic and pulmonary valves were separated from the heart and stored separately in PBS: 8.08 g NaCl, 0.56 g KH_2PO_4, and 2.42 g Na_2HPO_4 in 1 L H_2O. The valves were then placed into a freezer at 30 C. Within a week of freezing the valves, they were removed from the freezer and allowed to thaw to room temperature before the leaflets were dissected from the valve and tested in the bending device. The leaflets were removed from the root by using a scalpel to cut at the edges of the leaflet where they met the root. A very small graphite marker (approximately 0.5 mm in diameter) was glued with a very small amount of cyanoacrylate on the ventricularis so that the two different sides could be distinguished after the leaflet had been removed. The leaflet was then cut into a rectangular testing strip measuring approximately 14 mm in circumferential length and 3 mm in radial length measured using a sliding caliper. The location of the cuts placed the specimen strip below the nodulus of the leaflet and circumferentially oriented. This was performed by pressing a fresh razor blade into the tissue and cutting along the side of blade facing the tissue with a scalpel. Thickness measurements were then taken of the leaflet specimen using a rotating dial caliper at three different locations along the length of the tissue. The thickness was recorded immediately upon releasing the caliper upon the tissue and then three seconds later to compensate for the softness of the tissue. A small amount of cyanoacrylate was then used to attach a steel sleeve at each of the shorter ends of the tissue. This was done by laying the tissue flat upon the cutting surface and applying a droplet of cyanoacrylate to the edge. The steel sleeve was then pushed up against the tissue and allowed to affix to the tissue. This was done to both ends of the tissue. While attaching the steel sleeves, the tissue was kept hydrated by applying drops of PBS to the center of the tissue, but the ends of the tissue were kept dry so that the posts would adhere securely.

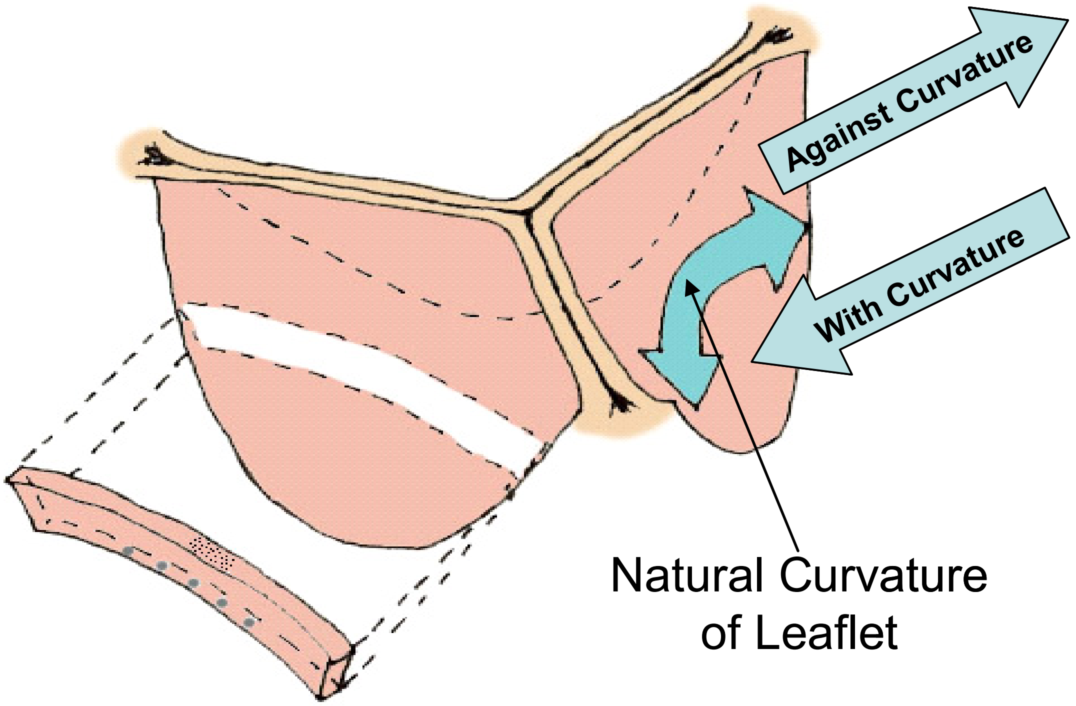

Figure 28, Schematic showing the orientation of the leaflet within the aortic root along with the difference between the AC and WC bending directions for the leaflet. Note that the natural curvature of the leaflet of interest is in the circumferential direction because all tissue samples were circumferential in orientation.

Five graphite markers were then attached to the edge of the tissue closest to the free edge of the leaflet by using a needle and small droplets of cyanoacrylate (Fig. 29). The tissue was then turned over so that the microscopic side was exposed. Markers for the transmural strain tracking were then applied. This was accomplished by first dabbing the side of the tissue dry. Using house air, an air brush was used to spray waterproof India ink onto the side of the tissue. To obtain a good coverage of markers across the area of interest, the tissue was sprayed for at least two minutes. The other portions of the tissue were masked off to prevent covering the entire tissue in black ink that would have interfered with the marker tracking software. Afterwards, the tissue was allowed to dry for another minute before it was immersed in the PBS solution. The tissue sample was then immediately transferred to the specimen bath in the testing device. The tissue was then mounted within the testing bath by sliding the sleeves attached to the tissue over the post in the specimen bath and the post at the end of the bending bar. The specimen bath was filled with the same PBS solution to ensure the neutral buoyancy of the specimen in the bath.

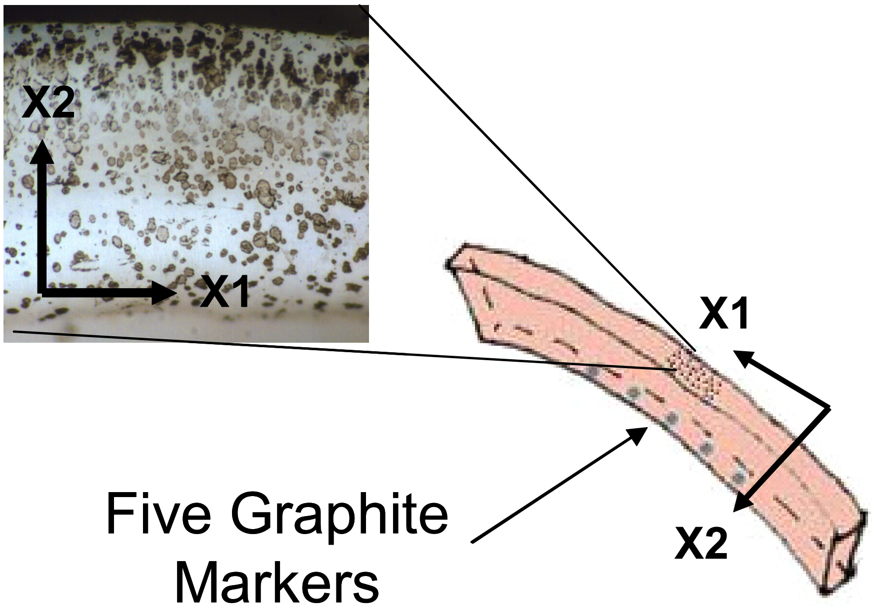

Figure 29, Graphite markers used by the macro-imaging system are shown on the edge of the leaflet specimen closer to the attachment edge. The airbrushed transmural strain markers used by the micro-imaging system are shown on the edge of the leaflet specimen closest to the free edge of the leaflet. The orientation of the X1 and X2 coordinate system specifies the X1 axis to be coincident with the circumferential direction of the leaflet and the X2 axis to reflect the thickness of the leaflet.

Each leaflet was tested for at least five repetitions in the against curvature (AC) and with curvature (WC) directions, illustrated in figure 26. The AC or WC directions are defined with respect to the natural curvature of the leaflets. *In vivo*, the leaflet is oriented with the ventricularis facing downwards and the fibrosa facing upwards while curving downwards towards the ventricle. The first three repetitions in each direction were performed without preconditioning. To precondition the tissue, it was flexed back and forth to its maximum curvature ten times. Afterwards, the two subsequent trials were performed and their results compared to the previous three results to determine any change in properties with conditioning. To determine any differences between performing tests in the AC direction first to performing tests in the WC direction first, both sets of tests were performed. Some AC or WC directions were repeated at the end of the test set to determine if the previously obtained results could be repeated. Any differences that may have occurred from the dissimilar protocols would have manifested in some change of properties. Pilot studies indicated no significant differences between the different testing protocols and it was determined that the order of testing did not have an impact upon the results. The testing software outputted a text file recording all of the data that was obtained during the test including, for every point tracked on the tissue, the coordinates, the change in curvature, the moment applied, the vertical displacement, and the force being exerted by the tissue upon the bending bar.

2.4 ANALYTICAL METHODS

2.4.1 Flexure analysis

The data obtained by the device and used for the flexural analysis included the positions of the macroscopic markers and the positions of the two posts. All measurements required to determine the curvature and stiffness of the tissue were obtained from these marker coordinates which were recorded to disk for analysis. Also, in remaining faithful to the desire to automate testing, all of the measurements from the marker coordinates were performed during the experiment and displayed to ensure variables remained within nominal operating boundaries.

The positions of the markers affixed to the tissue are fitted to a quadratic equation of the form of equation 3 using a general least squares method. This expression was found to be the most appropriate because of its ability to capture the general shape of the tissue without being overly complicated. From this equation, the curvature is determined using equation 4. The coefficients for the fitted quadratic along with the curvature are determined in real-time so that the curvature measurements could be used by the program for control purposes. Matlab math functions are used to perform these operations within the Labview program.

$$y = ax^2 + bx + c \tag{3}$$

$$\kappa = \frac{y''}{\left(1 + y'^2\right)^{\frac{3}{2}}} \tag{4}$$

The force applied to the tissue specimens is measured using pre-calibrated bending bars discussed earlier under load measurement. The position of the bending bar (post two) is recorded by the program at execution and used as a reference for the displacement of the bar during the experiment. The displacement of the bar along with its pre-determined calibration curve is then used to determine the amount of load being generated at the end of the leaflet specimen. The moment is calculated using this applied load along with the geometry of the leaflet specimen as determined by the markers tracked. Measurements are taken at the center of the specimen where a marker had been specifically placed and the moment equation was derived from the free body diagram of the tissue specimen (Eq. 5 and Fig. 30).

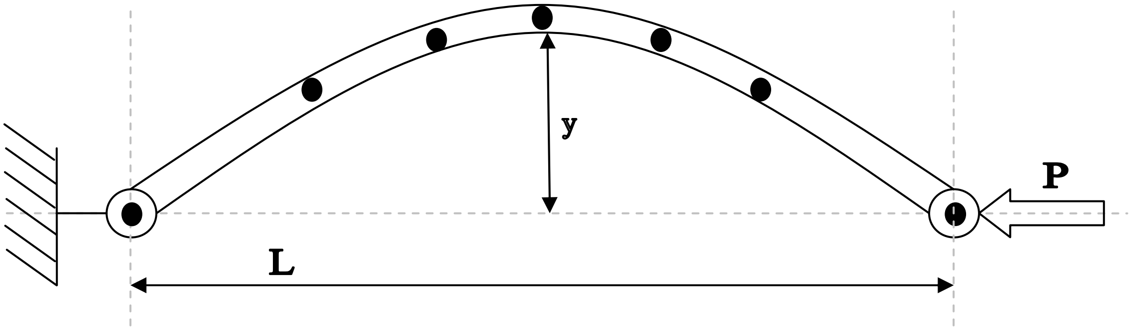

Figure 30, Free body diagram of the idealized tissue specimen during testing.

$$M = Py \tag{5}$$

Using the Bernoulli-Euler moment-curvature relation discussed earlier, equation 6, a correlation is made between the difference between the initial curvature, κ_0, and the current curvature, κ, and the effective stiffness, E_{eff}, and the second moment of inertia of the specimen, I. The second moment of inertia of the specimen is determined using equation 7 and the thickness of the specimen, t, and the width of the specimen, W. The effective stiffness of the leaflet specimen as a whole can be determined by rearranging equation 6 to obtain E_{eff}. Alternatively, a flexural rigidity can be determined as well by rearranging equation 6 to obtain $E_{eff}I$. This flexural rigidity is advantageous in some circumstances because it does not rely upon the dimension measurements required to obtain the moment of inertia. The flexural rigidity is also found as the slope of a moment curvature plot where the moment applied to the specimen is plotted against the change in curvature of the specimen (Fig. 30).

$$M = E_{eff} I(\kappa - \kappa_0) \qquad (6)$$

$$I = \frac{1}{12} t^3 W \qquad (7)$$

2.4.2 Transmural strain determination

Data extracted from the transmural images taken from the experiment consist of the coordinates of the markers in the reference and deformed positions. These points are manually matched from the set of before and after images through the use of a facilitating Labview program that identifies and isolates detected markers from the background of the tissue. These coordinates are processed further by a Matlab script (see Appendix B.) Post-processing of these images was necessary because of the number of markers sought as well as the variations in image quality that accompanied variations in specimens. Unfortunately, automation was impossible for matching markers between the reference and deformed images because of the complexity and unpredictable nature of the marker patterns. Otherwise, identification of the markers was accomplished by the program using some of the same subroutines used to identify the markers for the moment-curvature analysis.

The displacement field is determined from the reference points, X_i, and the deformed points, x_i, according to equations 8.

$$\begin{aligned} u &= X_1 - x_1 \\ v &= X_2 - x_2 \end{aligned} \tag{8}$$

The u and v displacements each describe a surface when plotted as a function of the reference positions, X_1 and X_2. The X_1 axis is defined to coincide with the Cartesian x-axis and the X_2 axis is defined to coincide with the Cartesian y-axis. On the tissue, the X_1 is found to run along the length of the tissue and the X_2 axis is found to run along the thickness of the tissue as seen in figure XX. The surface fitted through the u and v displacements took the form of equations XX.

$$\begin{aligned} u &= a_0 + a_1X_1 + a_2X_2 + a_3X_1X_2 + a_4X_1^2 + a_5X_2^2 \\ v &= b_0 + b_1X_1 + b_2X_2 + b_3X_1X_2 + b_4X_1^2 + b_5X_2^2 \end{aligned} \tag{9}$$

For every marker processed, a u and v displacement was calculated and a set of fit parameters were fit for each. Higher and lower order equations were used with lesser success because of the propensity of those equations to be either hyposensitive or hypersensitive to perturbations in the surface. By fitting an equation of moderate sensitivity, $r^2 \approx 0.9$, the general form of the surface is captured by the equations while local perturbations of the surface caused by inherent errors in image capture and processing are averaged out. A higher r^2 value would yield a rough surface passing through points above and below the smooth surface fit by the lower r^2 value resulting in local inaccuracies when differentiated. The chosen form of the fit equations also allows for their derivatives to be taken with respect to X_1 and X_2, allowing for the determination of the deformation gradient, **F**, for each marker coordinate according to the following relationship.

$$\mathbf{F} = \mathbf{H} + \mathbf{I} = \begin{bmatrix} \frac{\partial u_1}{\partial X_1} & \frac{\partial u_1}{\partial X_2} \\ \frac{\partial u_2}{\partial X_1} & \frac{\partial u_2}{\partial X_2} \end{bmatrix} + \begin{bmatrix} 1 & 0 \\ 0 & 1 \end{bmatrix} = \begin{bmatrix} \lambda_1 & \kappa_1 \\ \kappa_2 & \lambda_2 \end{bmatrix} \tag{10}$$

The deformation gradient can then be decomposed into its stretch and rotation tensors, **U** and **R**, respectively. The polar decomposition of the deformation tensor removes rigid body motion effects into the rotation tensor, leaving only the stretch deformation information in the stretch tensor. The rigid body rotation information in **R** was calculated to determine the degree of rotation experienced by the tissue during flexure. Higher levels of rigid body rotation were determined to be coincident with measurements taken away from the center of the tissue.

$$\mathbf{F} = \mathbf{R}\mathbf{U} \tag{11}$$

$$\mathbf{U}^2 = \mathbf{F}^T\mathbf{F} \tag{12}$$

$$\mathbf{R} = \mathbf{F}\mathbf{U}^{-1} \tag{13}$$

$$\Lambda_1 = \sqrt{U_{11}^2 + U_{12}^2} \tag{14}$$

$$\Lambda_2 = \sqrt{U_{22}^2 + U_{12}^2} \tag{15}$$

The **U** stretch tensor reveals the amount of deformation in the X_1 and X_2 directions, respectively, via its U_{11} and U_{22} components. When no deformation occurs, the stretch tensor is identical to the identity tensor. When the U_{11} or U_{22} components are greater than one, than stretch in those directions occur. When either component is below unity than a contraction has occurred in that direction. Strains in the X_1 direction coincide with a change in the length of the tissue, either a contraction or an extension. Strains in the X_2 direction coincide with a change in the thickness of the tissue (Fig. XX). The Λ_1 and Λ_2 quantities were determined from U_{11}, U_{22}, and U_{12} so that the stretch information in U_{11} and U_{22} could be combined with the shearing information in U_{12} to provide a more accurate portrayal of the tissues behavior. The distribution of these quantities throughout the tissue can be related directly to classical bending theory in interpreting the behavior of the tissue during the experiment.

2.5 BIAXIAL MECHANICAL TESTING

2.5.1 Theoretical basis

Conventional means of testing materials exploit their isotropic nature and test them uniaxially. Biological materials are inherently anisotropic and so new testing methods have been developed such as biaxial testing. Biaxial testing has been used extensively in the literature [30, 31] to test soft tissues. The dimensions of the test specimens length-wise and width-wise are much greater than the thickness of the specimen. The specimens are mounted like a trampoline using several metal hooks as point attachments to the tissue. The center region of the tissue is where all the strain measurements are taken optically to avoid the confounding effects of the point loads on the edges.

The positions of the markers are captured by the testing software so that they may be used for the determination of the deformation gradient and subsequent quantities. Four markers are tracked on the tissue with each marker being located at each of the four vertices of a square. The reference positions of the markers are referred to as **X** while the deformed locations of the markers are referred to as **x**. The actual locations of the markers, however, do not always fall where they should for a perfect square. Thus, the (x, y) locations of the markers are mapped to a finite element coordinate system (r, s) using the following interpolation functions:

$$\mathbf{u}(r,s)=\sum_{n=1}^{m} f_n(r,s)\,\mathbf{u}_n \tag{16}$$

Here, **u** is defined as the displacements calculated from the reference and deformed marker positions, **u**=**x**-**X**. The shape functions, *f_n*, are used to relate the marker positions to their corresponding nodes in the finite element, namely marker positions in the (x, y) coordinate system are transformed to the location in the (r, s) coordinate system. Thus, the **u** displacements are found in the (r, s) coordinate system from the (x, y) positions and can then be used to determine the derivatives of **u** with respect to the (r, s) directions.

$$\frac{\partial \mathbf{u}}{\partial r}=\sum_{n=1}^{m}\frac{\partial f_n}{\partial r}\mathbf{u}_n \qquad \frac{\partial \mathbf{u}}{\partial s}=\sum_{n=1}^{m}\frac{\partial f_n}{\partial s}\mathbf{u}_n \tag{17}$$

The derivatives of **u** in the (r, s) system are then translated back into the (x, y) system using the following relationship:

$$\begin{bmatrix}\frac{\partial}{\partial r}\\ \frac{\partial}{\partial s}\end{bmatrix}=\begin{bmatrix}\frac{\partial u_1}{\partial r} & \frac{\partial u_2}{\partial r}\\ \frac{\partial u_1}{\partial s} & \frac{\partial u_2}{\partial s}\end{bmatrix}\begin{bmatrix}\frac{\partial}{\partial x_1}\\ \frac{\partial}{\partial x_2}\end{bmatrix} \tag{18}$$

The deformation gradient, **F**, then follows from the following relationship:

$$\mathbf{F}=\mathbf{H}+\mathbf{I}=\begin{bmatrix}\frac{\partial u_1}{\partial X_1} & \frac{\partial u_1}{\partial X_2}\\ \frac{\partial u_2}{\partial X_1} & \frac{\partial u_2}{\partial X_2}\end{bmatrix}+\begin{bmatrix}1 & 0\\ 0 & 1\end{bmatrix}=\begin{bmatrix}\lambda_1 & \kappa_1\\ \kappa_2 & \lambda_2\end{bmatrix} \tag{19}$$

With **F**, the right Cauchy-Green deformation tensor, **C**, can then be computed using equation 20. Through polar decomposition, **F** can be separated into two tensors, **R**, the rotation tensor, and **U**, the stretch tensor. The deformation gradient tensor includes information about the entire deformation, including rigid body rotation. By separating **F** into the rotation and stretch tensor, the rigid body rotation information is removed and only the stretch information remains. The right Cauchy-Green deformation tensor can also be obtained from the stretch tensor using equation 20.

$$\begin{aligned} \mathbf{C} &= \mathbf{F}^{\mathbf{T}}\mathbf{F} \\ \mathbf{C} &= \mathbf{U}^{\mathbf{2}} \end{aligned} \tag{20}$$

From the right Cauchy-Green deformation tensor, the Lagrangian strain tensor, **E**, can be obtained using the following:

$$\mathbf{E} = \frac{\mathbf{1}}{\mathbf{2}}(\mathbf{C} - \mathbf{I}) \tag{21}$$

The Lagrangian strain tensor is a commonly used method of quantifying strain. Lagrangian stress, **T**, can be determined from the dimensions of the specimen and the load applied to each of its sides.

$$T_{11} = \frac{P_1}{hL_2}, \quad T_{22} = \frac{P_2}{hL_1} \tag{22}$$

The load in each direction is P, the thickness of the specimen is h, and the length along each side of the specimen is taken to be L. Thickness measurements of soft tissues are notoriously difficult to take because of their deformability when subjected to conventional measurement techniques. Thus, in lieu of conventional stress measurements where load is normalized by cross-sectional area, the stress measured for these biaxial tests is membrane stress where the load is normalized by only the length of the tissue it is measured along. Instead of units of N/m^2, membrane stress is measured in units of N/m. For ease in modeling the soft tissue response, the Lagrangian stress is converted to the second Piola-Kirchhoff stress tensor, **S**.

$$\mathbf{S} = \mathbf{T}\cdot\mathbf{F}^{-1} \tag{23}$$

The maximum stretches in the longitudinal and circumferential directions for all stretch ratio protocols were normalized against the equibiaxial protocol to determine the percent change in maximum stretches. As the biaxial load was changed from equibiaxial (T_{CC}:T_{RR}=1:1) to non-equibiaxial conditions (e.g. T_C:T_R=1:0.17), the degree of axial mechanical coupling was assessed from the percent change in peak stretch ratio along each axis. These values were then used to create axial coupling plots and the results between the aortic and pulmonary leaflets were compared [64]. For example, as tension was reduced along the radial axis, (with circumferential tension unchanged), we measured the contraction in the radial direction and the corresponding stretch in the circumferential direction. Thus, axial-coupling was determined as the percent change in circumferential or radial stretch from the equibiaxial state to the non-equibiaxial state: $((U_{xx}-U_{eq})/U_{eq})*100\%$. These axial coupling plots illustrate some of the subtle structural relationships inherent in the tissue that binds the behavior of the two primary directions of the tissue together. If coupling were to absent in the specimen being tested, the response in either the circumferential or radial directions would be wholly independent of the other. Because of the intricate structure of the leaflet and the organization of collagen fibers along the circumferential direction, the leaflet is very responsive to coupling. With radially applied tension the fibers in the leaflet separate and rotate away from the circumferential axis towards the radial axis. This resulted in extension in the radial direction and contraction in the circumferential direction. By varying the tension ratios along the circumferential and radial directions, an idea of the magnitude of axial-coupling can be determined. Membrane tension versus stretch plots were generated for the circumferential and radial directions using T_{ij} and U_{ij}, respectively to determine the response of the tissue with increasing load. Comparisons can be made between the two tissues and their axial coupling plots to determine the magnitude of coupling between the two directions. Significant differences in axial coupling would be related to some significant difference between the structures and organization of collagen fibers between the two leaflets.

2.5.2 Device description

The biaxial testing device consists of four computer controlled stepper motors arranged around a specimen bath (Fig. 31). The bath consists of one cross shaped container recessed within another. The exterior cross-shaped bath is used to circulate a separate solution to control the temperature of the solution within the inner cross for temperature dependent testing. One stepper motor is attached to every arm of the cross. Above the center of the cross is positioned a camera attached to a video capture card in the computer. The movement of the stepper motors is controlled by the four markers tracked from the images of the specimen captured by the camera.

Attached to every stepper motor is a carriage that suspends a pair of pulleys over the edge of the specimen bath. The pulleys are oriented so that sutures which have been hooked into the edges of the tissue specimen can be looped over the pulley. The suture lines are inelastic and of equal length so the tissue specimen can be oriented properly at the center of the cross.

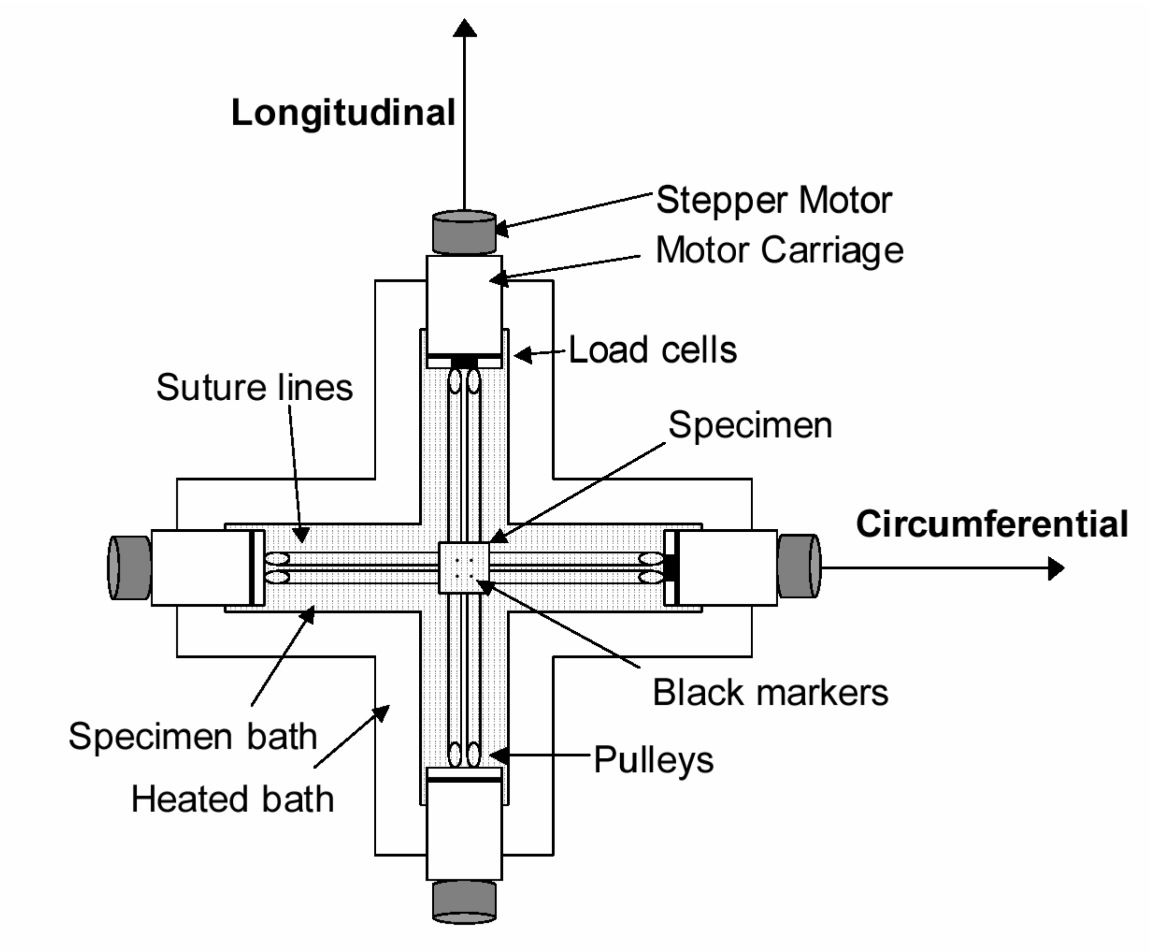

Figure 31, Schematic of biaxial testing device. The specimen has four black markers that are tracked by a camera system suspended over the device (outwards from the page). The specimen is held in place by hooks and suture lines which are attached to pulleys which translate the forces exerted on the sutures to the load cells. The stepper motors activate in unison to increase or decrease tension upon the circumferential and longitudinal axes.

2.5.3 Testing methods

Biaxial experiments were performed following protocols and methods previously established [30]. Briefly, tissue specimens were cut from the cusps of native porcine aortic and pulmonary valve leaflets to be squares as closely as possible. On average, the aortic samples measured 10.1 mm in width and 9 mm in length using a slide caliper. Pulmonary samples measured 10 mm in width and 9 mm in length. A very small graphite marker was glued to the upper right of the square specimens so that the circumferential and radial directions could be retained and so the two different sides of the specimen could be differentiated. Thickness measurements were performed using a rotating thickness caliper at the four corners of the specimen and averaged to yield an average thickness of 0.522 mm for aortic leaflets and 0.254 mm for pulmonary leaflets. Four small graphite markers making a square were glued using a minimal amount of cyanoacrylate to the center of the specimen below the nodulus of Arantii. The tissue specimen was then placed into the biaxial device so that the positions of the markers could be determined before sutures were placed into the tissue. This state was designated as the free-floating reference state. Suture lines with hooks on either end were then attached to the tissue specimen. Two suture lines were attached to every side of the specimen. The marker positions were captured again and designated as the free-floating sutured state. The geometry of the tissue specimen and the placement of the markers and the hooks and lines can be seen in figure 32. The suture lines were then fitted over the pairs of pulleys attached to the stepper motor carriages. A load of approximately 0.5 g was then applied to both axes of the specimen. Another set of marker positions were then taken and designated as the sutured pre-tensioned state.

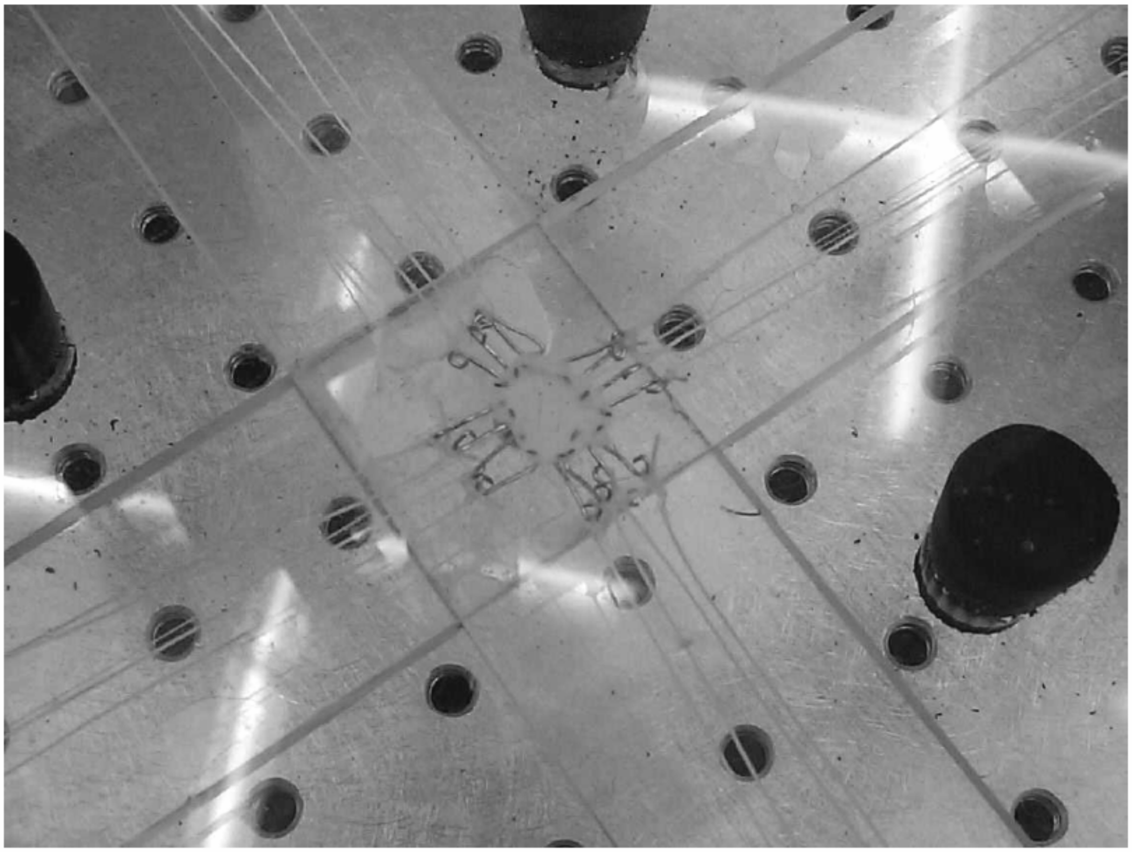

Figure 32, Photograph of a specimen attached to hooks and suture lines and suspended within the testing bath.

The first test protocol performed was a load controlled equi-biaxial stretch. Aortic valve tissues were loaded to 60 Nm^{-1} and pulmonary valve tissues were loaded to 30 Nm^{-1}. The ratio of the tensions upon each side of the tissue was kept 1:1. Marker positions were recorded after this first test run to obtain the post-preconditioned, pre-tensioned state. This state was used as the reference state for the following analyses. Six other protocols were performed upon the test specimen before a final equi-biaxial test was performed. The protocols that were performed possessed the following tension ratios of 0.5:1, 1:0.5, 0.25:1, 1:0.25, 0.1:1, 1:0.1 (Fig 33). The variation of tensions between the longitudinal and circumferential directions reveals what mechanical differences the tissue may possess between the axes along with any coupling that may occur.

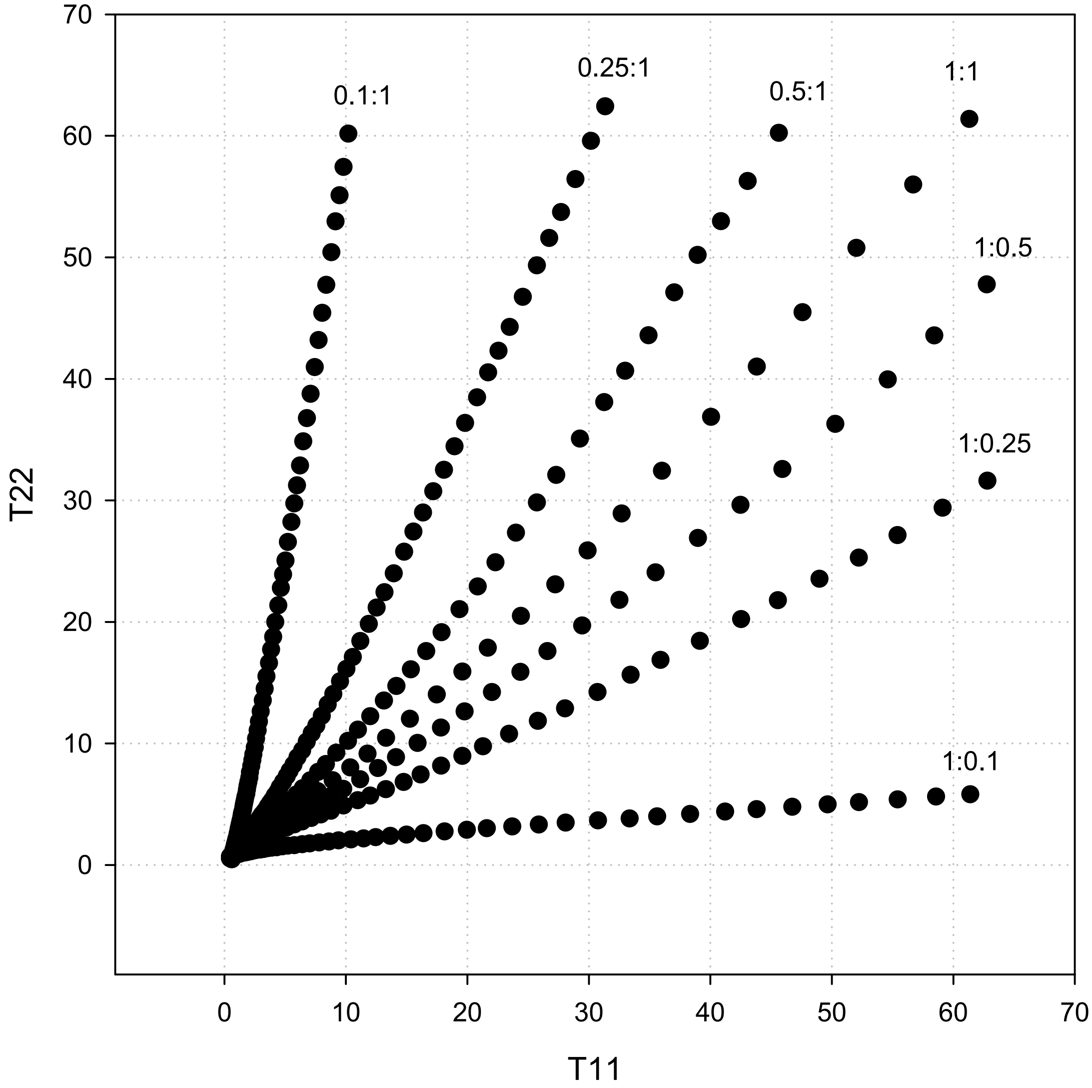

Figure 33, Representative plot of the tensions in the longitudinal and circumferential directions for the different ratios used (1:1, 0.5:1, 1:0.5, 0.25:1, 1:0.25, 0.1:1, 1:0.1) for aortic valve.

3.0 RESULTS

3.1 FLEXURE RESULTS

A total of 18 aortic and 18 pulmonary leaflet specimens were tested. The differences in bending stiffnesses between the aortic and pulmonary valve are illustrated in the plot in figure 34. Figure 35 shows the typical results obtained from a bending test, showing the data points and fitted trend lines obtained in the AC and WC directions for one tissue sample. A linear trend line was fitted to the data points to determine the slope and EI. Results from the tests performed are summarized in figures 36 and 37. The effective stiffness of the tissue, E, is obtained from the EI flexural rigidity values by dividing by I, the second moment of the area determined by the tissue geometry. The value of I, determined from equation 2, is highly dependent upon the measured thickness of the sample because of the $1/t^3$ term. As mentioned above, the protocol for determining the thickness of the tissue specimen involved taking the initial caliper reading and the caliper reading three seconds later. This method of measurement sought to normalize for the compressibility of the tissue under loads. However, because of the nature of the tissue, thickness measurements and quantities dependent upon them must be considered with some caution.

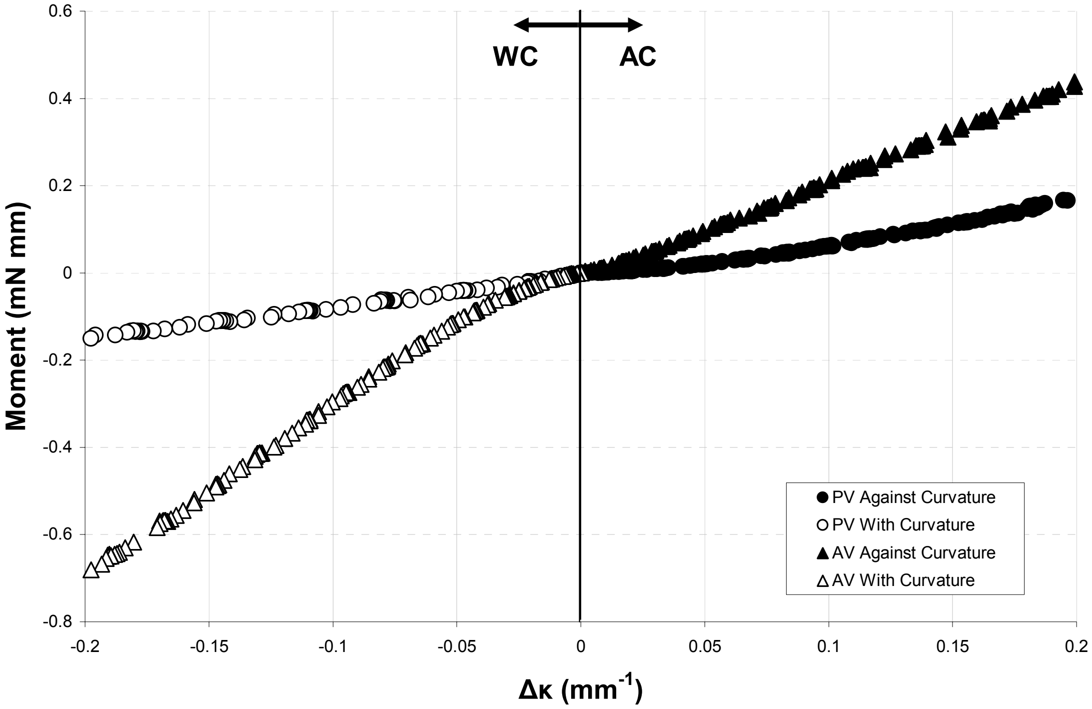

Figure 34, A representative plot of the moment-curvature bending response of a native aortic valve leaflet in the AC and WC directions that has been flexed to a change of curvature of 0.2 in either direction.

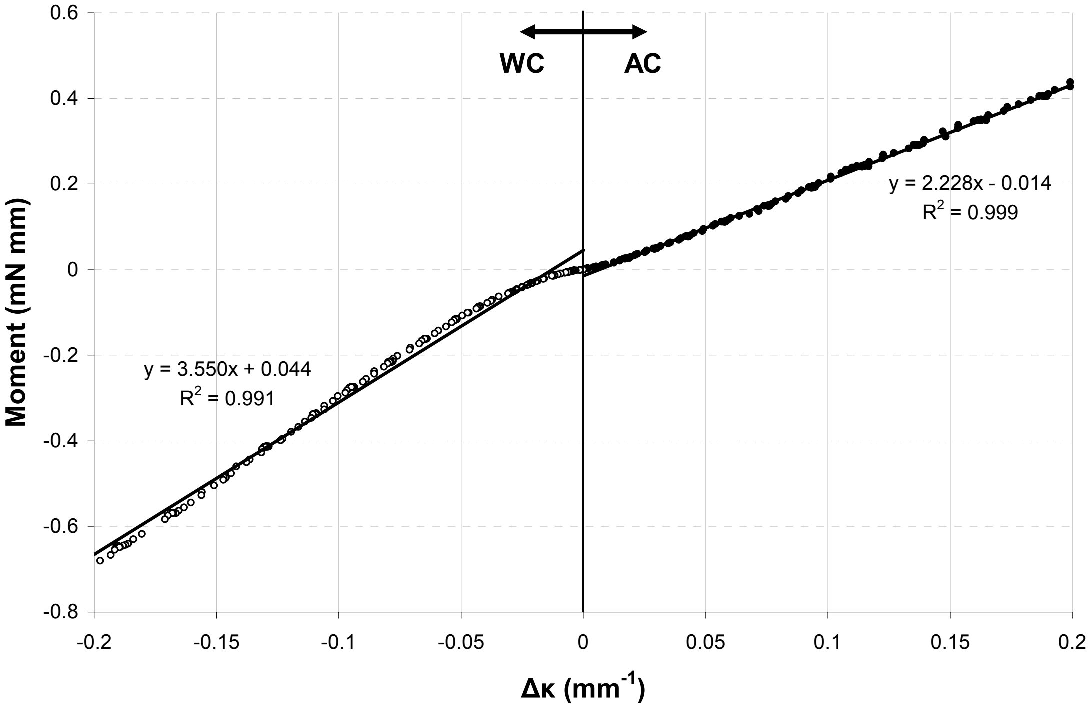

Figure 35, Representative plot of moment-curvature relationship for aortic valve showing fitted linear trend line. The slope of the trend line represents the quantity EI. Notice the greater degree of linearity in the AC direction in contrast to the delayed onset of linearity in the WC direction.

The averaged flexural rigidity (EI) for aortic and pulmonary valve leaflets are summarized by figure 36. The averaged effective modulus (E) for aortic and pulmonary valve leaflets are summarized by figure 37. Error bars represent the standard error of the mean for each set of 18 tests.

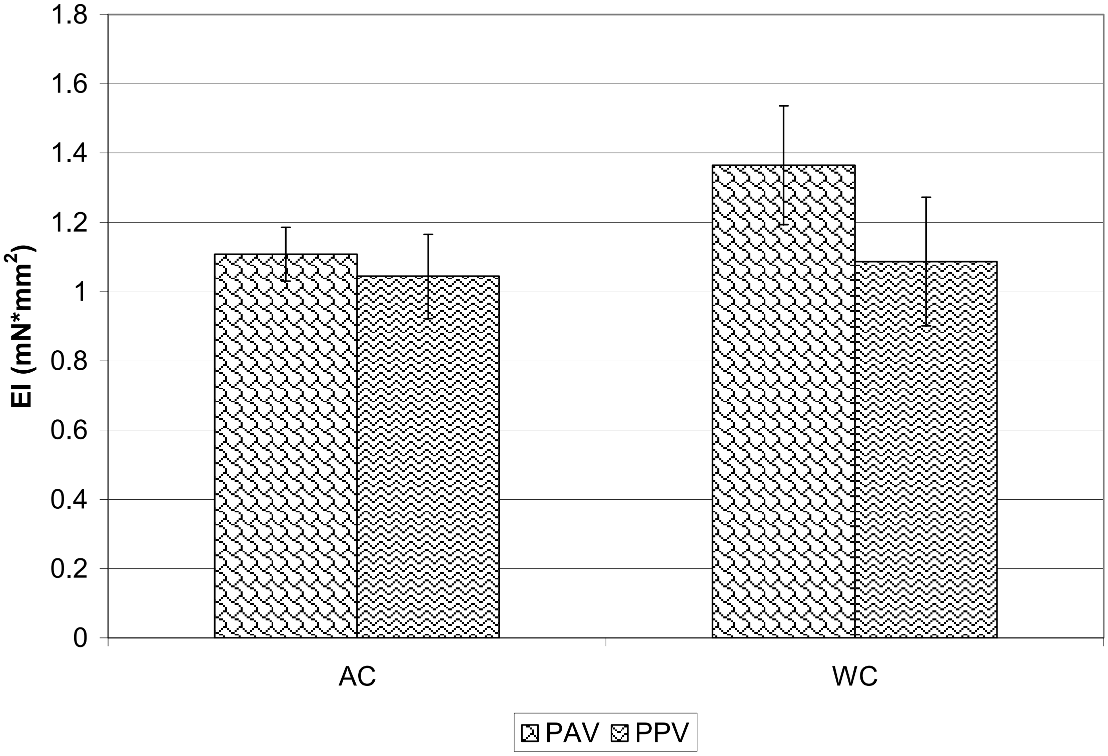

Figure 36, The flexural rigidity was determined from the slope of moment-curvature plots and is a product of the effective modulus, E_{eff}, and the second moment of the area, I. Error bars are SEM. There were no statistically significant differences between the AC and WC values for the PAV and PPV.

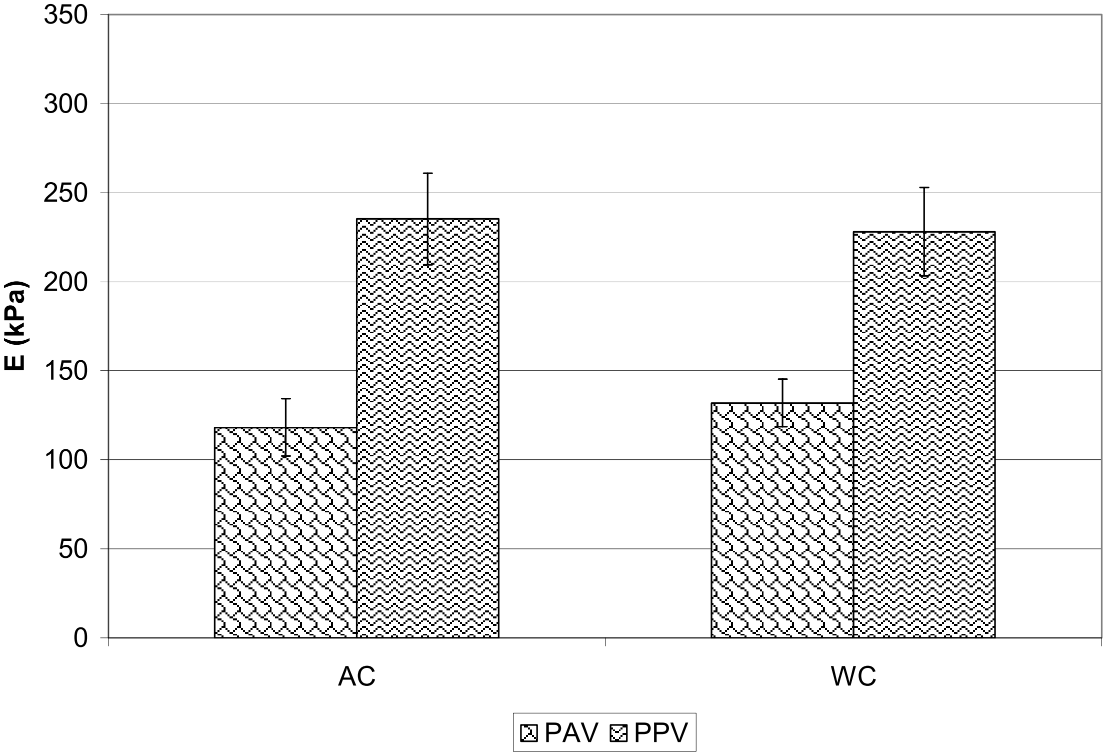

Figure 37, The effective modulus of the tissue was determined in the AC and WC directions for each tissue sample. The effective modulus was obtained from the slope of the moment-curvature plot after having divided out the second moment of the area (I.) Error bars are SEM. There was a statistically significant difference in the AC bending direction between the PAV and PPV (p=0.007) and in the WC bending direction (p=0.004). There were no statistically significant differences between the AC and WC bending directions for each valve type.

The bending response of the aortic tissue in the AC direction was relatively linear (Fig. 38) while the response in the WC direction was linear at slightly higher changes in curvature. On average, bending in the AC direction was determined to be negligibly different from bending in the WC direction (n=17). In the AC direction, the flexural rigidity was 1.06±0.08 (Fig. 39) with an effective stiffness of 150±16 kPa (Fig. 40). In the WC direction, the flexural rigidity was 1.08±0.17 with an effective stiffness of 144±13 kPa. Similar results were obtained for the pulmonary tissue where the flexural rigidity and effective stiffness in the AC direction were 1.04±0.12 and 235±26, respectively. In the WC direction the flexural rigidity was 1.09±0.19 and the effective stiffness was 228±25.

3.2 TRANSMURAL STRAIN RESULTS

Fourteen porcine aortic valve specimens and eleven porcine pulmonary valve specimens were tested and images captured for transmural analysis. Specimens were flexed in the AC and WC directions at three curvature increments. The curvature that was measured was the change in curvature from the tissues initial curvature. This was accomplished by the testing program by taking the curvature of the tissue before testing and using that as a baseline for all subsequent curvature measurements. Images were taken of the tissue at its reference state for everyone of the three curvature increments tested for. Tissue was flexed to a change in curvature of 0.1, 0.2, and 0.3. These values were chosen to encompass previously attained curvatures in flexure between 0-0.2 [65] as well as larger ranges of curvature in the 0.2-0.3 region suggested by the literature [66]. All of the tissue specimens reached a change in curvature of 0.1, only some to 0.2, and even fewer to a change of 0.3. For each level of curvature and each direction of bending, the location of the neutral axis was compared along with the maximum and minimum stretches in the X_1 and X_2 directions.

To characterize the overall layer behavior of the tissue, the location of the neutral plane was determined by examining Λ_1 against the thickness of the tissue (Figs. 39 & 48). Shearing within the leaflets was determined to be sufficiently negligible enough so that Λ_1 and Λ_2 were approximately equal to U_{11} and U_{22}. The values and locations of the maximum and minimum Λ_1 stretches were determined and compared between the WC and AC directions to find the relative deformability of the layers in compression and tension. A composite plot of Λ_1 versus normalized thickness was generated by averaging the Λ_1 values at every 0.1 increment of normalized thickness for all specimens (Figs. 41, 42 & 50, 51). Λ_1 and Λ_2 maximum and minimum values were determined at all three levels of curvature (Figs. 39, 40, 43 & 48, 49, 52) and a composite Λ_2 versus normalized thickness plot was also generated (Figs. 44, 45 & 51, 53). For appropriate pulmonary valve graphs, aortic valve results were also plotted to facilitate the illustration of differences between the two. Maximum and minimum values of the shear angle α were determined for the AC and WC directions and averaged (Fig. 46 & 55).

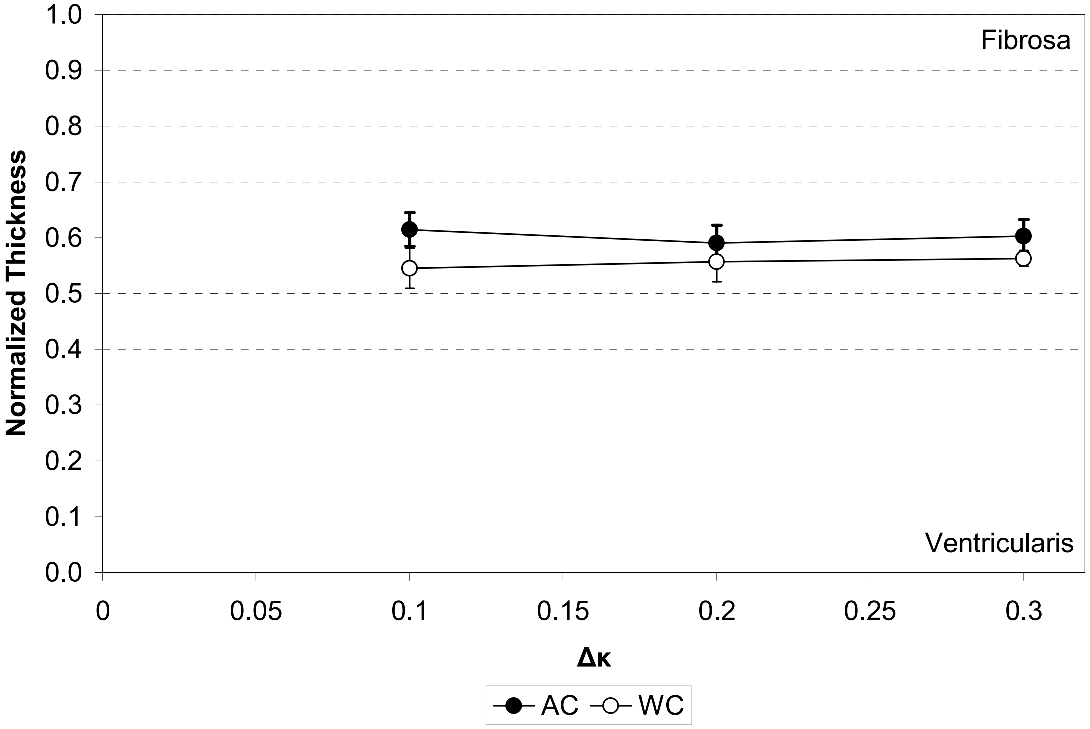

Figure 38, These results were obtained from transmural bending tests performed on native aortic valve tissue. The tissue was flexed to three different changes of curvature, 0.1, 0.2, and 0.3. The location of the neutral axis through the tissue was normalized against the thickness and tabulated with other results. Error bars are SEM.

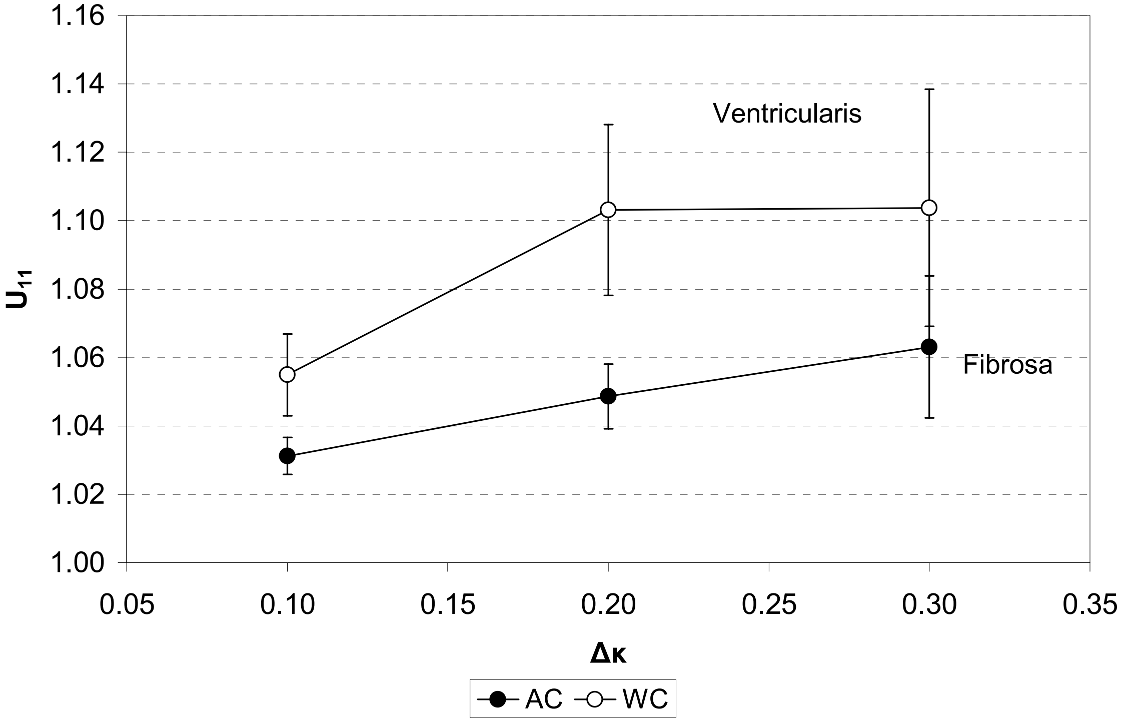

Figure 39, These results show the change in the aortic valve maximum stretch in the circumferential direction along the thickness of the tissue at three different levels of curvature. Error bars are SEM. There was a statistically significant difference between the AC and WC directions at 0.2 change in curvature (p=0.041).

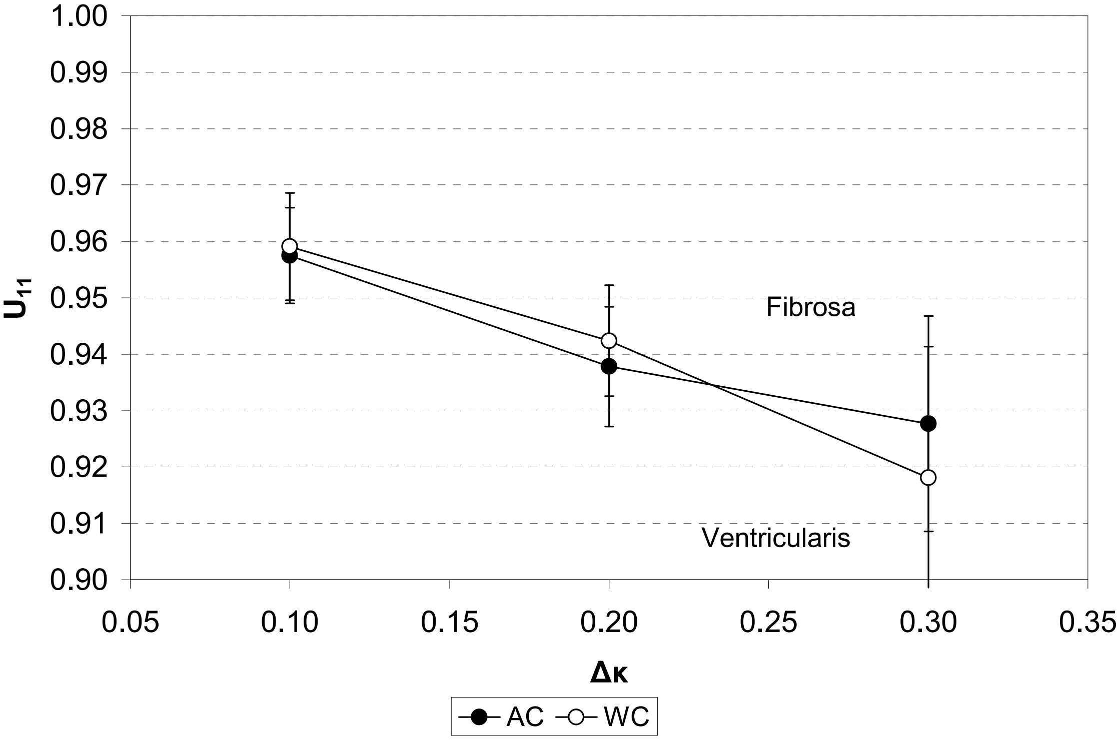

Figure 40, These results show the change in the minimum aortic valve U_{11} stretch in the circumferential direction along the thickness of the tissue at three different levels of curvature. Error bars are SEM. There were no statistically significant differences between the AC and WC bending directions.

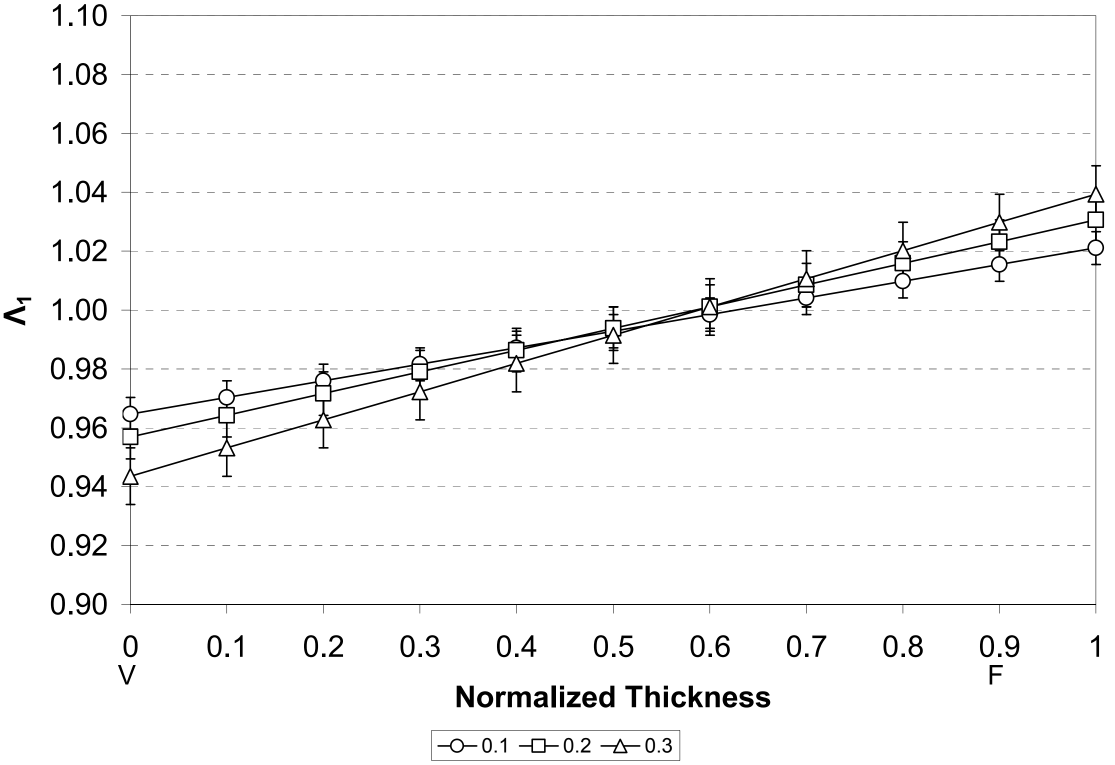

Figure 41, The regression lines from AC aortic valve samples at three curvatures were averaged together to create composite regressions lines representing the values of Λ_1 plotted against the normalized thickness of the tissue. Error bars are SEM. The differences in curvature were determined to not be statistically different from each other.

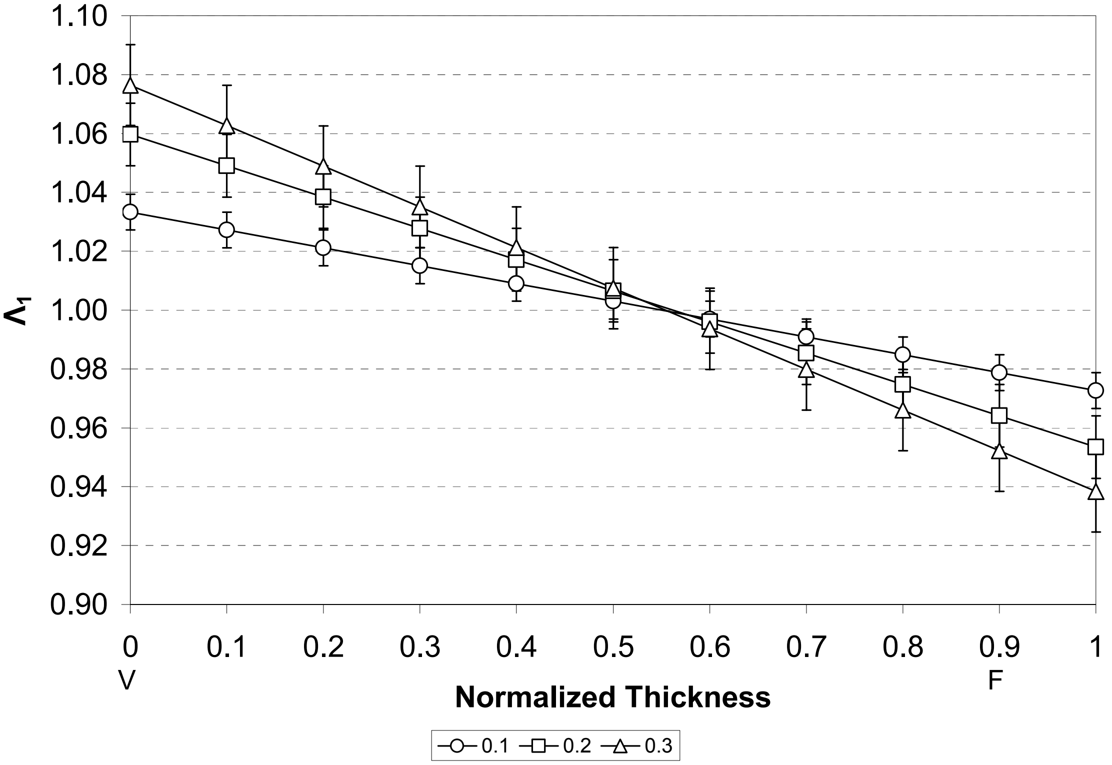

Figure 42, The regression lines from WC aortic valve samples at three curvatures were averaged together to create composite regressions lines representing the values of Λ_1 plotted against the normalized thickness of the tissue. Error bars are SEM. The differences in curvature were determined to not be statistically different from each other.

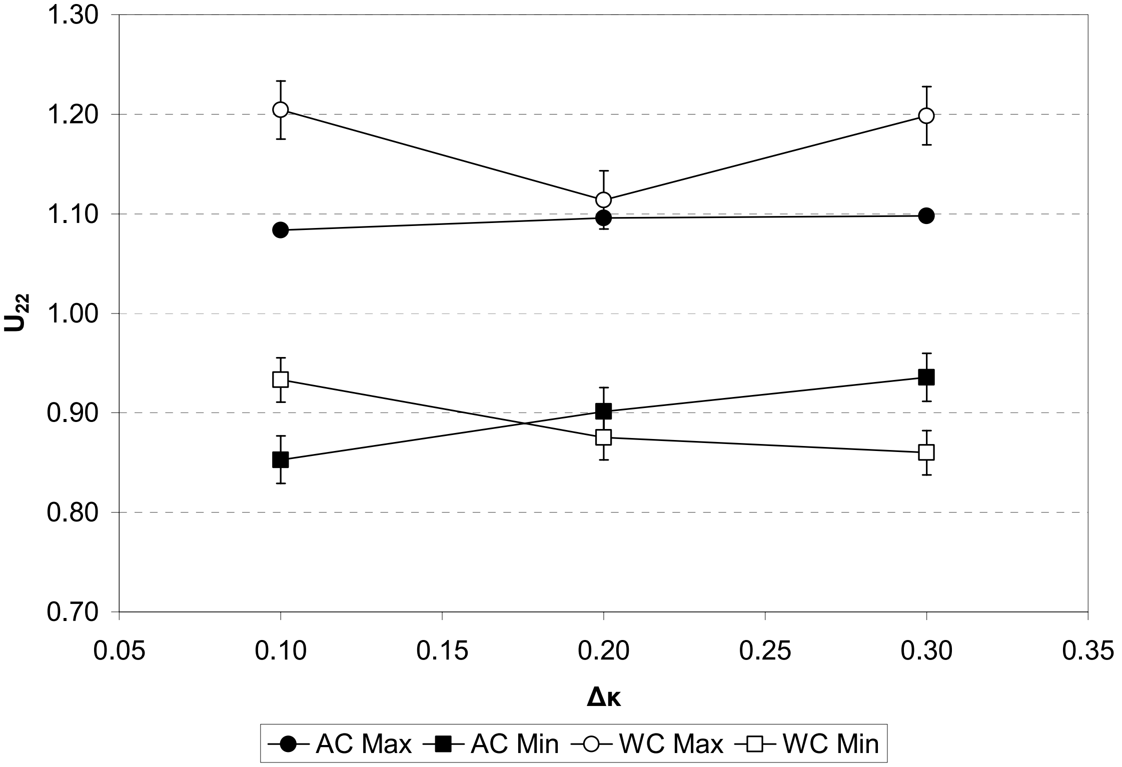

Figure 43, The maximum and minimum changes in aortic valve thickness, U_{22}, are plotted for AC and WC samples at three different levels of curvature. Error bars are presented as SEM. Differences between the AC and WC samples were determined to be not statistically significant.

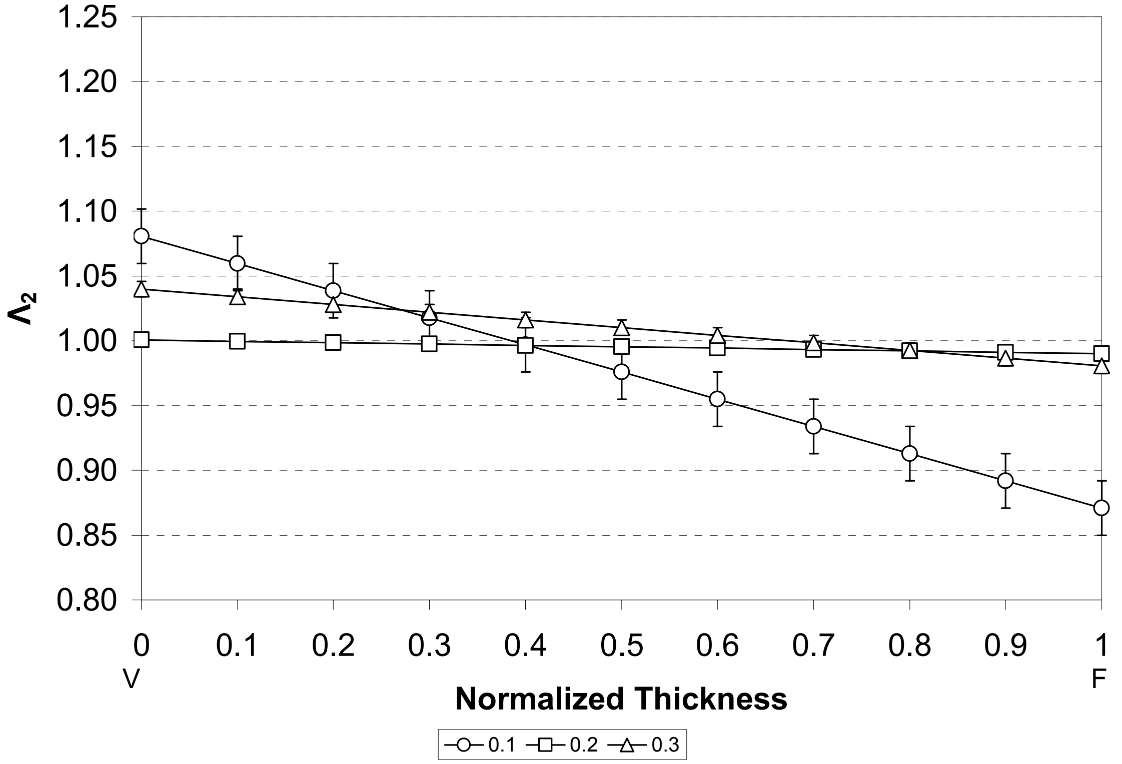

Figure 44, The regression lines from AC aortic valve samples at three curvatures were averaged together to create composite regressions lines representing the values of Λ_2 plotted against the normalized thickness of the tissue. Error bars are presented as SEM.

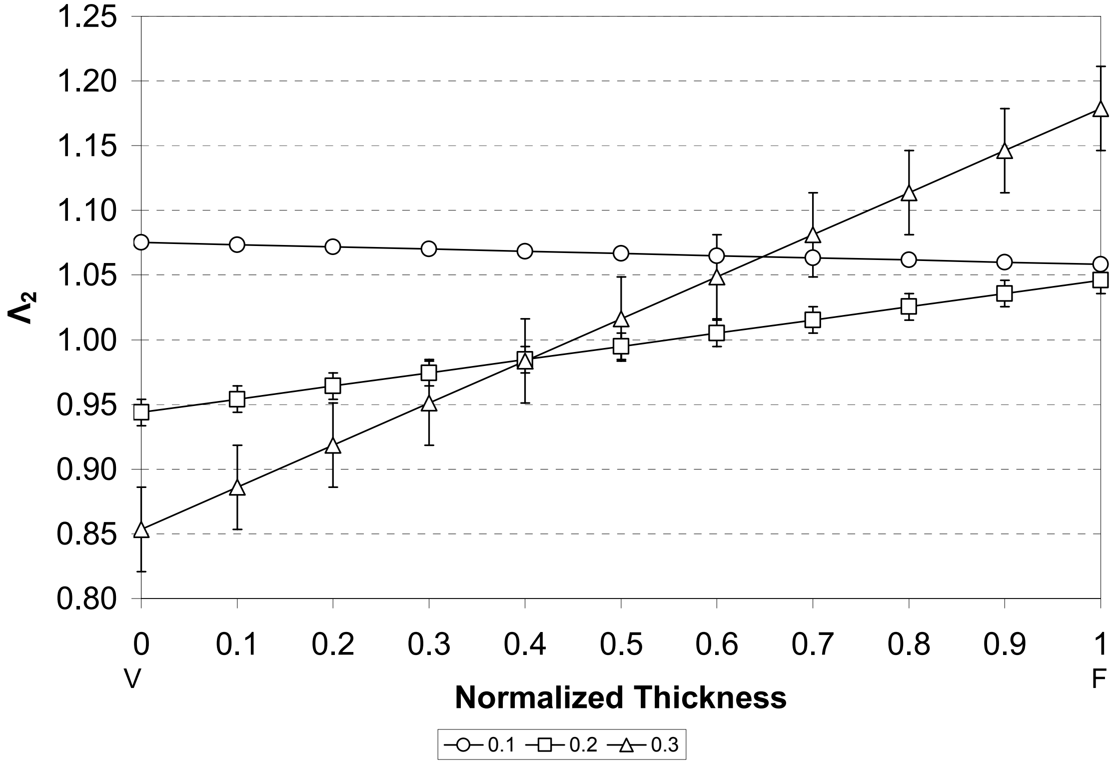

Figure 45, The regression lines from WC aortic valve samples at three curvatures were averaged together to create composite regressions lines representing the values of Λ_2 plotted against the normalized thickness of the tissue. Error bars are presented as SEM.

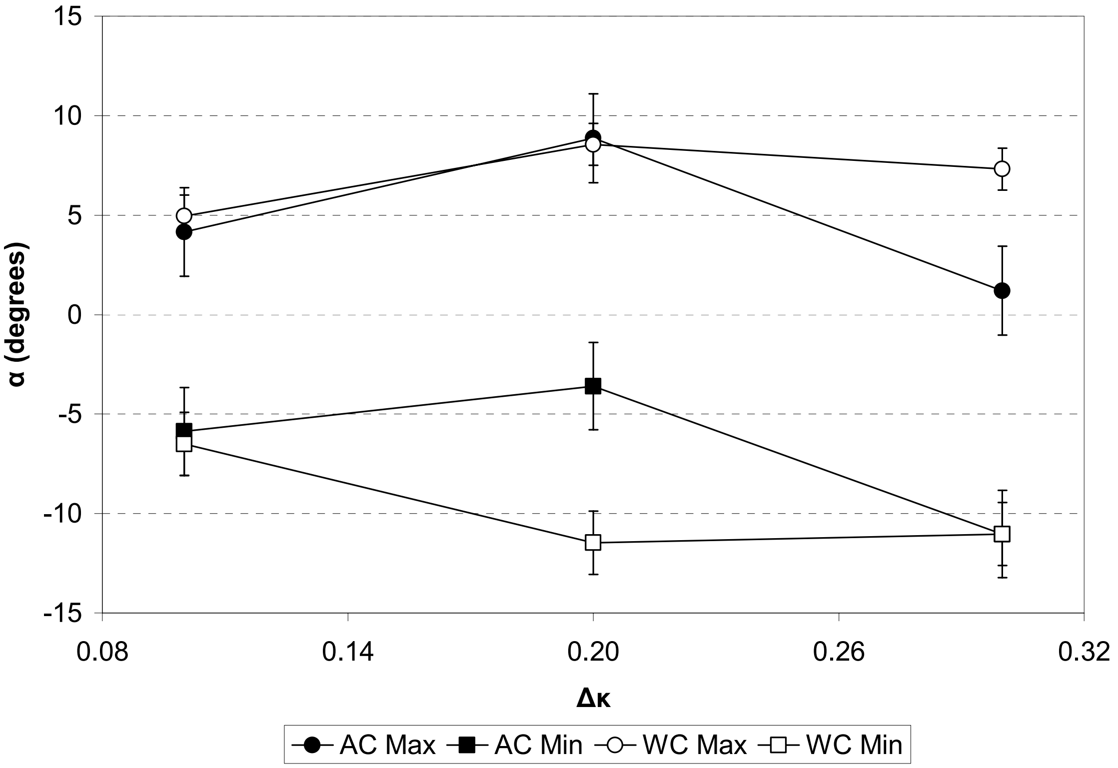

Figure 46, These results show the change in the aortic valve shear angle α along the thickness of the tissue at three different levels of curvature. Error bars are presented as SEM. There was a statistically significant difference ($p=0.033$) between the minimum AC α value and the minimum WC α value.

Table 2 - Neutral Axis Location values at three different levels of curvature showing the progression of the neutral axis towards the fibrosa in the aortic valve. Neutral axis values are presented as normalized thickness with the ventricularis at 0 and the fibrosa at 1. Error is reported as SEM. There were no statistically significant differences.

		Against Curvature (AC)	With Curvature (WC)
Δκ	**0.1**	0.61±0.09	0.55±0.10
	0.2	0.59±0.10	0.56±0.10
	0.3	0.60±0.07	0.56±0.03

Table 3 - Tabulated aortic valve U11 values showing maximum and minimum U11 values at three different levels of curvature for AC and WC directions. Tensile and compressive strains increase with increasing flexure in both bending directions. Error is reported as SEM. There were no statistically significant differences.

		Against Curvature (AC)		With Curvature (WC)	
		Maximum	Minimum	Maximum	Minimum
Δκ	**0.1**	1.03±0.02	0.96±0.02	1.05±0.03	0.96±0.03
	0.2	1.05±0.03	0.94±0.03	1.10±0.07	0.94±0.03
	0.3	1.06±0.05	0.93±0.05	1.10±0.08	0.92±0.05

Table 4 – Aortic valve U22 values at three levels of curvature showing an increase in the maximum U_{22} in the AC direction with increasing flexure and a decrease in the minimum U_{22} in the WC direction with increasing flexure. Error is reported as SEM. There were no statistically significant differences.

		Against Curvature (AC)		With Curvature (WC)	
		Maximum	Minimum	Maximum	Minimum
Δκ	**0.1**	1.08±0.09	0.85±0.13	1.20±0.15	0.93±0.14
	0.2	1.10±0.08	0.90±0.08	1.11±0.16	0.88±0.08
	0.3	1.10±0.03	0.94±0.03	1.20±0.13	0.86±0.17

Table 5 – Aortic valve shear angle α values in degrees at three levels of curvature measured in degrees showing a gradual increase in the shear angle with increasing flexure. Error is reported as SEM. There was a statistically significant difference (p=0.033) between the minimum AC α value and the minimum WC α value.

		Against Curvature (AC)		With Curvature (WC)	
		Maximum	Minimum	Maximum	Minimum
Δκ	**0.1**	4.15±5.72	-5.87±7.85	4.96±3.08	-6.50±9.61
	0.2	8.87±8.94	-3.60±4.82	8.55±4.64	-11.47±9.24
	0.3	1.20±1.77	-4.25±2.20	7.32±5.28	-11.03±13.90

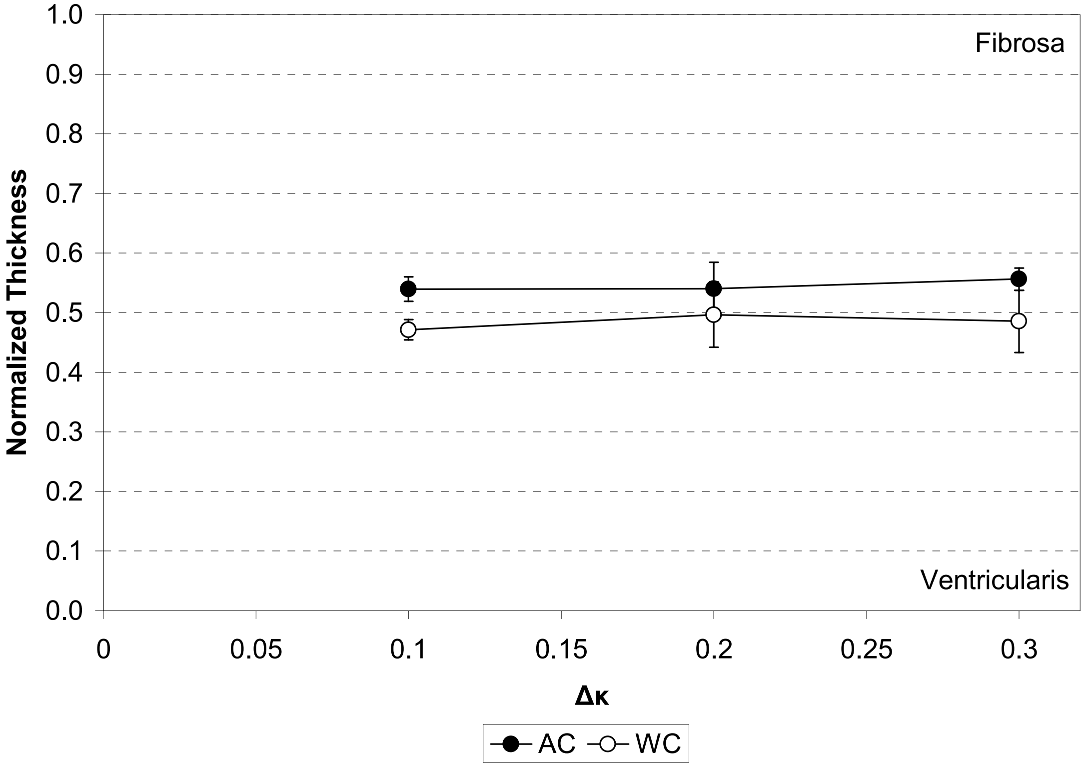

Figure 47, These results were obtained from transmural bending tests performed on native pulmonary valve tissue. The tissue was flexed to three different changes of curvature, 0.1, 0.2, and 0.3. The location of the neutral axis through the tissue was normalized against the thickness and tabulated with other results. Error bars are SEM. There was a statistically significant difference (p=0.030) between the bending directions at 0.1 change in curvature.

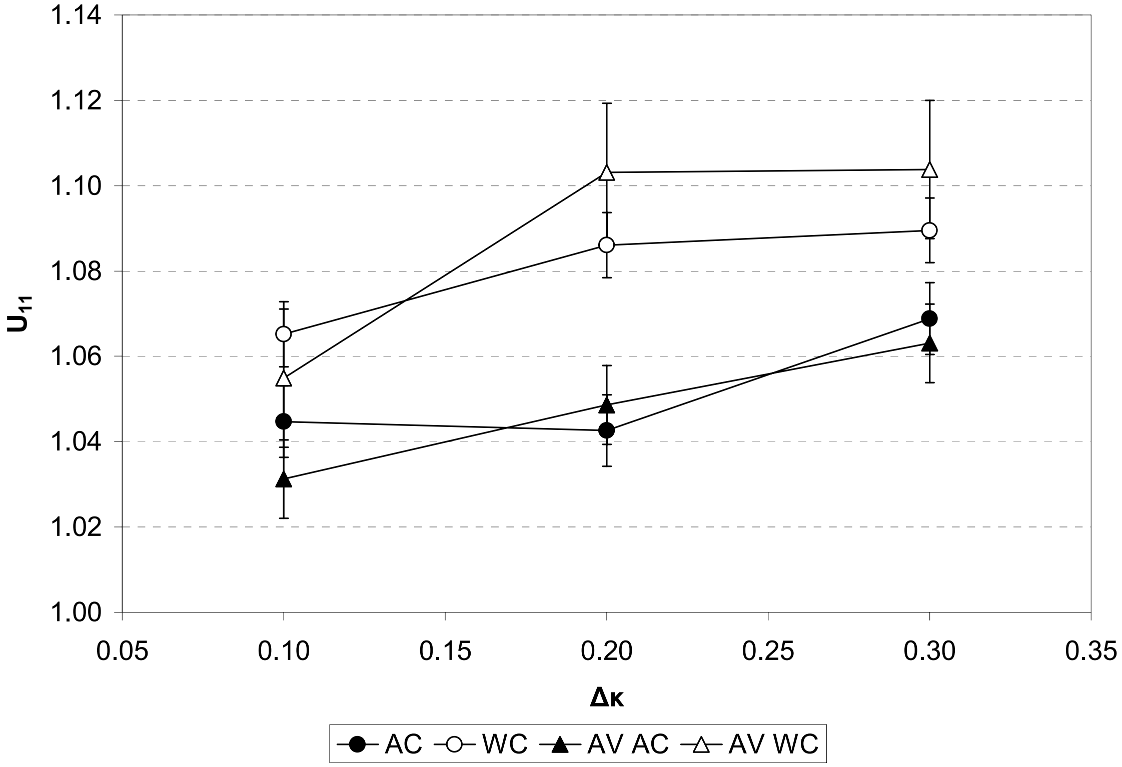

Figure 48, These results show the change in the maximum pulmonary valve stretch in the circumferential direction along the thickness of the tissue at three different levels of curvature. Error bars are SEM. There were no statistically significant differences.

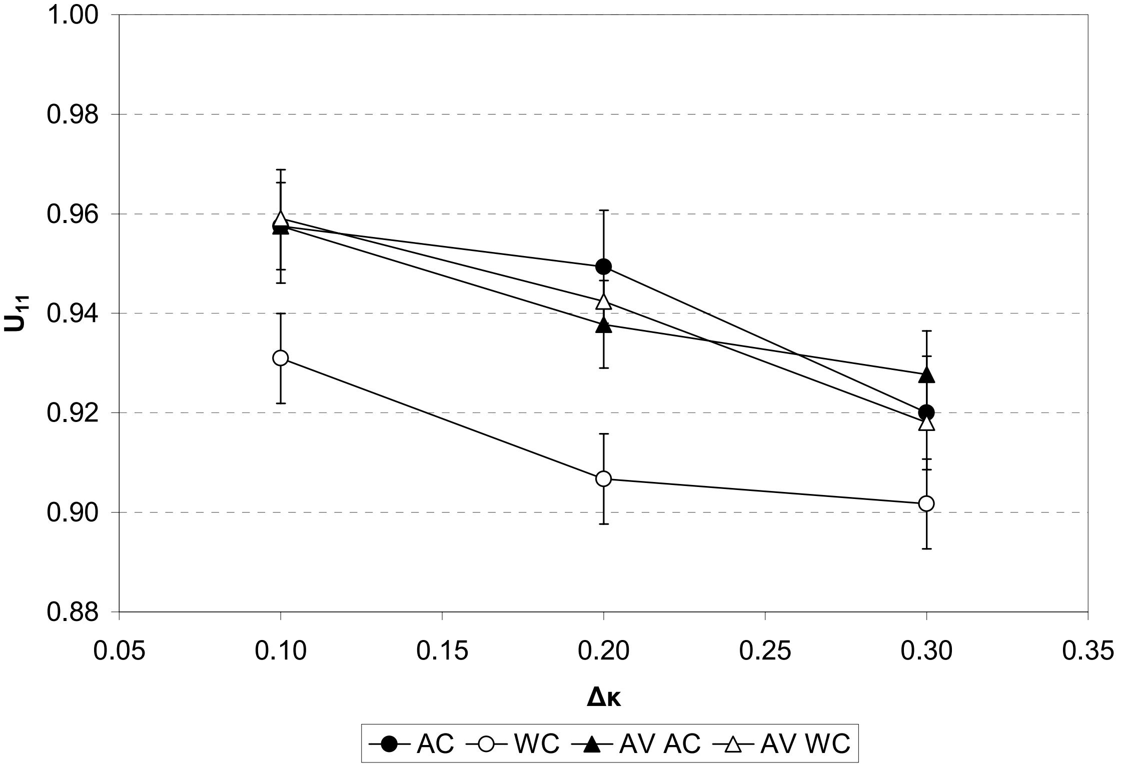

Figure 49, These results show the change in the minimum pulmonary valve U_{11} stretch in the circumferential direction along the thickness of the tissue at three different levels of curvature. Error bars are SEM. There were no statistically significant differences.

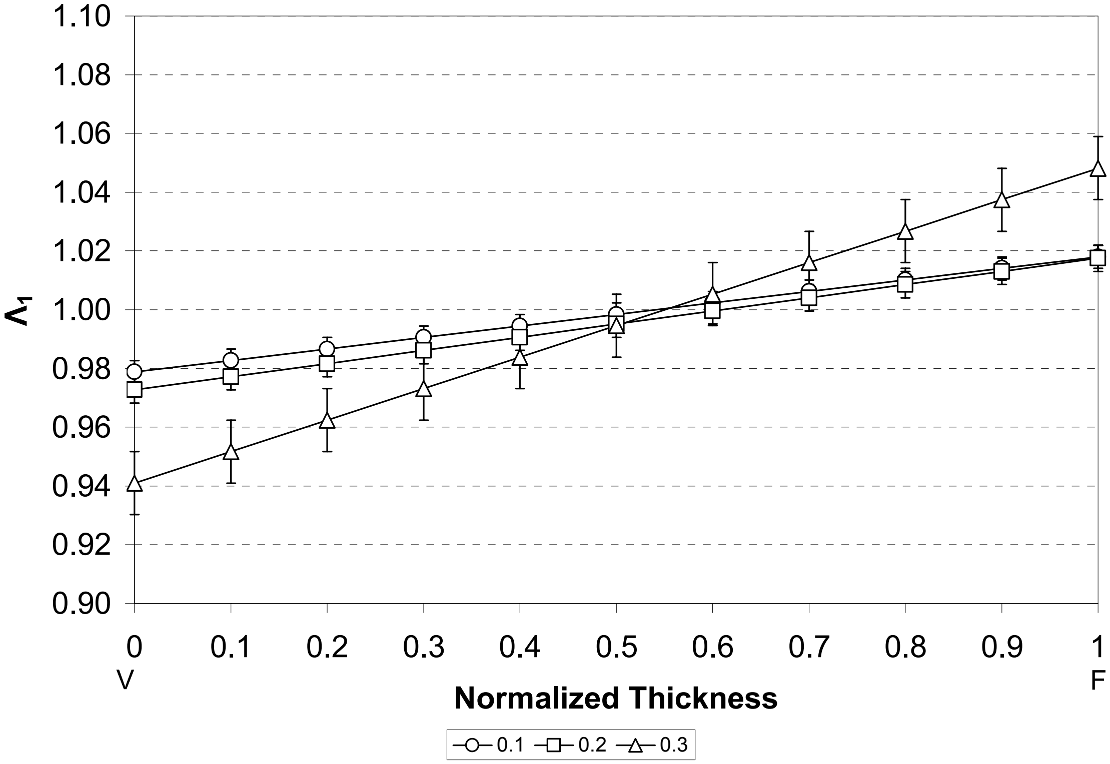

Figure 50, The regression lines from AC pulmonary valve samples at three curvatures were averaged together to create composite regressions lines representing the values of Λ_1 plotted against the normalized thickness of the tissue. Error bars are SEM.

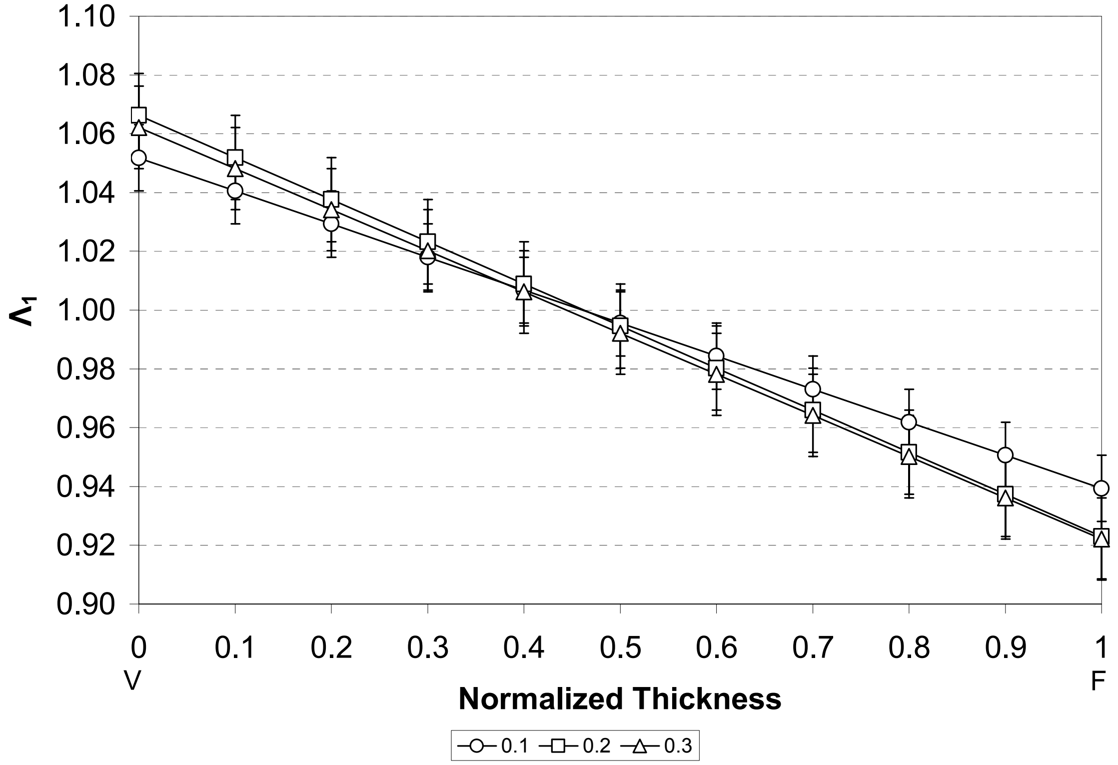

Figure 51, The regression lines from WC pulmonary valve samples at three curvatures were averaged together to create composite regressions lines representing the values of Λ_1 plotted against the normalized thickness of the tissue. Error bars are SEM.

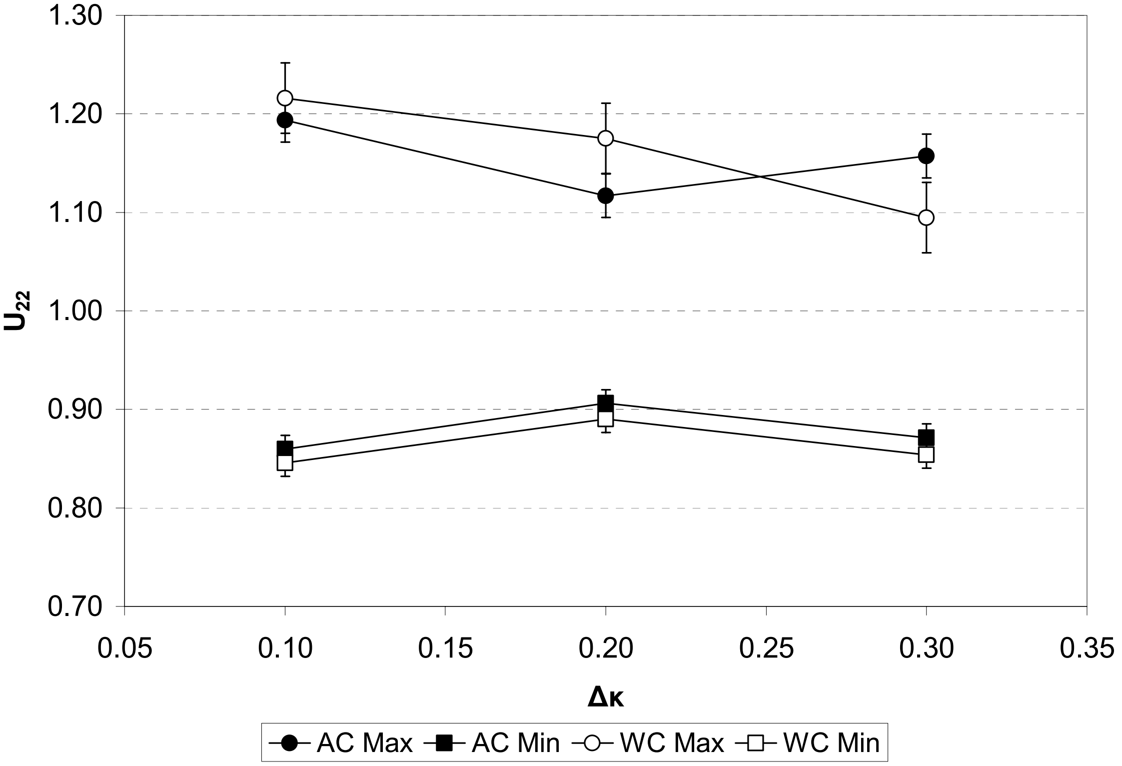

Figure 52, The maximum and minimum changes in pulmonary valve thickness, U_{22}, are plotted for AC and WC samples at three different levels of curvature. Error bars are SEM and no statistically significant differences were found between the maximum and minimum U_{22} values in the AC and WC directions.

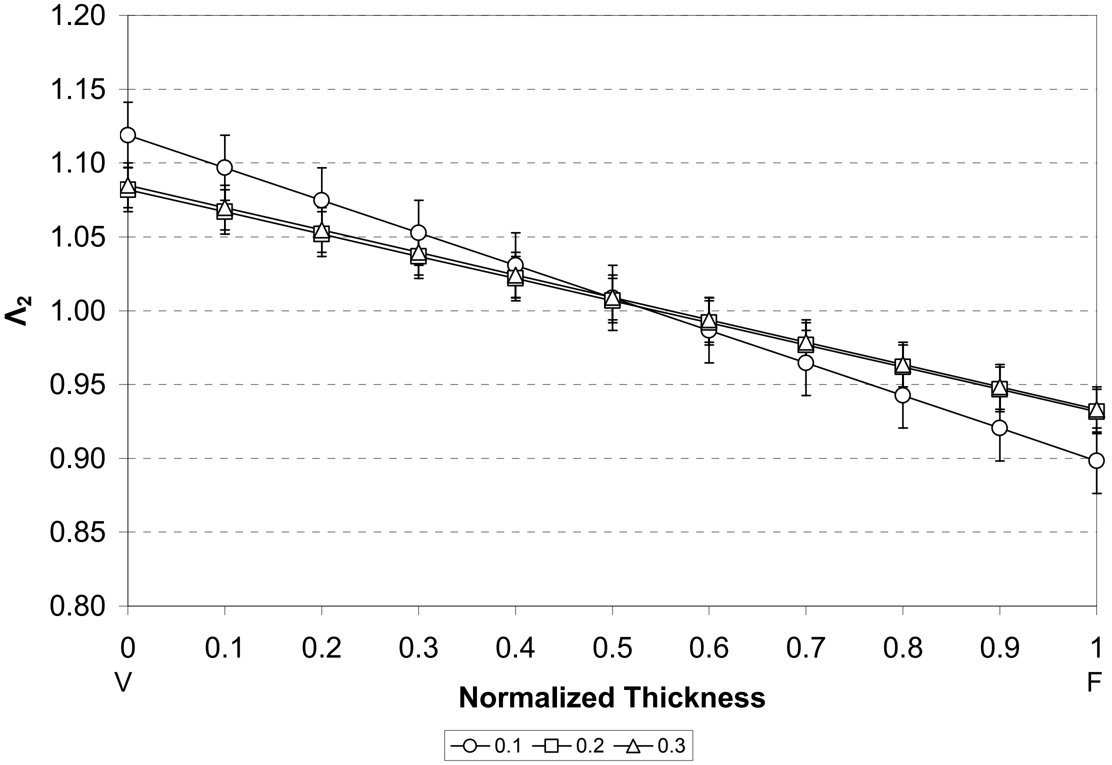

Figure 53, The regression lines from AC pulmonary valve samples at three curvatures were averaged together to create composite regressions lines representing the values of Λ_2 plotted against the normalized thickness of the tissue. Error bars are SEM.

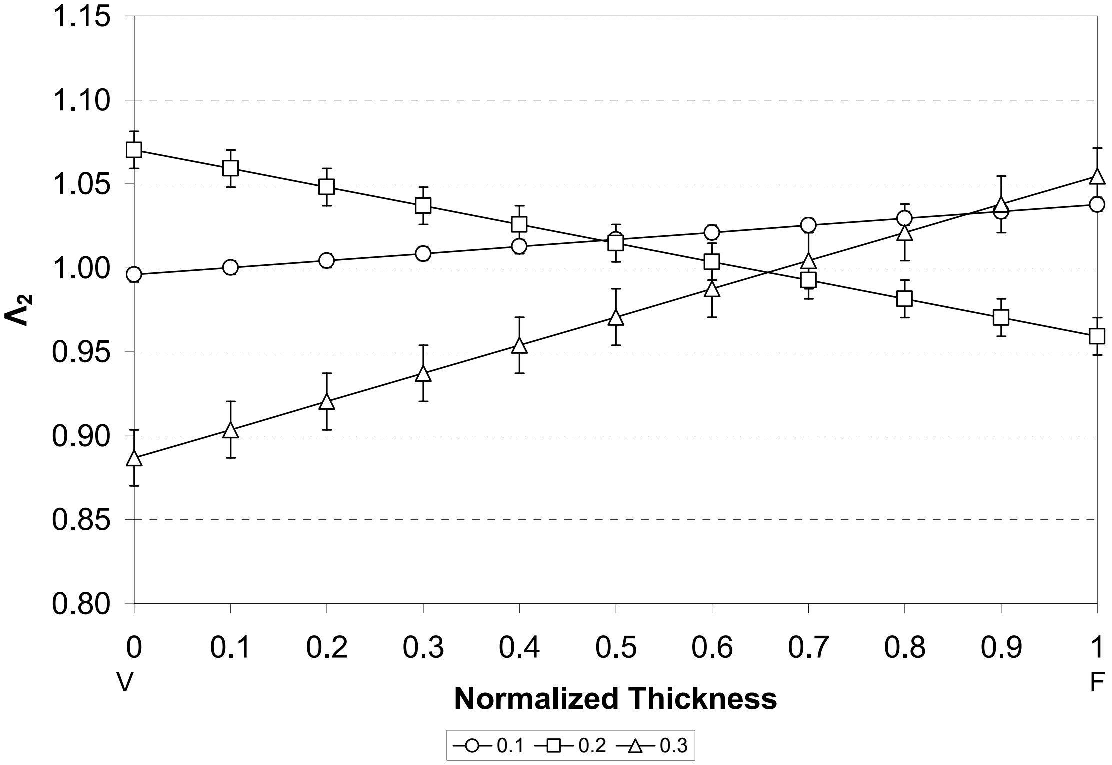

Figure 54, The regression lines from WC pulmonary valve samples at three curvatures were averaged together to create composite regressions lines representing the values of Λ_2 plotted against the normalized thickness of the tissue. Error bars are SEM.

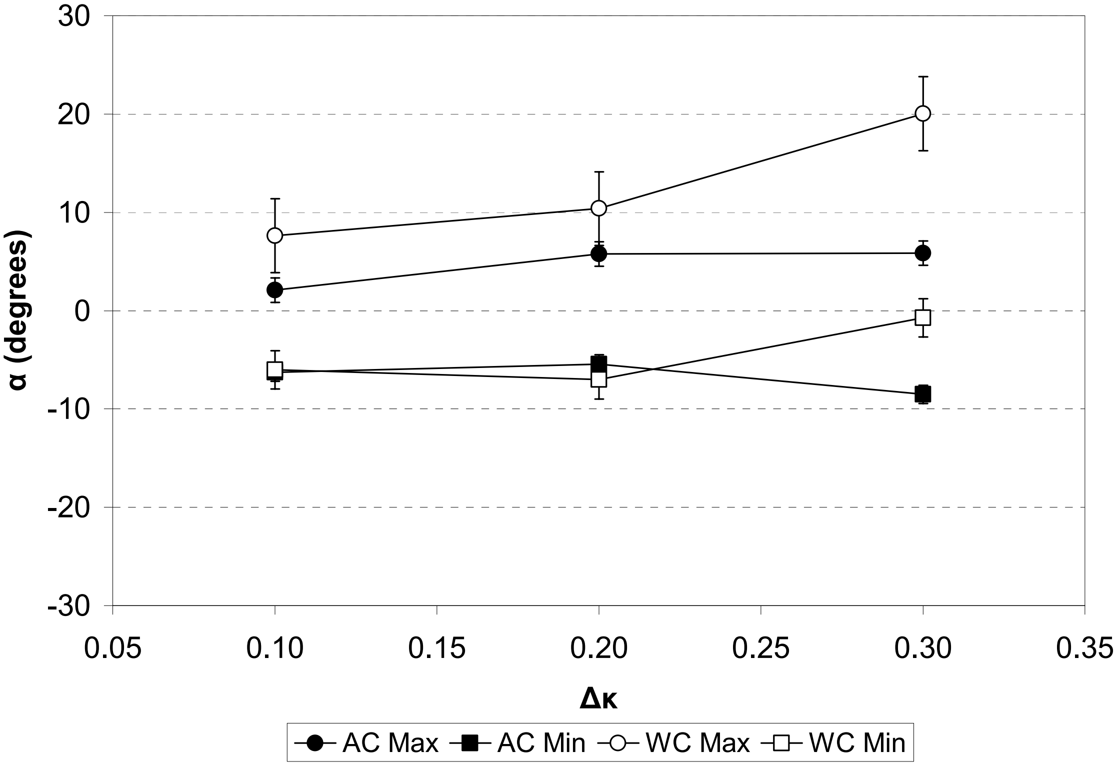

Figure 55, These results show the change in the shear angle α for the pulmonary valve along the thickness of the tissue at three different levels of curvature. Error bars are presented as SEM. There were no statistically significant differences.

Table 6 – Neutral Axis Location values at three different levels of curvature for the pulmonary valve showing the progression of the neutral axis towards the fibrosa. Neutral axis values are presented as normalized thickness with the ventricularis at 0 and the fibrosa at 1. Error is reported as SEM. There was a statistically significant difference (p=0.030) between the bending directions at 0.1 change in curvature.

		Against Curvature (AC)		With Curvature (WC)	
		AV	**PV**	**AV**	**PV**
$\Delta\kappa$	**0.1**	0.61±0.09	0.54±0.05	0.55±0.10	0.47±0.04
	0.2	0.59±0.10	0.54±0.10	0.56±0.10	0.50±0.11
	0.3	0.60±0.07	0.56±0.04	0.56±0.03	0.49±0.09

Table 7 – Tabulated U11 values showing maximum and minimum U11 values at three different levels of curvature for AC and WC directions. Tensile and compressive strains increase with increasing flexure in both bending directions. Error is reported as SEM. There were no statistically significant differences.

		Against Curvature (AC)		With Curvature (WC)	
		Maximum	**Minimum**	**Maximum**	**Minimum**
$\Delta\kappa$	**0.1**	1.04±0.03	0.96±0.03	1.07±0.03	0.93±0.04
	0.2	1.04±0.03	0.95±0.02	1.09±0.05	0.91±0.06
	0.3	1.07±0.04	0.92±0.01	1.09±0.02	0.90±0.05

Table 8 – U22 values at three levels of curvature showing an increase in the maximum U_{22} in the AC direction with increasing flexure and a decrease in the minimum U_{22} in the WC direction with increasing flexure. Error is reported as SEM. There were no statistically significant differences.

		Against Curvature (AC)		With Curvature (WC)	
		Maximum	**Minimum**	**Maximum**	**Minimum**
$\Delta\kappa$	**0.1**	1.19±0.30	0.86±0.14	1.22±0.21	0.85±0.18
	0.2	1.12±0.05	0.91±0.11	1.18±0.11	0.89±0.09
	0.3	1.16±0.02	0.87±0.15	1.09±0.09	0.85±0.08

Table 9 – Shear angle α values in degrees at three levels of curvature measured in degrees showing a gradual increase in the shear angle with increasing flexure. Error is reported as SEM. There were no statistically significant differences.

		Against Curvature (AC)		With Curvature (WC)	
		Maximum	**Minimum**	**Maximum**	**Minimum**
$\Delta\kappa$	**0.1**	2.11±0.98	-6.25±5.54	7.62±7.09	-6.02±4.47
	0.2	5.78±2.39	-5.43±3.88	10.38±15.42	-7.03±5.38
	0.3	5.87±2.75	-8.52±6.21	20.02±14.55	-0.72±4.42

3.3 BIAXIAL TEST RESULTS

Eight porcine aortic leaflet biaxial experiments and six porcine pulmonary leaflet biaxial experiments were performed. The results from the biaxial experiments were summarized by plotting values of the membrane tension applied against the corresponding stretches obtained. Figure 59 shows the typical collection of plots generated by the different protocols for the aortic specimens and figure 60 shows the typical collection of plots generated by different protocols for the pulmonary specimens. Figure 61 illustrates the differences between the equibiaxial protocols of the pulmonary and aortic leaflets. Note that the pulmonary leaflets could only be tested to a maximum membrane tension of 30 N/m whereas the aortic leaflets were tested to a maximum membrane tension of 60 N/m. Table 9 and 10 summarize the axial coupling results obtained between the aortic and pulmonary leaflets in the circumferential and radial stretch directions, respectively. Figures 62 and 63 illustrate the axial coupling values summarized in tables 11 and 12. Axial coupling data was obtained from the both leaflets at a maximum tension level of 30 N/m.

Table 10, Mean U_{11} and U_{22} stretch values from the 1:1 protocol for aortic and pulmonary leaflets at 30 N/m and 60 N/m of tension. Values are reported with their standard error.

U11			**U22**		
	30 N/m	**60 N/m**		**30 N/m**	**60 N/m**
PAV	1.14±0.02	1.14±0.02	**PAV**	1.54±0.04	1.57±0.04
PPV	1.08±0.01		**PPV**	1.64±0.06	

Table 11, Mean values accompanied by standard error showing the percent change in maximum stretch from the 1:1 equibiaxial protocol for several different stretch ratios in the circumferential direction. Significant differences between the AV and PV results are denoted with p-values under the appropriate stretch ratio.

Circumferential Direction (U_{11})							
AV	**0.1:1**	**0.5:1**	**0.75:1**	**1:1**	**1:0.75**	**1:0.5**	**1:0.1**
Mean	-11.52±2.08	-3.85±0.69	-1.31±0.28	0.00±0.00	1.06±0.09	2.64±0.41	5.41±1.18
PV	**0.1:1**	**0.5:1**	**0.75:1**	**1:1**	**1:0.75**	**1:0.5**	**1:0.1**
Mean	-13.53±2.47	-7.87±1.30	-2.84±0.49	0.00±0.00	2.58±0.55	4.46±0.86	7.61±1.29
p-value		p=0.013	p=0.014		p=0.008		

Table 12, Mean values accompanied by standard error showing the percent change in maximum stretch from the 1:1 equibiaxial protocol for several different stretch ratios in the radial direction. Significant differences between the AV and PV results are denoted with p-values under the appropriate stretch ratio.

Radial Direction (U_{22})							
AV	**0.1:1**	**0.5:1**	**0.75:1**	**1:1**	**1:0.75**	**1:0.5**	**1:0.1**
Mean	4.91±0.45	2.77±0.33	1.34±0.22	0.00±0.00	-0.94±0.28	-6.01±2.45	-16.80±1.51
PV	**0.1:1**	**0.5:1**	**0.75:1**	**1:1**	**1:0.75**	**1:0.5**	**1:0.1**
Mean	7.01±1.16	4.33±0.82	1.56±0.66	0.00±0.00	-3.01±0.55	-5.90±0.81	-18.00±1.32
p-value					p=0.004		

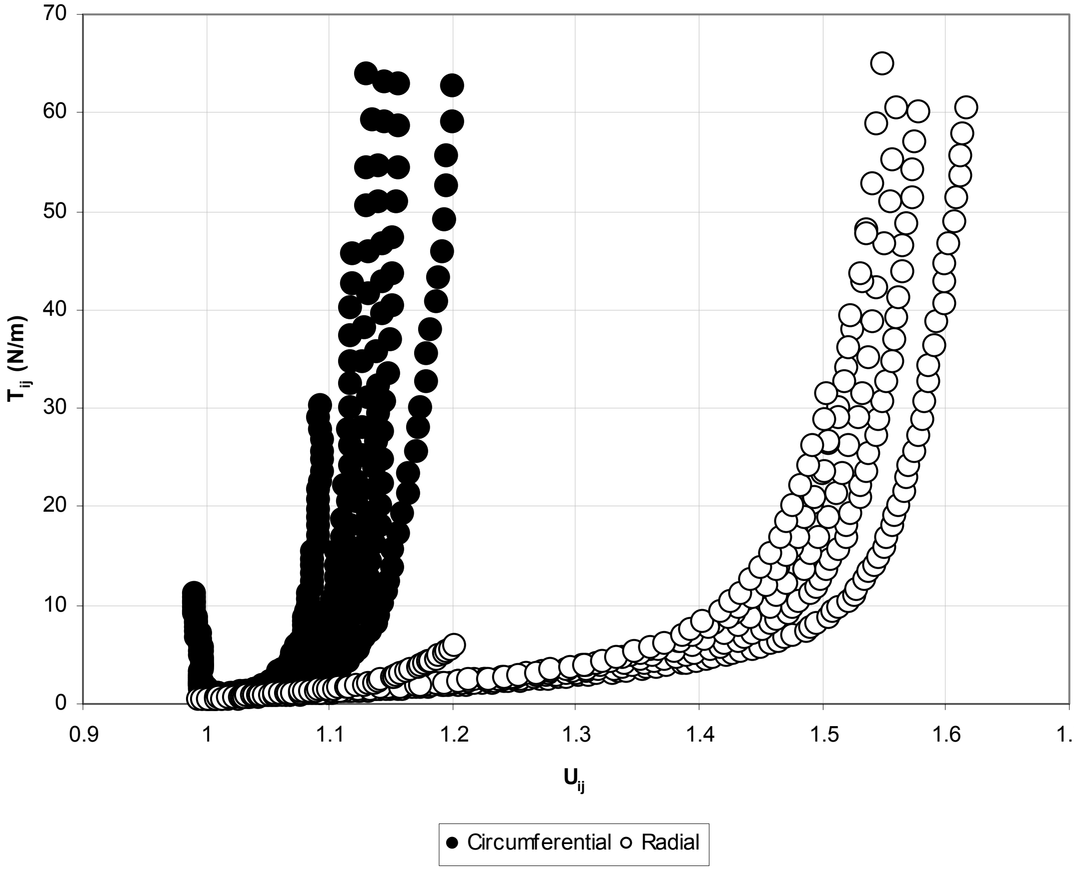

Figure 56, Chart showing the spread of load versus stretch responses of the native porcine aortic valve leaflet to varying biaxial stretch ratio testing protocols.

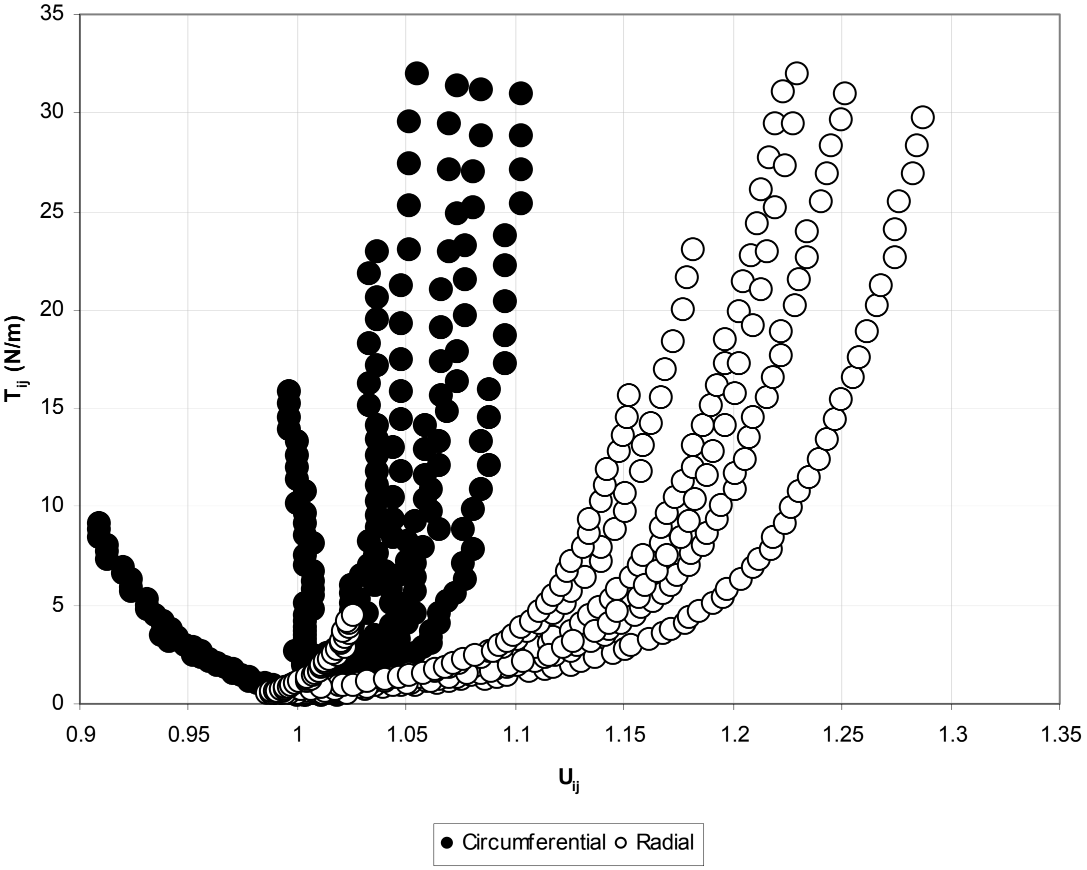

Figure 57, Chart showing the spread of load versus stretch responses of the native porcine pulmonary valve leaflet to varying biaxial stretch ratio testing protocols.

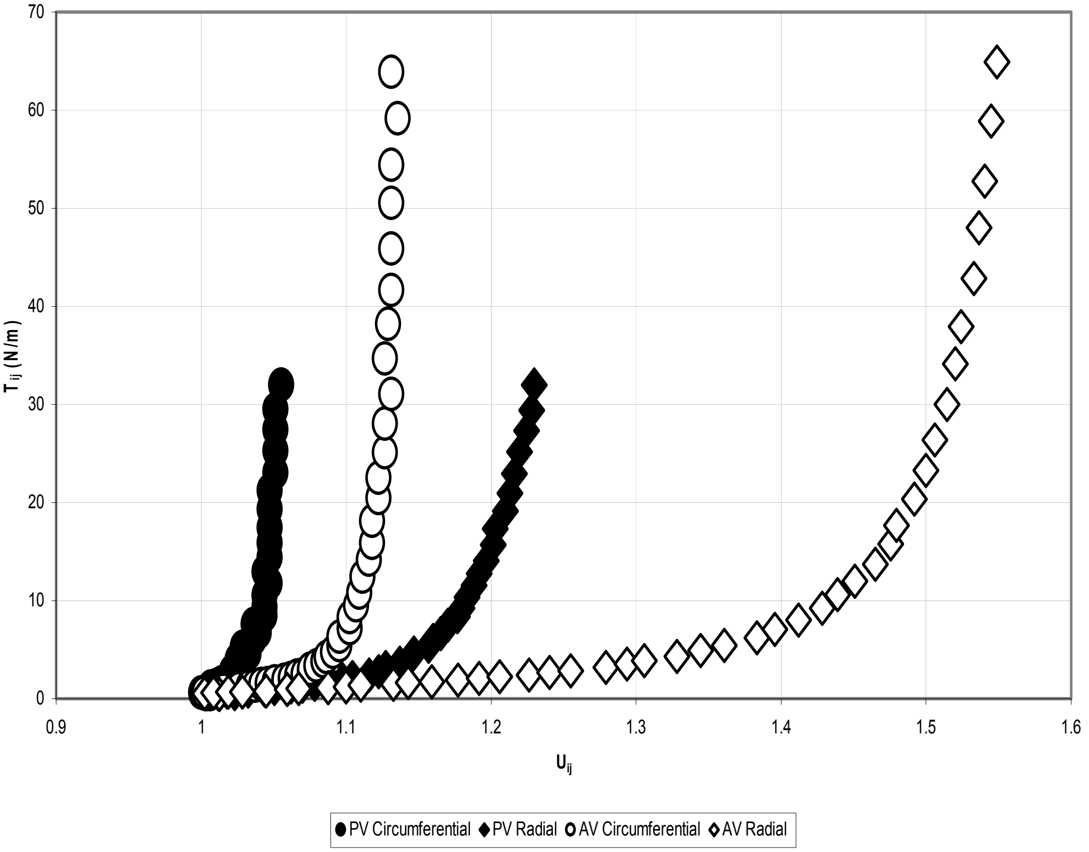

Figure 58, Chart showing the representative circumferential and radial load versus stretch curves obtained for native porcine aortic and pulmonary leaflets under equibiaxial conditions.

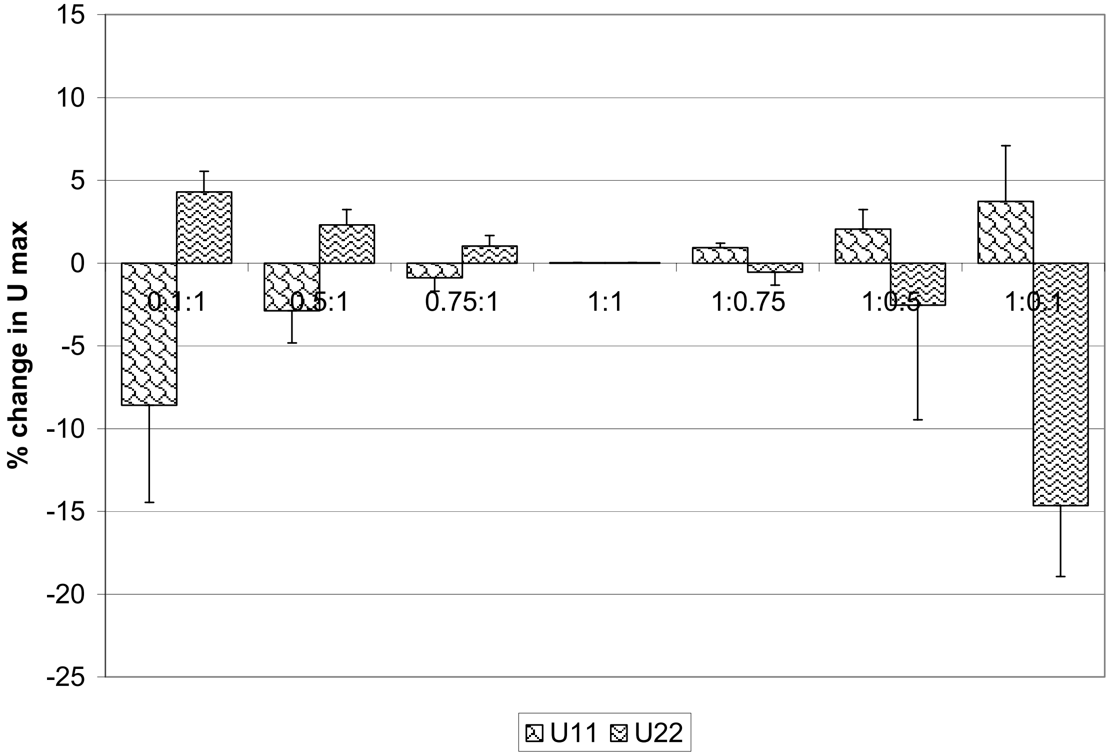

Figure 59, Chart showing the percent change from the equibiaxial state in U_{11} (circumferential direction) and U_{22} (radial direction) at several different stretch ratios for native porcine aortic valve leaflets.

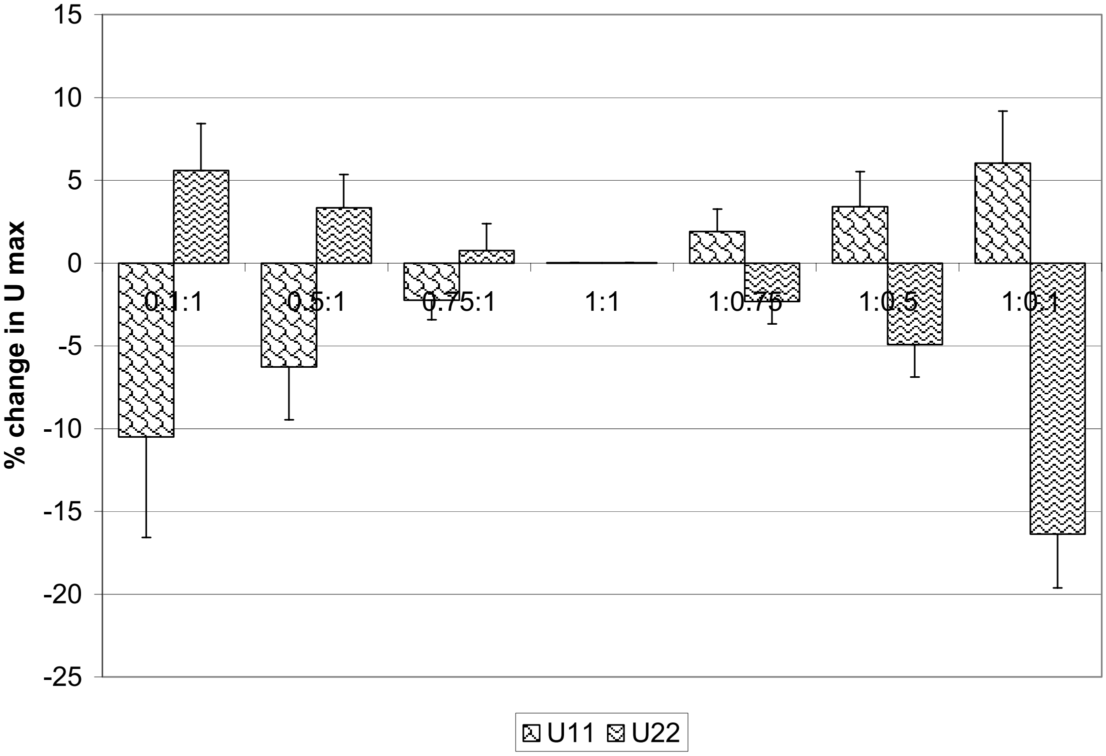

Figure 60, Chart showing the percent change from the equibiaxial state in U_{11} (circumferential direction) and U_{22} (radial direction) at several different stretch ratios for native porcine pulmonary valve leaflets.

3.4 VALIDATION RESULTS

Tensile tests upon the silicone rubber confirmed that it possessed a Young's modulus of 3.3 MPa which was also obtained using the bending device. Repeatability testing was confirmed after averaging the moduli to achieve the same Young's modulus of 3.3 MPa.

Table 13, Table summarizing a set of tensile tests performed to determine effective stiffness of silicone.

Tensile Test to 5% Strain		
Test #	**E (Pa)**	**E (MPa)**
1	3298426.60	3.298
2	3293070.84	3.293
Average		**3.296**
Standard Error		*0.003*

Table 14, Table summarizing repeatability results performed to determine the differences between bending directions.

Specimen normal	**Bending direction**	**E (MPa)**	**Specimen normal**	**Bending direction**	**E (MPa)**
Up	Down	3.59	Down	Down	3.28
Up	Down	3.61	Down	Down	3.24
Up	Down	3.56	Down	Down	3.22
Up	Down	3.56	Down	Up	3.37
Up	Down	3.56	Down	Up	3.31
Up	Down	3.36	Down	Up	3.30
Up	Down	3.50	Down	Up	3.30
Up	Down	3.52	Down	Up	3.30
Up	Down	3.44	Down	Up	3.27
Up	Down	3.49	Up	Up	3.80
Up	Down	3.58	Up	Up	3.75
Up	Down	3.51	Up	Up	3.71
Down	Down	3.08	Up	Up	3.71
Down	Down	3.22	Up	Up	3.70
Down	Down	3.22	Up	Up	3.61
Down	Down	3.22	Up	Up	3.60
Down	Down	3.22	Up	Up	3.75
Down	Down	3.24	Up	Up	3.63
Down	Down	3.29	Up	Up	3.69
			Average		**3.41**
			Standard Error		*0.03*

4.0 DISCUSSION

This study sought to determine the mechanical differences between the porcine aortic and pulmonary valve leaflets by examining their flexural behavior and micromechanical behavior through novel biomechanical testing, as well as contrasting these behaviors with biaxial mechanical testing.

4.1 SUMMARY OF FINDINGS

4.1.1 Flexural behavior

EI values were obtained from the moment curvature plots at a change of curvature of 0.2 (Fig. 38) and tabulated. The flexural rigidity (the product of the effective modulus and second moment of the area) was demonstrated to be roughly equivalent between the AC and WC flexural directions and between the two leaflet types (Fig. 39). The effective modulus, E_{eff}, determined from the data (Fig. 40) showed that the tissues exhibited similar behavior in the WC and AC directions but demonstrated different results when compared to each other. The effective modulus for the pulmonary valve was observed to be statistically higher than the aortic valve by a factor of a little less than two. This result of the effective modulus, however, cannot be taken completely without some caution because of this measurement's dependence upon the second moment of the area which is calculated using the thickness cubed. The similarities between the flexural rigidity results are interesting because they show that the leaflets provide approximately the same magnitude of resistance to an applied moment. Only when the thicknesses of the leaflets are taken into account are differences observed between them. These results illustrate the similarities between the function of the leaflets but also the apparent differences considering the variation of thickness between the two types of valves.

4.1.2 Transmural strain

In both bending directions, increasing curvature caused a slight statistically insignificant shift of the neutral axis towards the fibrosa in the aortic valve. The overall location of the neutral axis suggested that the fibrosa was stiffer than the ventricularis. This conclusion was confirmed by comparing the maximum and minimum Λ_1 stretches of the ventricularis and fibrosa faces in the two different bending directions. In the AC direction, the ventricularis faced the interior of the tissue curvature and the fibrosa the exterior and vice versa for the WC direction (Fig 1). Consequently, according to bending theory and experimental results, the ventricularis was under tension and the fibrosa was under compression in the X1 direction of AC bending and vice versa for WC bending. The ventricularis appeared to be more extensible than the fibrosa in tension. The neutral plane determined from the Λ_1 vs normalized thickness plots was biased towards the fibrosa layer in all bending directions and curvature levels. With increasing changes in curvature, the neutral plane was found to shift slightly towards the fibrosa. The compressive strains for the layers were comparable in both bending directions suggesting similar compressive behavior for the ventricularis and fibrosa. In the natural state, though, the differences between the layers was slight with only the difference in the maximum Λ_1 stretch at 0.2 change in curvature being statistically significant.

Similar to the behavior of AV leaflets, the PV specimens demonstrated progressive movement of the neutral axis towards the fibrosa with increasing flexure although to a lesser degree. The difference between the neutral axis and the halfway mark of tissue thickness was determined to be essentially insignificant in both valve types. The PV minimum Λ_1 results demonstrated increased levels of compression in the WC bending direction compared to AV specimens. The similarity between bending directions exhibited in the AV was also apparent in the PV data with differences between the AC and WC bending directions being statistically insignificant.

Shear angle α measurements illustrated a negligible amount of shearing at the center of the tissue during bending. For all directions of bending, maximum shearing angles occurred at the fibrosa and ventricularis faces. Insignificant differences between U_{11}, the pure stretch information, and Λ_1, combined stretch and shear information, were observed. The overall trend for α over the increasing change in curvature was not as obvious as those for the neutral axis and maximum and minimum U_{11} stretches. For WC samples, the shear angle exhibited increases with changes in curvature. The change in thickness of the leaflet represented by U_{22} and Λ_2 showed interesting results suggesting the tissue underwent significant thickness changes. The composite trends of Λ_2 versus normalized thickness showed increasing thickness changes with flexure in the WC direction and decreasing thickness changes in the AC direction.

4.1.3 Biaxial results

The experimental results from the biaxial tests on the native porcine aortic and pulmonary leaflets demonstrated some significant differences between their responses. The pulmonary leaflets were not tested to the membrane tension of 60 N/m that the aortic valves were tested to because the pulmonary leaflets, in general, were not capable of withstanding that level of tension without tearing at the hook attachment points. Although the membrane tension versus stretch plots for the pulmonary leaflet end at 30 N/m, their comparison to the aortic leaflet plots show the large difference in extensibility between the two.

The axial cross coupling results demonstrated a significantly greater change in circumferential stretches in the pulmonary valve in a limited number of stretch ratios. This showed that, although the pulmonary leaflets were subject to a lower maximum stretch at 30 N/m, they experienced a somewhat greater change in stretch in the circumferential direction with certain ratios.

4.2 HYPOTHESES: INTERPRETATION OF FINDINGS

4.2.1 Flexural behavior

The indifference between bending directions could be attributed to the distribution of stress and strain throughout the structure of the leaflet. Fibers may not be solely responsible for material response and observed behavior may result from different mechanisms such as the sliding of fibers. Furthermore, the compressive behavior of the layers was shown to be similar in the transmural data suggesting that a structural component other than the fibers such as the GAGs could have been responsible. The increased stiffness could also be an adaptation to the low pressure environment, a lack of adaptation to a high pressure environment, or a consequence of structural features.

4.2.2 Transmural strain

The shift of the neutral axis towards the fibrosa may be accounted for by the greater concentration of inelastic collagen (1-2% strain) within the fibrosa and the greater concentration of elastin in the ventricularis. Previous studies have shown that the elastin in the ventricularis forms a honeycomb network around the collagen fibers, allowing the fibers to stretch and return to their initial state [67, 68]. The collagen fibers in the fibrosa do not possess an extensive or organized elastin network and are bound together more tightly [69]. Thus, the different levels of stretch and the location of the neutral axis allude to differing tensile stiffnesses of the two layers, however, because of the statistical insignificance of the shift, the tissue could essentially be assumed to be isotropic in nature. The layers would not possess any significant differences in stiffness if they were approximately equal in size within the leaflet. The fibrosa, though, tends to be slightly thicker than the ventricularis introducing the possibility that may yet possess different stiffnesses but exhibit isotropic behavior when combined as the composite leaflet.

Because the leaflets had not been fixed in glutaraldehyde, the glycosaminoglycans in the spongiosa were preserved [19]. This water rich, compression resistant layer loosely located between the other two layers probably played a significant role in distributing and withstanding the compressive strains of the leaflet. Thus, fixation with glutaraldehyde would remove whatever contribution the glycosaminoglycans have towards the proper flexing of the leaflet in addition to exacerbating the differences in the behavior of the layers [26].

Increasing shear with increasing changes in curvature would be expected as the different layers of the tissue were stretched to a greater and greater degree. However, the absence of any observable trends in shear could be an indication to the role the spongiosa plays in permitting layer sliding and alleviating shear stresses within the leaflet. This sort of mechanism would be advantageous to the operation of the valve because it would act as a kind of internal damper that reduces the magnitude of shear stresses while simultaneously isolating them to the proper structures.

The variation in thickness in the WC direction may be attributed to the already undulated surface of the fibrosa undergoing compression and becoming even more convoluted. The increases in the hills and valleys of the fibrosal surface may cause changes throughout the leaflet as collagen fibers are pulled together, apart or tighter. The AC results are more difficult to understand because of the inverse relationship between Λ_2 and flexure. The undulations of the fibrosa could be expected to straighten with applied tension resulting in increasing thickness changes with increasing flexure. The observed behavior suggests an auxiliary mechanism at work or some sort of caveat relating flexure in the AC direction to the microstructure of the leaflet that is still unclear.

Under tensile conditions, the AV can be expected to be stiffer than the PV because of a greater concentration of collagen (due to higher transvalvular pressures) and its increased thickness [17]. The values of maximal Λ_1 stretch at the fibrosal surface support this notion because of the higher levels of stretch obtained in the PV leaflet than the AV leaflet. The stiffness of the AV may also be attributed to a fiber organization more highly aligned with the circumferential and radial directions or a greater density of collagen and perhaps a reduced collagen crimp [30].

A structural difference between the PV and AV must be responsible for the difference in compressive ranges for the two. In the WC direction, the fibrosa undergoes compression while the ventricularis is under tension. The similar compressive ranges for the AV were hypothesized to be caused by the contribution of GAGs and independent of the fibers present. The collagen fibers within the fibrosa can be assumed to be as weak in resisting compression as they are strong under tension. The organization or distribution of GAGs within the PV must assume a different pattern from AV leaflets to account for differences in maximum compression. The AV results supported the hypothesis that the layers were sufficiently separated with GAGs in the spongiosa to permit sliding between the layers. The PV results suggest structural differences are present that alter the leaflets response to bending stress. The increased stiffness of the leaflet in both bending directions may be a result of increased cross-linking between individual fibers or reduced GAG content that effectively curtails the sliding and movement of fibers. The leaflet consequently has less freedom reorganizing its internal structure to respond to applied stress, shifting the burden of compressive strains upon all of its constituents [70]. Thus, a less elastic leaflet would resist flexure more prominently, as demonstrated in the bending experiments. The reduction in the maximum strains of the ventricularis in tension may be attributed to the increase in fiber cross-linking and absence of substantial fiber movement. The collagen fibers in the PV fibrosa play a greater role in compression than in the AV and are understandably strained to a greater degree. In tension, however, they exhibit similar characteristics as in the AV specimens

4.2.3 Biaxial behavior

The aortic leaflets proved to yield more than the pulmonary leaflets in biaxial tension alluding to some structural difference between the two but most probably due to a difference in collagen and elastin organization. An increased presence of elastin and higher levels of collagen crimp within the aortic leaflet would be required to allow the leaflet to stretch more. The orientations of collagen fibers within the pulmonary leaflet may become more highly aligned along the circumferential and radial directions during biaxial tension and thus provide more direct resistance to the biaxial load. Elevated elasticity in the aortic leaflet could possibly be attributed to the requirement that the leaflet withstand greater transvalvular pressures and be more flexible to do so. This observation was possibly a result of the decreased maximum stretch of the pulmonary leaflet and the subsequently lower resistance of the leaflet micro-structure to applied load. The discrepancy between the stiffnesses of the leaflets in the flexure experiments and the biaxial experiments may be a result of the response of the tissue at different magnitudes and modes of loading. The loading experienced in the biaxial tests was significantly higher than those in flexure so the leaflets may behave differently at different levels of load to compensate. Thus the stress-strain response of the aortic and pulmonary valve may not be entirely linear but perhaps somewhat sigmoidal in nature with the pulmonary valve being stiffer than the aortic valve at lower stresses and reaching a lower maximum stretch than the aortic valve at higher levels of stress. This difference could be hypothesized to be directly related to the differences in operating pressures the two valves experience. These differences in tissue behavior underscore the importance of rigorous soft tissue testing through the use of multiple testing regimens. Complex tissue structure and function cannot be fully explained without thorough examination from varying points of view. These puzzling findings confirm the rationale behind including biaxial experiments with flexural analyses in providing an adequate picture of complexity of soft tissue mechanics.

4.3 RELATION TO PREVIOUS STUDIES

By exploring the mechanical behavior of the aortic and pulmonary leaflets in relation to their flexural properties and the interactions amongst their key structural components, a rough understanding of how these materials function so effectively in their individual environments has been achieved. In flexure, a physiologically faithful mode of deformation, the PV proved to be stiffer than the AV in contrast to biaxial experiments showing the contrary [17]. Christie et al examined the biaxial behavior of both native and glutaraldehyde fixed porcine aortic and pulmonary valve leaflets and found that they possessed similar stretch behavior circumferentially but that radially the pulmonary leaflets were more extensible which counter the findings in this study [17]. Differences in testing methodology may be responsible for these discrepancies since Christie et al used randomly placed markers and also introduced a suture at their location of strain measurement. From their results they hypothesize that the collagen content of the pulmonary valve is lower than that of the aortic valve which resonates with this study's findings that lower collagen may be responsible for the pulmonary valve's reduced tensile strength. Vesely et al found that the pulmonary valve cusps were capable of greater stretch but were also stiffer than their aortic counterparts [71]. Their tests, however, were uniaxial in nature and performed on cryopreserved valves and the effects of that treatment may have altered their results from the native state. This study, through flexural and biaxial experiments has shown that the difference between the pulmonary and aortic valve leaflets is not so profoundly distinctive that one can be said to be completely stiffer or extensible than the other. Via transmural strain measurements, the interaction of layer structures between the two valves was shown to differ, causing the observed behavioral differences.

4.4 EXPERIMENTAL DIFFICULTIES AND LIMITATIONS

4.4.1 Experimental difficulties

Specimen 'curling.' The leaflet specimens were cut to dimensions that had been determined large enough to accommodate the large curvatures and small enough to prevent curling in the radial direction. All strips cut from the leaflets curled along the lengthwise edges towards the ventricularis. This phenomenon could most likely be attributed to the presence of pre-stressed elastin in the ventricularis [19]. This pre-stress was released from the tissue when the strip was cut from the leaflet. The curling effect upon the leaflet specimens did not modify the geometry of the specimen sufficiently to prevent moment curvature relationship measurements. However, some samples experienced sufficient curling at the edges to prevent them from being used in the transmural studies. The strips were flexed at 500 micron increments until the two ends of the tissue were approximately 7 mm apart. Samples that did not bend properly from the approximately horizontal state to the approximately circular shape were eliminated.

Pulmonary valve 'thinness.' The decreased thickness of the PV leaflets relative to their AV counterparts, 250 microns compared to 360 microns respectively, presented several significant difficulties in performing experiments. The area used for transmural imaging was significantly reduced, complicating the application of the markers and reducing the number of viable markers available for analysis. The curling effect previously observed in the AV strips was exacerbated in the PV leaflets due to their thinness.

4.4.2 Limitations

The limitations of the study were primarily in the task of post-processing image for determining transmural strains and the preparation of tissues for testing. The established technique of airbrushing micron-sized ink particles possessed significant drawbacks that affected the ease and efficiency of performing experiments. There were no assurances to the density of particle coverage particles or particle size so tissue samples that have been prepared but airbrushed improperly cannot be tested. Several different alternative methods were attempted including using small fluorescent micro-spheres (ranging in size from 5 to 20 microns) pressed into or affixed to the tissue with an agarose gel. The use of the spheres failed because of the inability for the spheres to affix properly to the tissue. Other attempts involved the use of fluorescent cell staining, however, the technique proved too complicated to properly execute given testing conditions and was also abandoned. The development of an effective means of applying micron sized markers to the edge of the tissue would greatly enhance the efficiency of testing as well as reduce the introduction of experimental error. Improvements upon the established methods of manually matching the markers from their reference positions to their deformed positions would greatly expedite testing so that experimental results could be obtained within a short time of its completion.

The accuracy of results was highly dependent upon the behavior of the tissue when placed into an experimental situation. The steel sleeves mounted on the edges of the tissue were fitted over posts in the specimen bath during testing and the rotation of these sleeves about the posts was assumed to be frictionless. Although the sleeves were made to fit loosely they would have experienced some resistance in rotating. The method of zeroing the bending bars before the beginning of an experiment discussed above was the most straight-forward way of ensuring that no force was being applied to the tissue. However, variations between the zero-load state from one test to another could have existed because of the need for user adjustment of the bending bar and zeroing bar. The variability inherent in biological tissues cannot be controlled and differences between leaflets lend themselves to introducing significant variability in the measurements taken for this experiment. Improvements in testing and handling of soft tissues would significantly improve the quality of data as well as ease the burden of interpretation.

4.5 FUTURE RESEARCH DIRECTIONS

The work performed in this research project provides insight into the mechanical behavior of the aortic and pulmonary leaflets and establishes some fundamental differences between them. Further experiments examining leaflet behavior at higher levels of curvature could possibly show any behavioral differences they may exhibit with increased flexure. To continue along this vein, other properties about the valves must be studied with respect to the current methods of treating valve disease. Planned studies include examining the effects of glutaraldehyde fixation upon the bending and transmural strain behavior of the aortic valve leaflet. Because of the prevalence of using glutaraldehyde treatments in heart valve replacements, it is important to see how these behaviors deviate from the natural leaflet. This information could improve the current understanding of the damage mechanisms of glutaraldehyde treated heart valve replacements. Of course, these experiments would be conducted on tissue at varying concentrations of glutaraldehyde and under different fixation pressures. Using the device, the changes in bending and transmural behavior of leaflets undergoing fatigue could also be explored. Thus, changes in the leaflet as a whole can be attributed to any changes that may occur in the layers with time. It would also be interesting to determine the flexural and biaxial behavior of the pulmonary leaflet after its transplantation into the aortic position to observe what changes may occur with the increased operating pressures and what possible remodeling could be occurring.

5.0 CONCLUDING REMARKS

This study has succeeded in illustrating that there are interesting differences between the native porcine aortic and pulmonary valve leaflet biomechanical behavior. Through flexural experimentation, the pulmonary valve has been shown to be stiffer than the aortic valve in flexure but less compliant than the aortic valve through biaxial testing. The interactions between the layers of the leaflets lend an isotropic nature to the leaflet in flexure but do so through mechanisms that are not fully understood. For heart valve leaflet replacement therapy, this study illustrates the biomechanical differences between the aortic and pulmonary valve leaflets and emphasizes the need to fully characterize the two as separate but related entities. The pulmonary valve cannot be thought of as simply a thinner or smaller version of the aortic valve. The effective stiffness measurements and the extensibility of the valves in biaxial testing show this. The results also demonstrate the complexity of native valve function and how nature has evolved this structure to serve its purpose in a masterful way. Although both the aortic and pulmonary leaflets are constructed as composite materials with very different layers of varying composition, they behave relatively isotropically in flexure. However, under tensile conditions provided by biaxial testing, the leaflets show an increased strength and can withstand greater stress. This dichotomy is puzzling at first but

The results obtained within this thesis illustrate a general need for scientific researchers to explore a previously overlooked level of detail within human physiology, namely, the tissue level. Whereas great advances are currently being made towards the elucidation of the mechanical properties and physiology of organs and their components and the methods of exploring molecular biology and their mechanisms are firmly established, the methods for determining the structure and function of biology between these two levels are under-developed. Understanding the interactions of microscopic structures such as collagen and elastin fibers is critical to understanding the response of the tissue as a whole and how all these elements combine to provide a functioning component of the organ system. These studies also reveal some before-unknown properties of the leaflets, namely their isotropic nature in flexure, that may influence the current approach towards developing and using biomaterials for producing valve replacements. By understanding some of the features inherent in the natural leaflet, researchers and designers can seek to duplicate these features and produce a more effective valve replacement.

APPENDIX

BENDING DEVICE MANUAL

Introduction

The bending device incorporates two systems that work together to characterize the bending properties of an appropriately sized tissue specimen. The bending moment-curvature relationship can be determined for a specimen using the macro camera. The transmural strain distribution of the specimen can be determined using the micro camera. The two systems work in unison to expedite tissue testing and to avoid excessive handling and manipulation of specimens. Bending data is collected automatically by the driving control PC during the test and saved to disk for analysis. Transmural data is obtained by post-processing images with Labview software and Matlab scripts.

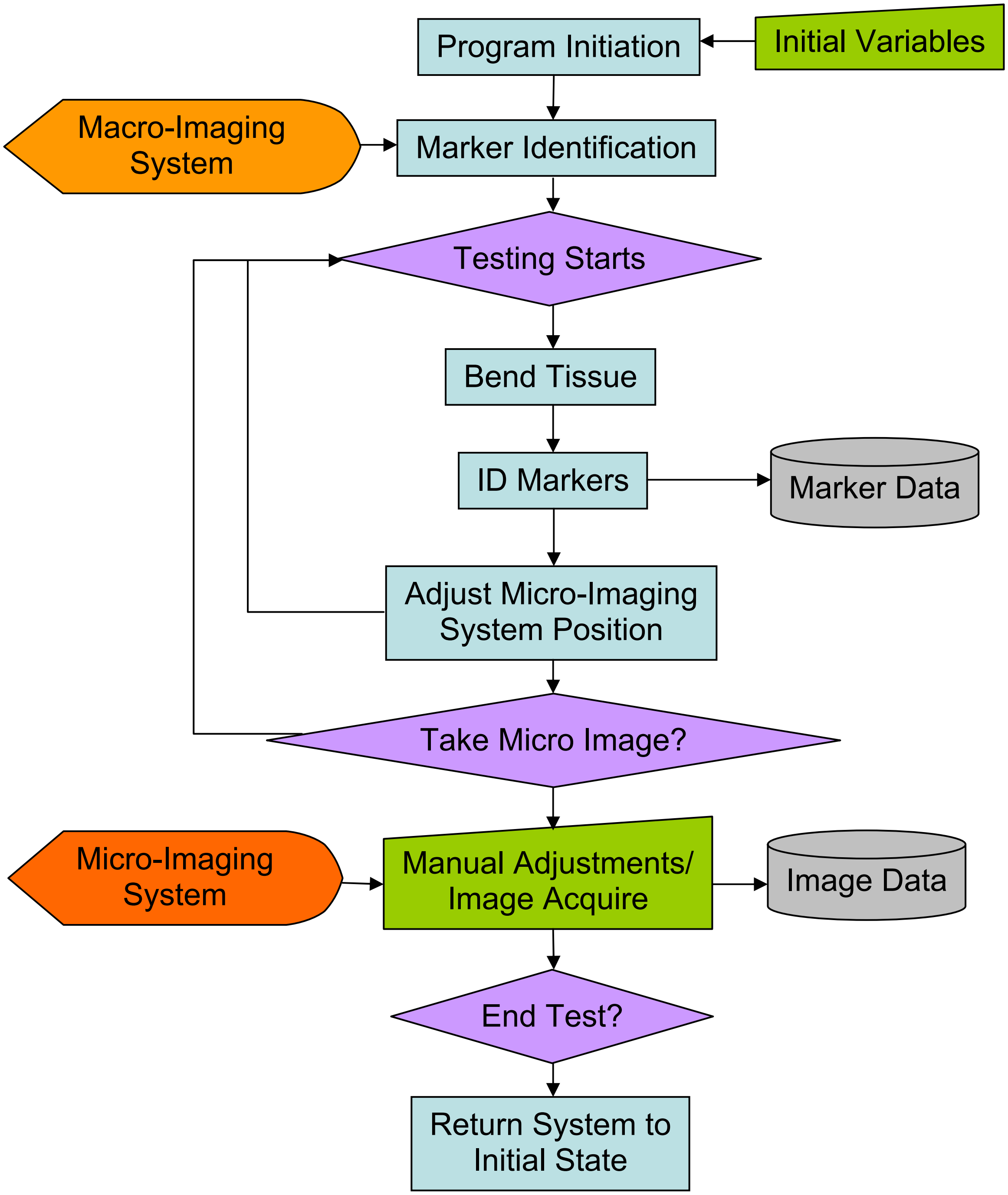

Figure 61, Flowchart describing the main functions of the testing program.

Components

The bending device consists of the following components:

Macro Camera System

XC-1 (Sony, 640x480 resolution CCD camera)

55mm FL Telecentric Video Lens (Edmund Industrial Optics)

PCI-1407 (National Instruments, analog capture board)

Micro Camera System

PL-1642 (PixeLINK, 1 MegaPixel CMOS 1394 camera)

VZM-1000i (Edmund Optics , high magnification video lens)

Motor Control

MC-4SA (National Aperture, MicroMini servo amplifier system)

MM-4M-F (National Aperture, Folded Motorized MicroMini Stage)

MM-4M-EX (National Aperture, Extended Motorized MicroMini Stage)

PCI-7344 (National Instruments, motor control board)

Motorized Stages

The motorized stages that control horizontal translation are MM-4M-EX motorized stages. The motorized stage controlling the motion of the specimen chamber will be referred to as **Axis 1** and is motorized stage MM-4M-EX-80. The motorized stage controlling the horizontal motion of the high magnification camera is referred to as **Axis 2** and is motorized stage MM-4M-EX-50. The motorized stage controlling the vertical motion of the high magnification camera is referred to as **Axis 3** and is motorized stage MM-4M-F-50.

Table 15, Motors used for different axes of motion in bending device.

Axis	NAI Motion Model #	Function
Axis 1	MM-4M-EX-80	Horizontal translation for specimen chamber
Axis 2	MM-4M-EX-50	Horizontal translation for high magnification camera
Axis 3	MM-4M-F-50	Vertical translation for high magnification camera

Table 10 summarizes this information regarding the motorized stages. The stages are attached to the MC-4SA amplifier system and are activated via the Axis 1-3 switches. The MC-4SA interfaces via a 68-pin connector to the PCI-7344 motor controller board in TMLFLEX. Control of the motors is all performed through the Labview interface. Measurement and Automation Explorer allows specific settings to be set for the motor system. By default, Axis 1 has been renamed Testing Stage and has been set to Servo mode with an encoder resolution of 896 encoder counts per revolution. By default, Axis 2 has been renamed Horizontal Zoom and has been set to Servo mode with an encoder resolution of 896 encoder counts per revolution. By default, Axis 3 has been renamed Vertical Zoom and has been set to Servo mode with an encoder resolution of 2560 encoder counts per revolution. By default, Axis 4 has been disabled. Other motor settings are left at the initial defaults. Control of the three motors is provided by the VI *motormover*. Six Boolean inputs are provided turning on and off movement in the three directions.

PixeLINK Camera

The PL-1642 is a color CMOS camera with a 1 megapixel resolution that is controlled via the Firewire IEEE-1394 bus card installed in TMLFLEX. Camera functions are not directly supported by Labview but an API provided by PixeLINK provides the functions necessary to control the camera. Using the *call library* function in Labview, the PixeLINK functions can be accessed by Labview during execution of the test. The DLLs are called using standard windows calling and arguments are specified according to the PixeLINK API manual. Images can be obtained two ways. The slower method of image capture would be return frames from the video stream of the camera and convert them to the image format used by Labview. This way of importing images into Labview permits the use of Labview image processing routines upon the video stream from the camera in real-time. To do so, the raw data from the camera is returned using a PixeLINK DLL and then converted to an image using the Labview function *Array to Image*. The buffer containing the data returned from the PixeLINK DLL must be reserved before calling the VI. This method is not very fast. The second method of obtaining images from the camera is to use the camera's preview window capabilities to display a preview window. Images are captured using the *MegaCaptureFrametoBMP* function which captures a frame from the video stream and writes it to the specified path in bitmap format. The following functions in Table 2 have already been prepared for use with Labview.

The PixeLINK Megapixel Firewire Camera Developer's Manual is attached at the end of this manual and provides all the necessary information regarding the functions included in the

API. Also attached is the include H file that defines many of the constants used by the PixeLINK API functions.

Table 16, PixelLINK DLL functions incorporated into Labview custom VIs to permit the use and control of firewire camera functions including image acquisition.

Function and VI name	**Purpose**
MegaCaptureFrametoBMP	Capture and save frame to a BMP file
MegaInit	Initialize PL-1642 camera and obtain imager handle
MegaPausePreview	Pause/restart preview window
MegaReturnStillFrame	Returns a still frame
MegaSetDataTransferSize	Set the data transfer size (bpp)
MegaSetExposureTime	Set camera exposure time in milliseconds
MegaSetImageFlip	Set horizontal and vertical image flip
MegaSetImagerClocking	Set the oscillator type and clock divisor
MegaSetSubWindowSize	Set the size of the imager subwindow
MegaSetVideoMode	Set video mode to STILL_MODE (0) or VIDEO_MODE (1)
MegaStartPreview	Start preview window
MegaStartVideoStream	Open video stream from camera
MegaStopPreview	Stop and close preview window
MegaStopVideoStream	Close video stream from camera
MegaUninitialize	Uninitialize camera

Labview Interface

Labview is a graphically driven programming environment that is closely married with hardware input/output and control. A Labview program comprises of a Front Panel and a Block Diagram. Labview functions are referred to as Visual Instruments or VIs. VIs are connected with wires that control the flow of data and information from one VI to another. The piecing together of wires and VIs is performed in the Block Diagram (Fig. XX). The square boxes represent VIs. The blue pull-down menus are rarely used options set by the user in the Block Diagram. The green controls link the Block Diagram to the Front Panel in the form of controls. The Front Panel displays information from the Block Diagram and serves as the user interface. On the Front Panel, buttons, toggle switches, and dialog boxes serve as user input and control for the program. Digital readouts, meters, and graphs are used to display data and status. The bending device takes advantage of two Labview programs.

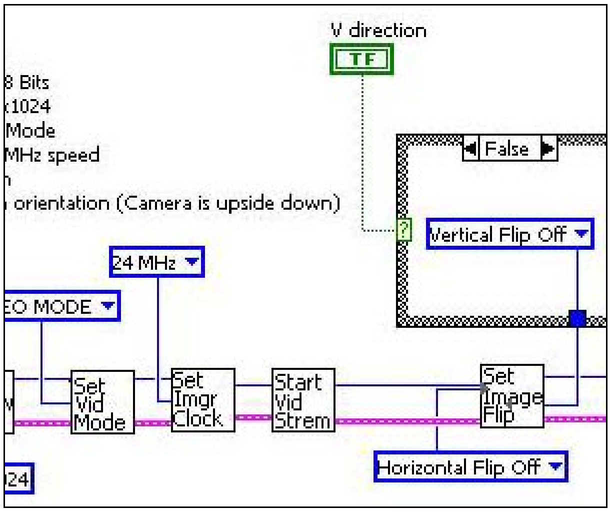

Figure 62, Block Diagram example

programv23.vi: This program is responsible for all tissue testing operations. It collects user requirements for testing parameters and automates the three subsystems to complete an experiment with the minimum of user intervention. Data collected during the experiment is graphically displayed by the program during the experiment and also saved to disk for further processing and analysis. Experiments are performed in three stages necessitating three integrated Front Panels.

transmuralv2.vi: This program is responsible for the post-processing of images captured from the micro camera for the purpose of transmural strain determinations. It takes advantage of a dual monitor computer to display the reference and deformed images concurrently so that markers identified by the program can be matched between them.

The Front Panel interfaces of both programs will be discussed to explain their major features and use.

Labview Interface: Positioning

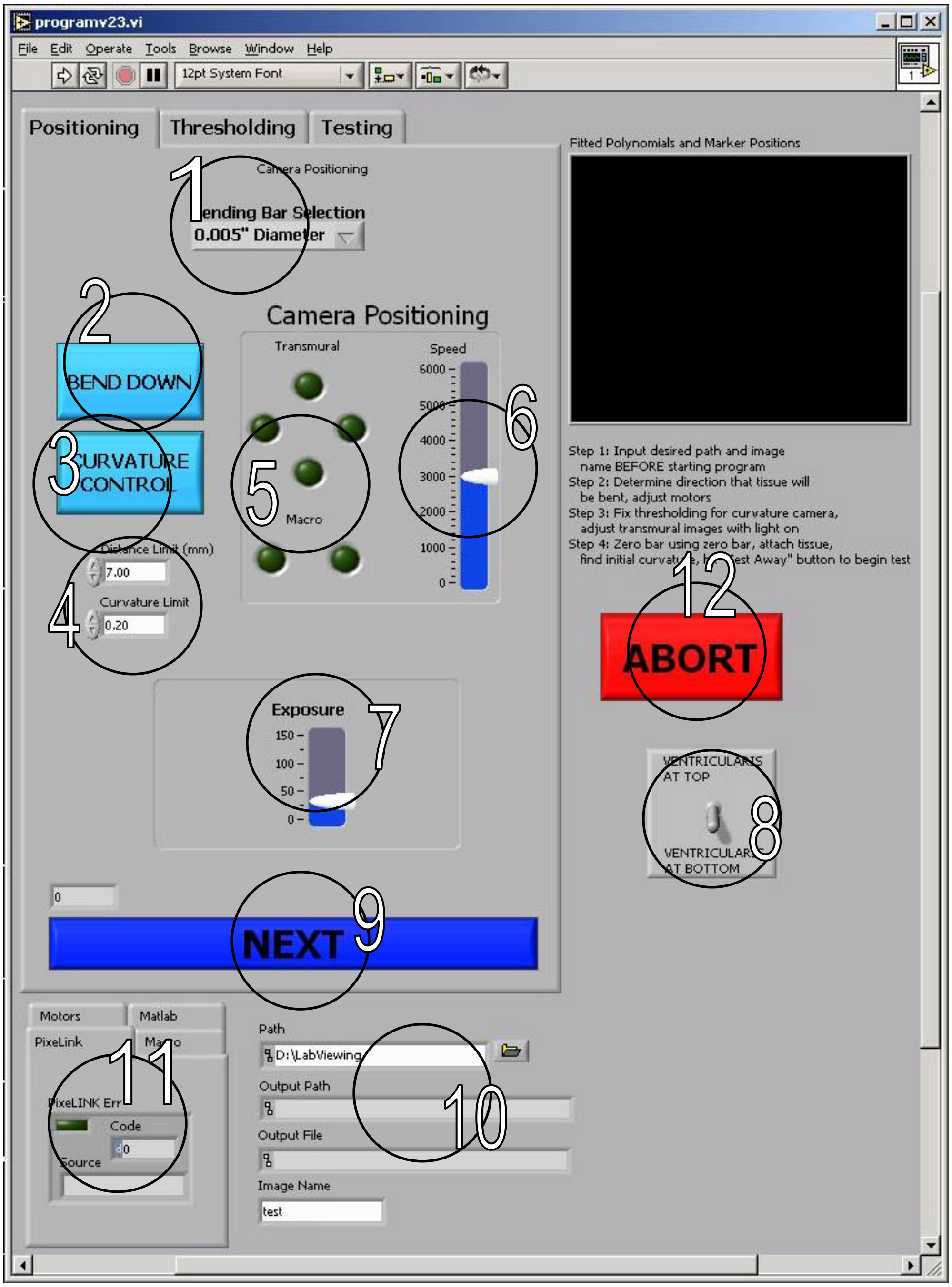

ending Bar Selection: 0.005" Diameter

Distance Limit (mm): 7.00

Curvature Limit: 0.20

0

Step 1: Input desired path and image name BEFORE starting program

Step 2: Determine direction that tissue will be bent, adjust motors

Step 3: Fix thresholding for curvature camera, adjust transmural images with light on

Step 4: Zero bar using zero bar, attach tissue, find initial curvatu[illegible]e, h[illegible]est Away" button to begin test

PixeLINK Err
Code: 0
Source:

Path: D:\LabViewing

Output Path:

Output File:

Image Name: test

Figure 63, Program interface for positioning

1: The Bending Bar Selection pull down menu is used to select the proper diameter for the bending bar being used in the experiment. This selection must be made **BEFORE** executing the VI to ensure that the proper bending bar size is registered with the program. Additional entries in the pull down menu can be added in the VI source by inputting another title entry and another scaling entry. The scaling entry is a number determined from the calibration of the bar and is used to determine the force being exerted by the bar from the displacement of the bar.

2: The Bend Up/Down button is used to specify the direction the tissue is flexed during the experiment. When the tissue is concave downwards, the tissue is flexed upwards and vice versa. Selecting the proper direction of bending is important for the program to use the proper marker tracking algorithms. This selection should be done **BEFORE** the program is executed.

3: The Curvature Control/Distance Control button is used to specify to the program the control algorithm to be used for termination of the experiment. Under Curvature Control, the experiment ceases when the tissue reaches a preset level of curvature specified in the input box in item 4. Under Distance Control, the experiment ceases when the distance between the two ends of the tissue dips below a preset distance value specified in item 4. This selection must be done **BEFORE** the program is executed.

4: The two input boxes are used to set the limits for the termination of the experiment. The selection made in item 3 dictates which of the two limits are employed during the experiment. The limit that was not selected does not affect the outcome of the experiment. This selection must be done **BEFORE** the program is executed.

5: The two sets of controls are responsible for controlling the three servo stages. The Transmural buttons are responsible for controlling the movement of the micro camera horizontally and vertically. The directions on the panel are referenced to the point of view of the camera so the horizontal translation is reversed in the macro camera view. Vertical translation remains unchanged regardless of the point of view. The Macro controls control the movement of the servo stage responsible for moving the specimen bath horizontally. These controls are referenced to the point of view of the macro camera.

6: The slide control is responsible for controlling the speed of the camera. The gradations are with respect to the number of counts per minute the servo motors are run at. Adjustments to the speed of the motors should be made while observing the movement of the cameras and the testing stage to ensure proper movement. These adjustments do not affect the movement of the servo stages later in the program. All servo stages are affected by these speed changes.

7: The level of exposure controlled in this slide control is for the micro camera. The units of the controller are in milliseconds. Acceptable values range between 0 and 1000 milliseconds, however, the useful range is between 0 and 150 milliseconds. Behind this control is the *MegaSetExposureTime* VI which interfaces with the PixeLink API function *MegaSetExposureTime*.

8: This switch is responsible for adjusting the orientation of the cameras to account for the orientation of the tissue sample. By default, the ventricularis is always located at the bottom of the sample. This adjustment must be made **BEFORE** the program is executed.

9: The large *NEXT* button is used to transfer control of the program to the second stage after all of the initialization steps have been followed.

10: The path of the data files and the name of the specimens are input in the dialogs at item 10. The output paths and files are then output by the program for user information. The path is automatically generated by the program from the path specified by the user. Each execution of the program receives a unique path name that incorporates the current date and the time of execution.

11: This cluster of tab controls and dialog boxes houses all of the programs error reporting abilities. Different tabs represent different subsystems of the program. Any errors reported in the PixeLink tab emanate from the portions of the program dealing with the PixeLink camera. The Macro tab shows any errors emanating from the macro camera system. The Motors tab shows any errors that originate from the servo stages and its control system. The Matlab tab shows any errors that may have occurred in any of the Matlab scripts included in the program. Normally, Matlab does not report detailed error information but only if the script failed to execute properly.

12: The *ABORT* button is used only in the third stage of testing when a test has actually commenced. If for any reason the test proceeds outside of normal conditions, the *ABORT* button is used to terminate the program. Otherwise, the system may not be able to detect a problem with the test and may destroy the tissue. The servo stages themselves are protected with limit switches to define their range of movement but are independent of the device design and orientation of attachments.

Labview Interface: Thresholding

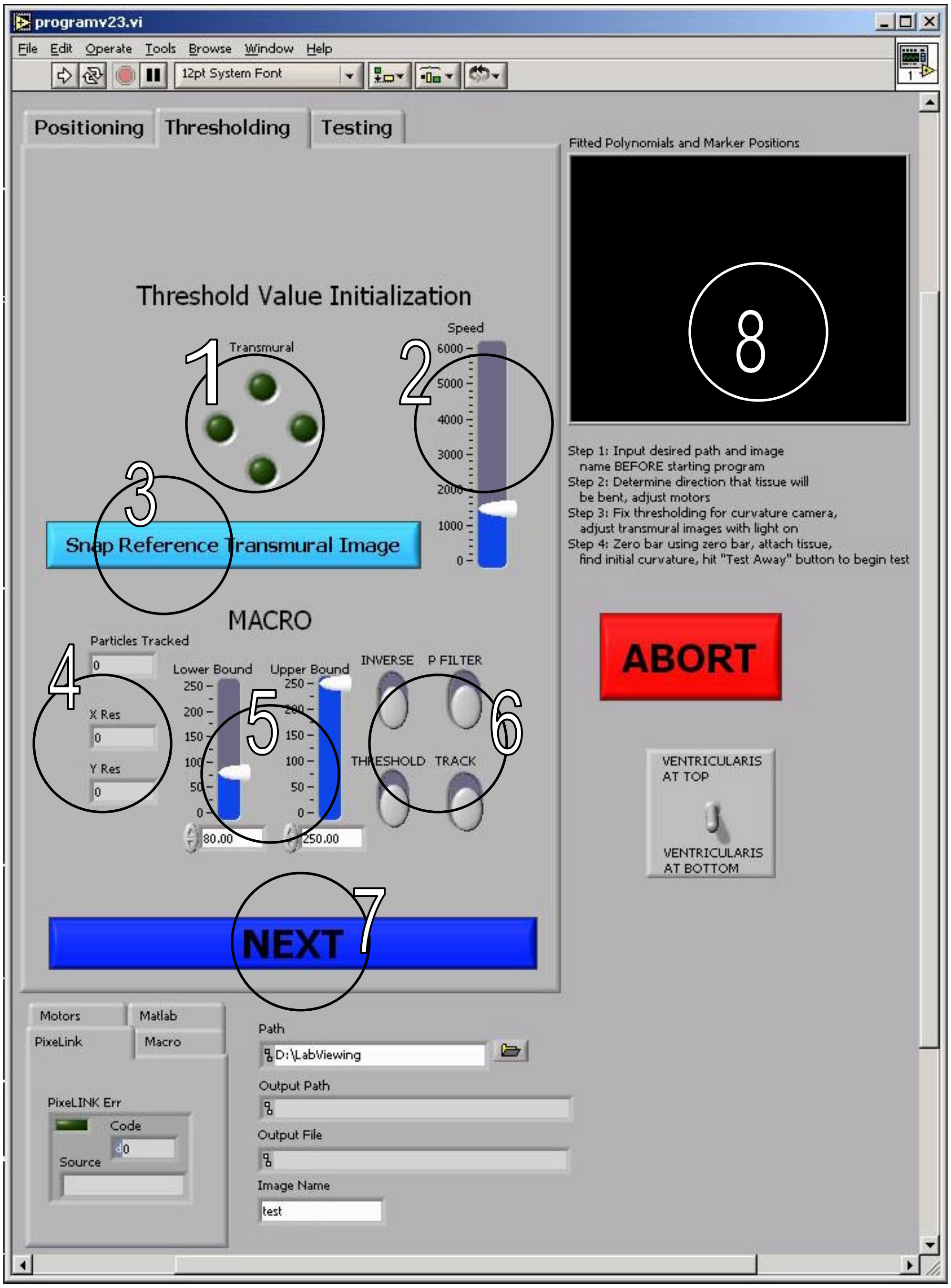

Step 1: Input desired path and image name BEFORE starting program

Step 2: Determine direction that tissue will be bent, adjust motors

Step 3: Fix thresholding for curvature camera, adjust transmural images with light on

Step 4: Zero bar using zero bar, attach tissue, find initial curvature, hit "Test Away" button to begin test

Particles Tracked: 0

X Res: 0

Y Res: 0

Lower Bound: 80.00

Upper Bound: 250.00

Code: 0

Path: D:\LabViewing

Image Name: test

Figure 64, Program interface for thresholding

1: These buttons are similar to the Transmural buttons in stage one in that they are responsible for the movement of the micro camera for positioning purposes. These controls are also oriented with the point of view of the micro camera.

2: The speed control slider functions exactly as the speed control slider found in stage one.

3: The *Snap Reference Transmural Image* button captures the image currently displayed on the micro camera and saves it to the hard disk. The images taken are used as the reference state for the transmural analysis that is performed after the end of the test. The files are always named '*refstateXXXX.bmp*' where the XXXX is provided by the iteration number of the program. This numbering system ensures that no reference images are overwritten. The image is saved in the output path as a bitmap to ensure that no information is lost through compression.

4: The display in item 4 reports, from top to bottom, the number of particles detected in the macro camera by the software, the horizontal resolution of the micro camera, and the vertical resolution of the micro camera. It is important to note the number of particles detected do not and should not equal the number of markers placed on the tissue. There will always be two extra markers in the image, the static left-most marker on the post and the bending bar marker at the right. Extra particles detected during the test will confound the software and corrupt the data obtained.

5: The two slide controls and digital inputs are used to determine the low and high ranges of the thresholding the images in the macro camera. These must be adjusted to ensure that the markers are isolated against the background while eliminating everything else in the image. As a rule of thumb, the values reached for a specific camera setup normally can be used for subsequent experiments. As always, the lower threshold bound should always be lower than the upper bound.

6: The four toggle switches turn on and off the following functions for the macro camera: Inverse inverts the colors of the image, turning white to black and black to white. The P Filter toggle eliminates small (<XX pixels) detected objects in the image as well as any black objects that are located along the borders of the image. This toggle can be used to eliminate any erroneous objects that cannot be eliminated by thresholding. The Threshold toggle is used to turn the thresholding of the image on and off. The Track toggle switches on and off the marker tracking functions. This toggle is used to ensure that the proper objects are being identified as markers for the rest of testing.

7: The large *NEXT* button is used to transfer control of the program to the third stage after all of the initialization steps have been followed.

8: This window displays the identified and tracked markers as empty circles on a coordinate system localized to the area the tissue will move. The quadratic equation that is fitted to the marker coordinates is also displayed superimposed upon the markers so that the accuracy of the fit can be determined quickly by visual inspection.

Labview Interface: Testing

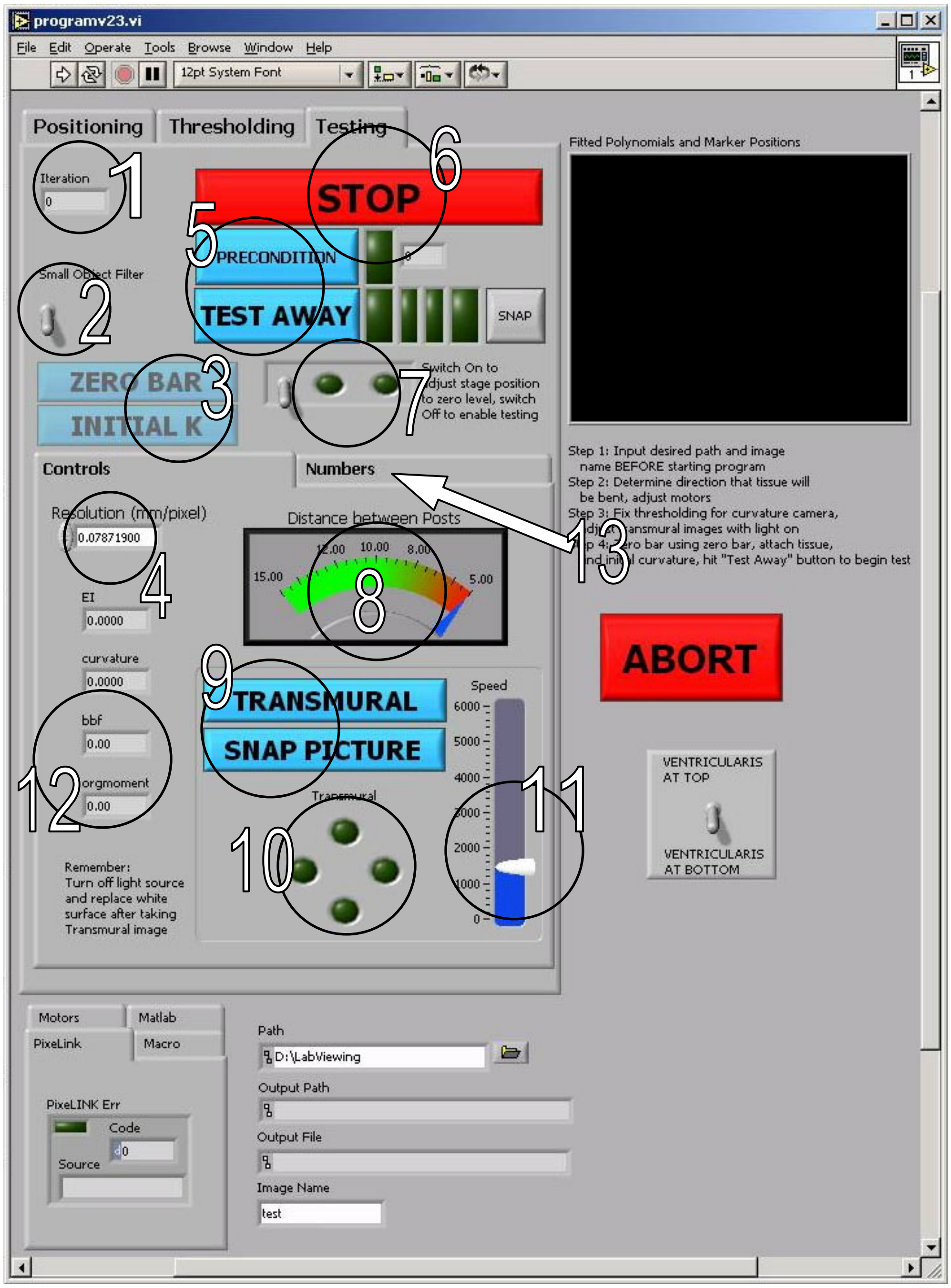

Iteration 0

Small Object Filter

Switch On to adjust stage position to zero level, switch Off to enable testing

Resolution (mm/pixel) 0.07871900

EI 0.0000

curvature 0.0000

bbf 0.00

orgmoment 0.00

Remember:
Turn off light source and replace white surface after taking Transmural image

Step 1: Input desired path and image name BEFORE starting program
Step 2: Determine direction that tissue will be bent, adjust motors
Step 3: Fix thresholding for curvature camera, adjust transmural images with light on
Step 4: Zero bar using zero bar, attach tissue, find initial curvature, hit "Test Away" button to begin test

Code 0

Path D:\LabViewing

Output Path

Output File

Image Name test

Figure 65, Program interface for testing

1: The number of iterations the program goes through is displayed for informational purposes. The iteration number is used to name files saved to the hard disk to ensure that no files are overwritten.

2: The Small Object Filter toggle switch serves the same purpose as the P Filter toggle switch on the second stage. To enable small particle filtering, this switch must be enabled even if it was enabled in the second stage when setting up the thresholding levels. The thresholding levels, however, are maintained.

3: The Zero Bar button is used to set the displacement of the bending bar detected by the software as zero so that the force registered by the bending bar will be recorded as zero at the onset of testing. The Initial K button is used to initialize the curvature detected by the software by recording the current curvature and displaying and recording the difference between the current curvature and this initial curvature. It is important to zero the bending bar and the curvature so that the data outputted by the recording system will be correct. Otherwise, the data will have to be post-processed manually to account for the initial displacement of the bar and the initial curvature.

4: The resolution control refers to the resolution of the macro camera in millimeters per pixel. This resolution is set beforehand by taking an image of a calibration grid using the macro camera and determining the number of pixels per millimeter using SigmaScan Pro software. This resolution determination does not need to be repeated unless the position of the camera or the testing stage changes. Calibrating the camera is discussed in its own section.

5: The Precondition button is used to instruct the program to precondition the specimen. Using the control algorithms specified during the first step, the system will bend the tissue back and forth a total of 10 times. The LED next to the Precondition button lights up when the system is preconditioning and the digital readout next to the LED records the number of preconditions the specimen has had. The Test Away button is depressed to begin testing after all of the options have been set and the specimen is ready. This relinquishes control to the program as it begins to bend the tissue up to the earlier set limits. The program will move the tissue in small increments, collecting data all the while and recording a macro camera image at every increment. It suspends the bend test and switches to the micro camera system when running under curvature control. This permits the user to capture images from the micro camera for transmural strain analysis later.

6: The large *STOP* button can be depressed to terminate the program anytime before the *TEST AWAY* button has been pressed. Pressing the *STOP* button during testing will terminate the program as well but will not reset the servo stages to their initial positions, requiring them to be repositioned manually. To terminate testing, the *ABORT* button detailed in stage one should be used. This will stop the testing regimen and return the system to its initial state.

7: Unfortunately, there will be times when the specimen must be flexed more or less so that it may be positioned properly for the experiment. This may occur when attempting to bend a stubborn tissue against its natural curvature. When the toggle is switched on, the *TEST AWAY* button is disabled to prevent accidental test activation. Only the testing stage may be moved with the direction controls. Adjustments using this control should only be used when the specimen is difficult to work with and only *after* the bending bar has been zeroed and *before* the initial curvature is captured.

8: The Distance between Posts meter measures the distance between the two posts in mm. The first post is the static marker in the specimen bath and the second post is the marker on the bending bar. The distance between the posts should be controlled to prevent the device from damaging the bending bar and the specimen.

9: The *TRANSMURAL* button activates the cluster of controls in items 9, 10, and 11. It can be used by the user any time during testing to switch to the micro camera to capture images. Otherwise, the computer program will enable the transmural mode automatically when the curvature limit has been reached. The *SNAP PICTURE* button saves an image from the video stream to the hard disk. The files will be named according to the Image Name input in the first stage in the format *nameXXTYY.bmp*. The XX is replaced with the number of iterations the program was at when it was suspended into transmural mode. The YY is replaced with the number of iterations of the transmural subsystem. This ensures that no images are overwritten.

10: In some cases it may be necessary to adjust the position of the micro camera. Normally, the tissue should be within the field of view of the camera or very close, depending on how accurate the servo stage calibrations are. In some instances, the micro camera image window must be moved to increase its update priority and maintain a smooth frame-rate.

11: The speed of the servo stages controlling the micro camera position can be controlled via the slider as earlier described in stage one.

12: This cluster of displays show the values obtained by the system for EI, the current curvature of the tissue, the bending bar force being exerted (bbf), and the moment at the center of the tissue. The EI is obtained by dividing the current moment with the current change in curvature. The curvature of the tissue is what is recorded to the data file so it is affected by initializing the curvature. The bbf is calculated from the displacement of the bending bar along with the corresponding calibration factor. The moment at the center of the tissue is determined by finding the vertical distance of the center of the tissue from the axis defined by the posts and multiplying it by the bbf.

13: The *Numbers* tab hides a variety of reported data values from the system that were used for debugging purposes. The initial curvature values, x and y coordinates of markers, coordinates of the posts, coordinates of the tracked point, the initial bending bar displacement, and the number of objects detected are displayed. The LED is a part of the curvature control system.

Calibrating the Macro Camera

The resolution of the macro camera is determined by finding the number of pixels that correspond to a known distance within an image. A millimeter graduated grid is used as the reference for the known distance. It is attached to a calibrating bar that can be maneuvered into position so that the grid is parallel with the specimen mounted in the bath. An image is acquired using the National Instruments Measurement and Automation Explorer software. The analog video capture board, the IMAQ PCI-1407, is listed under devices and interfaces. The camera is found under channel 0 of the board as an rs170 camera. MAX can display the video stream from the camera as well as capture still images for calibration purposes. The calibration image is opened using SigmaScan Pro 4.01 (SPSS Inc.).

Using SigmaScan Pro's calibration routines, the number of pixels per millimeter is determined:

1. Open the image in SigmaScan Pro
2. Under the *Measure* menu heading, select *Calibrate Distance and Area…*
3. In the *New Distance* block, enter the number of microns desired (for example, if you will be measuring on the image a 4 mm distance than you will want to enter 4000 microns, corresponding to the 4 mm). It is advisable to use a large value such as 4000 microns or more to calibrate the image. Small values will be more susceptible to measurement errors.
4. Click in the *Old Distance* block and then click on the *Image* button to obtain the *Old Distance* from the image itself.

5. Now you will have the opportunity to click upon the grid in the image. The distance clicked is the distance measured corresponding to the value entered in *New Distance*. It is advisable to click on the same part of the grid for each end point.
6. When the two points have been defined, the program will return a value into the *Old Distance* dialog box. This is the number of pixels between the two end points. The resolution is determined by dividing *New Distance* by *Old Distance*. In this example this would be 4000 microns divided by *Old Distance.* The units of the resolution are then microns/pixel. On average, the resolution should be around 80 microns/pixel.

Calibrating the Bending Bars

The force applied to the tissue specimens is measured using pre-calibrated bending bars. The bending bars are made of 316V stainless steel in varying diameters. The diameter of the bar determines the amount of force produced by the bar as a function of the bars displacement. The load displacement relationship of the bar is determined by using a microscale and a platform that can be moved in micron increments. Figure X2 illustrates the setup used to calibrate the bending bars. The bending bar is suspended horizontally to the microscale and rigidly fixed to the platform. An allen wrench is placed upon the microscale and the end of the bending bar is centered upon the wrench. Something must be placed onto the surface of the microscale to elevate the end of the bending bar so that the bar will not contact the microscale when it is deformed. The force the bar exerts upon the scale is determined at zero displacement of the bar. The bar is then displaced along regular intervals and force measurements from the microscale are taken. The load-displacement response of the bars is linear so a linear equation is fit to the data. Thus, for any given amount of bar displacement, the load can be accurately determined. This method of measuring force is convenient because it avoids the necessity of using expensive load cells that need to be constantly calibrated and maintained.

Transmural Post-Processing and Analysis

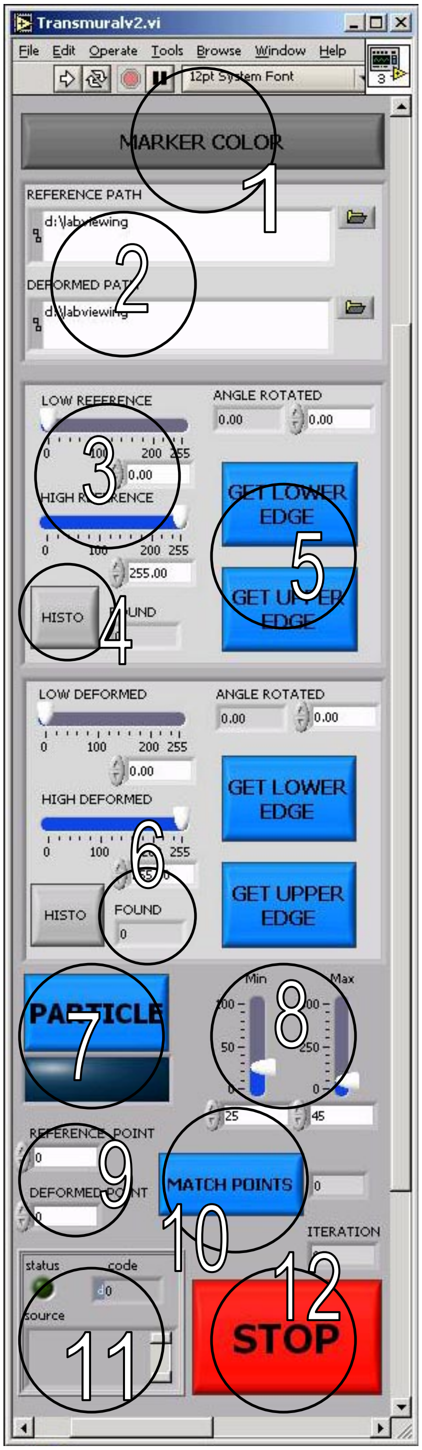

Figure 66, Marker matching interface

1: The color of the markers can be either black or red. For the majority of experiments, the markers airbrushed to the side of the tissue are black. By selecting the color of the marker, the program will use different algorithms to threshold and isolate the chosen colors against the background. When red markers are chosen, the button will be red.

2: The locations of the two images used for analysis must be specified. The reference image location is placed into reference path dialog box and the deformed image location is placed into the deformed path dialog box. The folder icons located on the right can be used to browse for the files.

3: *LOW REFERENCE* and *HIGH REFERENCE* refer to the upper and lower threshold bounds for the reference image displayed on the main display. These values must be adjusted to obtain balance between the white background and the black or red markers. *LOW DEFORMED* and *HIGH DEFORMED* are the upper and lower bounds for the deformed image. Separate thresholds are used for both images to account for different imaging conditions.

4: The *HISTO* buttons are used to turn on/off the thresholding of each image.

5: The *GET LOWER EDGE* and *GET UPPER EDGE* buttons are used to find the upper and lower edges of the specimen. When they are depressed, the user is allowed to select five points along the edge of the tissue which are then fit to a quadratic equation. The edge information is recorded to disk in their own files.

6: For both images, the number of objects found by the program's particle VIs is displayed. It is best to find a moderate number of markers because too many markers will clutter the display while too few will not provide sufficient markers for matching.

7: The *PARTICLE* button toggles the particle finding VIs. When particles are identified, a bounding box is drawn around the particle and overlaid onto the image along with the identifying number. The particles are found once and that image data is saved in the program. When the image containing the identified particle information is displayed, the large LED below the *PARTICLE* button is lit. To switch between the source image and the modified image, the LED can be turned on and off. When any of the threshold controls or particle size controls are changed, the *PARTICLE* button must be depressed to refresh the modified image.

8: The two slide controllers have different scales to accommodate the range of particles that may be identified with the software. These sliders are adjusted to eliminate particles that are too small or too large for use. They can also be used to isolate a group of markers so their identification and matching can be performed more efficiently.

9: These inputs are used to specify the identity of the matched marker in the reference and deformed images. The *REFERENCE POINT* input is hotkeyed as F1 and the *DEFORMED POINT* input is hotkeyed as F2. When a point is found in the reference image, its identifying number is input into *REFERENCE POINT*. Its corresponding point in the deformed image is input into *DEFORMED POINT*.

10: The two markers identified using item 9 are matched together by using the *MATCH POINTS* button. This has also been hotkeyed as F3. The number of matched points is displayed in the digital readout to the right of the button. When two points are selected to be matched, their areas and centroids are recorded in the file *matched.txt*. Their bounding boxes in the modified images are also filled to eliminate them from the image. The images are automatically re-processed to account for missing markers. Modifications to the image do not alter the source image stored on the hard disk. The sequence of key strikes should be F1, reference marker number, F2, deformed marker number, and then F3. The identification numbers of the all the markers in the image are likely to change when a marker is eliminated from the image.

11: Errors produced by the program are displayed in this error cluster. Most error-prone functions output their function name in the *source* dialog to ease debugging.

12: The *STOP* button terminates program execution. This is normally done after all the possible marker matches have been exhausted.

Post-processing of Transmural data

After matching the points using the transmuralv2 VI, a text file, *matched.txt* is generated. The first two columns are the x and y coordinates of the points in the reference frame, respectively. The third and fourth columns are the x and y coordinates of the points in the deformed frame, respectively. The fifth column is the u gradient, defined as $x_{deformed}-x_{reference}$ or X-x. This fifth column is calculated so that erroneously large values of u can then be discarded as these are most probably mismatches between points. Inclusion of these points in the analysis program will yield poor and inaccurate results. The edited *matched.txt* file should be saved as *data.txt* so that the analysis program, *loco.m* will be able to locate the data. The transmural VI will also output a text file, *edges.txt*. This text file contains the iteration at which the deformation image was taken at along with four sets of polynomial coefficients. These polynomials were used to define the upper and lower bounds of the reference and deformed images as they were picked out in previous versions of the transmural VI. Currently, the *edge.txt* file has no use. The *loco.m* also looks for the presence of the file *ac.txt*. The presence of this empty file prompts the program to modify the data for an **a**gainst **c**urvature test where the ventricularis is found at the top of the image and the fibrosa at the bottom. The data is flipped along the horizontal axis so that the ventricularis is located at the bottom of the image according to previously established conventions.

The Matlab script *loco.m* performs all of the calculations and data processing to go from raw marker coordinates to analyzed data. A variety of formatted plots can be generated by the script and saved to disk in Adobe Acrobat PDF format. The variables used in *loco.m* are listed and detailed in Table XX and the source code with explanations follows afterwards.

Table 17: Variables used in *loc.m*

data	Matrix containing data loaded from *data.txt*
dat.x1	Reference marker *x* coordinates read from *data*
dat.y1	Reference marker y coordinates read from *data*
dat.x2	Deformed marker x coordinates read from *data*, corrected for translation from reference origins
dat.y2	Deformed marker y coordinates read from *data*, corrected for translation from reference origins
dat.u	*u* gradient calculated from X_1-x_1
dat.v	*v* gradient calculated from X_2-x_2
toaster1	Scaling factor used to determine whether the *v* gradient of some points cause them to be outliers
toaster2	Scaling factor used to determine whether the *u* gradient of some points cause them to be outliers
i	Iterative variable
p	Linear trend line fit to reference markers
angle	Angle calculated from *p* that line must be rotated to be horizontal
R	Rigid body rotation tensor
dat.base	Base matrix of *(x, y)* coordinates
dat.thick	Thickness of tissue calculated from maximum and minimum reference *y* coordinates
plotmesh	Delaunay triangle mesh generated from reference points
beta	Initial values used for nonlinear fitting routines
sr	Search radius of local fit read from file *sr.txt* for each specimen
k	Iterative variable
sstx	Sum of squares of total for *x* fit
ssty	Sum of squares of total for *y* fit
ssex	Sum of squares of errors for *x* fit
ssey	Sum of squares of errors for *y* fit
j	Iterative variable
dist	Distance map calculated for every point from every point
local.x	Reference marker *x* coordinates for the local system
local.y	Reference marker *y* coordinates for the local system
local.xd	Deformed marker *x* coordinates for the local system
local.yd	Deformed marker *y* coordinates for the local system
local.u	*u* gradient calculated from X_1-x_1 for the local system
local.v	*v* gradient calculated from X_2-x_2 for the local system
local.base	Base matrix of *(x, y)* coordinates in the local system
localxfit	Coefficients from nonlinear fit of deformed *x* coordinates
localyfit	Coefficients from nonlinear fit of deformed *y* coordinates
local.xdpred	Predicted deformed *x* positions using fit
local.ydpred	Predicted deformed *y* positions using fit
local.meanx	Mean of all local *x* coordinates
local.meany	Mean of all local *y* coordinates

Table 16 (continued).

ss	Iterative variable for determination of r^2
rsquaredx	r^2 value determined for *x* fit
rsquaredy	r^2 value determined for *y* fit
base	Base matrix of *(x, y)* coordinates
dat.f11	$\mathbf{F}_{11}$ determined from partial derivative of *x* fit
dat.f21	$\mathbf{F}_{21}$ determined from partial derivative of *y* fit
dat.f22	$\mathbf{F}_{22}$ determined from partial derivative of *y* fit
dat.f12	$\mathbf{F}_{12}$ determined from partial derivative of *x* fit
Xi	*X* coordinates obtained from generating a mesh of data range
Yi	*Y* coordinates obtained from generating a mesh of data range
dat.uGrid	*u* gradient expanded to grid made by *Xi, Yi*
dat.vGrid	*v* gradient expanded to grid made by *Xi, Yi*
m	Size in one dimension of gridded data
n	Size in one dimension of gridded data
newsize	Total number of elements in gridded data
dat.Xv	Vector form of *Xi*
dat.Yv	Vector form of *Yi*
dat.uGridv	Vector form of *dat.uGrid*
dat.vGridv	Vector form of *dat.vGrid*
dat.ufit	Coefficients of nonlinear fit of *u* gradients
ru	Residuals of nonlinear fit of *u* gradients
jacbu	Jacobian of nonlinear fit of *u* gradients
dat.upredv	Vector form of *dat.upred*
dat.upred	Predicted *u* gradients obtained from nonlinear fit
dat.vfit	Coefficients of nonlinear fit of *v* gradients
rv	Residuals of nonlinear fit of *v* gradients
jacbv	Jacobian of nonlinear fit of *v* gradients
dat.vpredv	Vector form of *dat.vpred*
dat.vpred	Predicted *v* gradients obtained from nonlinear fit
dat.ynorm	Reference *y* values normalized to range from 0 to 1
dat.F	Deformation gradient tensor
dat.Ft	Transpose of deformation gradient tensor
dat.C	Right Cauchy-Green deformation tensor
dat.U	Stretch tensor obtained via polar decomposition
dat.R	Rotation tensor obtained via polar decomposition
dat.E	Lagrangian strain tensor
dat.V	Eigenvectors of deformation gradient tensor
dat.d	Eigenvalues of deformation gradient tensor
dat.L1	
dat.L2	
temp	Temporary variable used for assigning values
dat.xpred	Deformed *x* coordinates predicted by applying **F**
dat.ypred	Deformed *y* coordinates predicted by applying **F**

Table 16 (continued).

dat.xrot	Rotated x coordinates predicted by applying $\mathbf{R}$
dat.yrot	Rotated y coordinates predicted by applying $\mathbf{R}$
dat.xrot2	Rotated x coordinates predicted by applying $\mathbf{R}^{-1}$
dat.yrot2	Rotated y coordinates predicted by applying $\mathbf{R}^{-1}$
dat.xstr	Stretched x coordinates predicted by applying $\mathbf{U}$
dat.ystr	Stretched y coordinates predicted by applying $\mathbf{U}$
dat.sinalpha12	Intermediate to calculation of shear angle alpha
dat.alpha	Measure of angular rotation caused by application of $\mathbf{F}$
dat.lambda1	Stretches in the X1 and X2 coordinate system directions
dat.deter	Determinant of deformation gradient tensor
dat.eigv	Eigenvectors of stretch tensor $\mathbf{U}$
dat.eigd	Eigenvalues of stretch tensor $\mathbf{U}$
dat.delta	Angular rotation of principal axes from coordinate axes
dat.lambda1p	X1 stretch in principal direction
dat.lambda2p	X2 stretch in principal direction
dat.caplamU1	Λ_1 taking into account U_{11} and U_{12}
dat.callamU2	Λ_2 taking into account U_{22} and U_{12}
dat.caplamF1	F_1 taking into account F_{11} and F_{12}
dat.caplamF2	F_2 taking into account $F_{22}$and F_{21}
dat.lambda1vsynorm	Linear trend line fit to U_{11} stretches and y normalized
dat.caplam1vsynorm	Linear trend line fit to Λ_1 stretches and y normalized
dat.ynormvscaplam1	Linear trend line fit to y normalized and Λ_1 stretches
capu1r2	r^2 value obtained from ynormvscaplam1 fit
intervals	y normalized expressed in 0.1 intervals
uoneline	Λ_1 values determined by ynormvscaplam1 along y normalized intervals
dat.ynormvscaplam2	Linear trend line fit to y normalized and Λ_2 stretches
capu2r2	r^2 values obtained from ynormvscaplam2 fit
utwoline	Λ_2 values determined by ynormvscaplam2 along y normalized intervals
dat.ynormvsalpha	Linear trend line fit to y normalized and shear angle α values
alphar2	r^2 value obtained from ynormvsalpha fit
alphaline	α values determined by ynormvsalpha along y normalized intervals
dat.naloc	Location of neutral axis in normalized y coordinates
fid	File identification handle
e11	$\mathbf{E}_{11}$ for output reasons
e12	$\mathbf{E}_{12}$ for output reasons
e22	$\mathbf{E}_{22}$ for output reasons
u11	$\mathbf{U}_{11}$ for output reasons
u12	$\mathbf{U}_{12}$ for output reasons
u22	$\mathbf{U}_{22}$ for output reasons
f11	$\mathbf{F}_{11}$ for output reasons

Table 16 (continued).

f12	$\mathbf{F}_{12}$ for output reasons
f21	$\mathbf{F}_{21}$ for output reasons
f22	$\mathbf{F}_{22}$ for output reasons
output	Matrix for organizing data to be written to disk
capU1capU2	Product of Λ_1 and Λ_2 for the determination of incompressibility
flag0	Flag for plot of reference/deformed positions and displacement vectors
flag1	Flag for plot of u and v displacements
flag2	Flag for plotting **E** against y normalized
flag3	Flag for plotting **F** against y normalized
flag4	Flag for plotting **U** against y normalized
flag5	Flag for plotting **R** against y normalized
flag6	Flag for plotting lambda values against y normalized
flag7	Flag for plotting 3D surfaces
flag8	Flag for plotting separate u and v displacements
flag9	Flag for plotting Lambda values against **U** and **F**
flag10	Flag for plotting composite page of important plots
dotsize	Specification for size of scatter points
pathstr	String containing current path
name	String containing current directory name
pwd	System variable containing current path
z	Temporary variable for determining a string within a string
first	First part of specimen label, namely specimen number
second	Second part of specimen label, namely testing time
suptitle	Concatenated specimen label
X	X coordinates obtained from generating a mesh of data range
Y	Y coordinates obtained from generating a mesh of data range
maxU11	Maximum U_{11} value
minU11	Minimum U_{11} value
maxU22	Maximum U_{22} value
minU22	Minimum U_{22} value
maxA	Maximum α value
mina	Minimum α value
maxE12	Maximum E_{12} value
minE12	Minimum E_{12} value
maxcU1	Maximum Λ_1 value
mincU1	Minimum Λ_1 value
maxcU2	Maximum Λ_2 value
mincU2	Minimum Λ_2 value
datarow	Vector used to organize data for screen output

```
% Thanh Lam
% March 25, 2004
% Transmural strain analysis program
clear;

%-------------------------------------------------------------------%
% Load data.txt generated by Transmural VI
%-------------------------------------------------------------------%
if exist('data.txt')
   load data.txt;

   dat.x1=data(:,1);
   dat.y1=1024-data(:,2);
   dat.x2=data(:,3)-(mean(data(:,3))-mean(data(:,1)));
   dat.y2=(1024-data(:,4))-((1024-mean(data(:,4)))-(1024-mean(data(:,2))));

   clear data;
else
   error('data.txt file not found');
end

if exist('ac.txt')
   dat.x1=1280-dat.x1;
   dat.y1=1024-dat.y1;
   dat.x2=1280-dat.x2;
   dat.y2=1024-dat.y2;
end

%-------------------------------------------------------------------%
% Calculate u and v gradients from x and y data
%-------------------------------------------------------------------%
dat.u=dat.x2-dat.x1;
dat.v=dat.y2-dat.y1;

%-------------------------------------------------------------------%
%   TOASTER ELIMINATES OUTLIERS
%-------------------------------------------------------------------%
if exist('notoast.txt')
   toaster1=20000;
   toaster2=20000;
else
   toaster1=mean(abs(dat.v))*2;
         for i=1:size(dat.x1)
      if abs(dat.v(i))>=toaster1
         dat.x1(i)=0;
         dat.y1(i)=0;
         dat.x2(i)=0;
         dat.y2(i)=0;
         dat.u(i)=0;
         dat.v(i)=0;
      end
         end

   toaster2=mean(abs(dat.u))*2;
   for i=1:size(dat.x1)
      if abs(dat.u(i))>=toaster2
```

```
            dat.x1(i)=0;
            dat.y1(i)=0;
            dat.x2(i)=0;
            dat.y2(i)=0;
            dat.u(i)=0;
            dat.v(i)=0;
        end
            end

dat.x1=nonzeros(dat.x1);
dat.y1=nonzeros(dat.y1);
dat.x2=nonzeros(dat.x2);
dat.y2=nonzeros(dat.y2);
dat.u=nonzeros(dat.u);
dat.v=nonzeros(dat.v);

end

clear toaster1 toaster2;

%--------------------------------------------------------------------%
%   DATA FITTING
%--------------------------------------------------------------------%

p=polyfit(dat.x1,dat.y1,1);                         % Rotate data
angle=atan(p(1));                                   % Rotate data
R=[cos(angle), -sin(angle);sin(angle),cos(angle)];      % Rotate data
dat.base=[dat.x1,dat.y1]*R;                             % Rotate data
dat.x1=dat.base(:,1);                               % Rotate data
dat.y1=dat.base(:,2);                               % Rotate data
clear dat.base;                                     % Rotate data
dat.base=[dat.x2,dat.y2]*R;                             % Rotate data
dat.x2=dat.base(:,1);                               % Rotate data
dat.y2=dat.base(:,2);                               % Rotate data
clear dat.base;                                     % Rotate data

dat.thick=max(dat.y1)-min(dat.y1);              % "thickness" of tissue
plotmesh=delaunay(dat.x1,dat.y1);
beta=[1,1,1,1,1,1,1,1]';            % Initial values for nonlinear fits
sr=load('sr.txt');                  % search radius for local fit

%--------------------------------------------------------------------%
% Local fit code
%--------------------------------------------------------------------%
% sstx, ssty: sum of squares total for x and y fits
% ssex, ssey: sum of squares error for x and y fits
% A distance table is calculated for every point from every point, those
% points that are within the search radius are included for the local fit
% (local.base).  Fit to the form in fit.m.  Points are predicted using the
% fits to determine the SSE for the Rsquared calculation of each fit.
%--------------------------------------------------------------------%
for i=1:length(dat.x1)
   k=1;
   sstx=0;
   ssty=0;
   ssex=0;
```

```
   ssey=0;
   for j=1:length(dat.x1)
      dist=sqrt((dat.x1(i)-dat.x1(j))^2+(dat.y1(i)-dat.y1(j))^2);
      if dist < sr
         local.x(k,:)=dat.x1(j);
         local.y(k,:)=dat.y1(j);
         local.xd(k,:)=dat.x2(j);
         local.yd(k,:)=dat.y2(j);
         local.u(k,:)=dat.u(j);
         local.v(k,:)=dat.v(j);
         k=k+1;
      end
   end
   local.base=[local.x,local.y];

   localxfit(:,i)=nlinfit(local.base,local.xd,@fit,beta);    % X, Y fit
   localyfit(:,i)=nlinfit(local.base,local.yd,@fit,beta);    % X, Y fit
   local.xdpred=fit(localxfit,local.base);                % X, Y fit
   local.ydpred=fit(localyfit,local.base);                % X, Y fit
   local.meanx=mean(local.x);                             % X, Y fit
   local.meany=mean(local.y);                             % X, Y fit
   for ss=1:length(local.x)                            % X, Y fit
      sstx=sstx+(local.xd(ss)-local.meanx)^2;                   % X, Y fit
      ssty=ssty+(local.yd(ss)-local.meany)^2;                   % X, Y fit
      ssex=ssex+(local.xd(ss)-local.xdpred(ss))^2;                % X, Y fit
      ssey=ssey+(local.yd(ss)-local.ydpred(ss))^2;                % X, Y fit
   end                                          % X, Y fit

%     localxfit(:,i)=nlinfit(local.base,local.u,@fit,beta);    % u, v fit
%     localyfit(:,i)=nlinfit(local.base,local.v,@fit,beta);    % u, v fit
%     local.upred=fit(localxfit,local.base);                % u, v fit
%     local.vpred=fit(localyfit,local.base);                % u, v fit
%     local.meanu=mean(local.u);                              % u, v fit
%     local.meanv=mean(local.v);                              % u, v fit
%     for ss=1:length(local.x)                           % u, v fit
%        sstx=sstx+(local.u(ss)-local.meanu)^2;                   % u, v fit
%        ssty=ssty+(local.v(ss)-local.meanv)^2;                   % u, v fit
%        ssex=ssex+(local.u(ss)-local.upred(ss))^2;                 % u, v fit
%        ssey=ssey+(local.v(ss)-local.vpred(ss))^2;                 % u, v fit
%     end                                         % u, v fit

   rsquaredx(i,:)=1-ssex/sstx;
   rsquaredy(i,:)=1-ssey/ssty;
   clear local;
end

base=[dat.x1,dat.y1];

dat.f11=xfit(localxfit,base);
dat.f21=xfit(localyfit,base);
dat.f22=yfit(localyfit,base);
dat.f12=yfit(localxfit,base);

warning off MATLAB:griddata:DuplicateDataPoints;

% Meshes x and y coordinates and then generates denser grid of data for
```

```
% given data set, reshapes data output to a point coordinate vector
[Xi,Yi]=meshgrid(floor(min(dat.x1)/100)*100-100:10:floor(max(dat.x1)/100)*100+100,...
   floor(min(dat.y1)/100)*100-100:10:floor(max(dat.y1)/100)*100+100); % For testing
dat.uGrid=griddata(dat.x1,dat.y1,dat.u,Xi,Yi,'linear');
dat.vGrid=griddata(dat.x1,dat.y1,dat.v,Xi,Yi,'linear');
[m,n]=size(dat.uGrid); % Determine number of points and length of vector
newsize=m*n;
dat.Xv=reshape(Xi,[newsize 1]);
dat.Yv=reshape(Yi,[newsize 1]);
dat.uGridv=reshape(dat.uGrid,[newsize 1]);
dat.vGridv=reshape(dat.vGrid,[newsize 1]);
base=[dat.Xv,dat.Yv];

% % Performs nonlinear fit of u griddata and obtain coefficients
[dat.ufit,ru,jacbu]=nlinfit(base,dat.uGridv,@fit,beta);
dat.upredv=fit(dat.ufit,base);
dat.upred=reshape(dat.upredv,[m n]);

% % Performs nonlinear fit of v griddata and obtain coefficients
[dat.vfit,rv,jacbv]=nlinfit(base,dat.vGridv,@fit,beta);
dat.vpredv=fit(dat.vfit,base);
dat.vpred=reshape(dat.vpredv,[m n]);

%--------------------------------------------------------------------%
%   CALCULATIONS
%--------------------------------------------------------------------%
% % Reset base point coordinate vector to data points
base=[dat.x1,dat.y1];
dat.ynorm=(dat.y1-min(dat.y1))/dat.thick;

for i=1:size(dat.f11,1)
   dat.F(:,:,i)=[dat.f11(i),dat.f12(i);dat.f21(i),dat.f22(i)]; % F tensor
   dat.Ft(:,:,i)=[dat.f11(i),dat.f12(i);dat.f21(i),dat.f22(i)]'; % F transpose tensor
   dat.C(:,:,i)=fix((dat.Ft(:,:,i)*dat.F(:,:,i))*10000)/10000; % C tensor
   dat.U(:,:,i)=sqrtm(dat.C(:,:,i)); % U tensor
   dat.R(:,:,i)=dat.F(:,:,i)*inv(dat.U(:,:,i)); % R tensor
   dat.E(:,:,i)=0.5*(dat.C(:,:,i)-eye(2)); % E tensor
   [dat.V(:,:,i),dat.d(:,:,i)]=eig(dat.F(:,:,i));
   dat.L1(i)=sqrt(2*dat.V(1,1,i)+1);
   dat.L2(i)=sqrt(2*dat.V(2,2,i)+1);
   temp=dat.F(:,:,i)*[dat.x1(i);dat.y1(i)];
   dat.xpred(i)=temp(1); % x coordinates predicted from using F
   dat.ypred(i)=temp(2); % y coordinates predicted from using F
   temp=dat.R(:,:,i)*[dat.x1(i);dat.y1(i)];
   dat.xrot(i)=temp(1); % x coordinates rotated by R
   dat.yrot(i)=temp(2); % y coordinates rotated by R
   temp=inv(dat.R(:,:,i))*[dat.x1(i);dat.y1(i)];
   dat.xrot2(i)=temp(1); % x coordinates rotated by inverse R
   dat.yrot2(i)=temp(2); % y coordinates rotated by inverse R
   temp=dat.U(:,:,i)*[dat.x1(i);dat.y1(i)];
   dat.xstr(i)=temp(1); % x coordinates stretched by U
   dat.ystr(i)=temp(2); % y coordinates stretched by U
   dat.sinalpha12(i)=(2*dat.E(1,2,i))./(sqrt(1+2*dat.E(1,1,i)).*sqrt(1+2*dat.E(2,2,i)));
   dat.alpha(i)=(180/pi)*asin(dat.sinalpha12(i));
   dat.lambda1(i)=dat.U(1,1,i);
   dat.deter(i)=det(dat.F(:,:,i));
```

```
   [dat.eigv(:,:,i),dat.eigd(:,:,i)]=eig(dat.U(:,:,i));
   dat.delta(i)=acos(dot(abs(dat.eigv(:,1,i)),[1;0]))*180/pi;
   dat.lambda1p(i)=dat.eigd(1,1,i);
   dat.lambda2p(i)=dat.eigd(2,2,i);
   dat.caplamU1(i)=sqrt(dat.U(1,1,i)^2+dat.U(1,2,i)^2);
   dat.caplamU2(i)=sqrt(dat.U(2,2,i)^2+dat.U(1,2,i)^2);
   dat.caplamF1(i)=sqrt(dat.F(1,1,i)^2+dat.F(1,2,i)^2);
   dat.caplamF2(i)=sqrt(dat.F(2,2,i)^2+dat.F(2,1,i)^2);
end

% Find normalized location of neutral axis
% dat.lambda1vsynorm=polyfit(dat.lambda1',dat.ynorm,1);
% dat.caplam1vsynorm=polyfit(dat.caplamU1',dat.ynorm,1);
% dat.naloc=polyval(dat.caplam1vsynorm,1);
dat.ynormvscaplam1=polyfit(dat.ynorm,dat.caplamU1',1);
capu1r2=r2linear(dat.ynormvscaplam1,dat.ynorm,dat.caplamU1');
intervals=[0,0.1,0.2,0.3,0.4,0.5,0.6,0.7,0.8,0.9,1]';
uoneline=polyval(dat.ynormvscaplam1,intervals);
dat.naloc=(1-dat.ynormvscaplam1(2))/dat.ynormvscaplam1(1);

dat.ynormvscaplam2=polyfit(dat.ynorm,dat.caplamU2',1);
capu2r2=r2linear(dat.ynormvscaplam2,dat.ynorm,dat.caplamU2');
utwoline=polyval(dat.ynormvscaplam2,intervals);

dat.ynormvsalpha=polyfit(dat.ynorm,dat.alpha',1);
alphar2=r2linear(dat.ynormvsalpha,dat.ynorm,dat.alpha');
alphaline=polyval(dat.ynormvsalpha,intervals);

%----------------------------------------------------------------------%
% Output calculated values to text file crunched.txt
%----------------------------------------------------------------------%
fid=fopen('crunched.txt','w');
fprintf(fid,'x1\tx2\tX1\tX2\tU\tV\tYNORM\tALPHA\tE11\tE12\tE22\tU11\tU12\tU22\tF11\tF12\tF21\tF22\tr2X
\tr2Y\n');

e11(:,1)=dat.E(1,1,:);
e12(:,1)=dat.E(1,2,:);
e22(:,1)=dat.E(2,2,:);
u11(:,1)=dat.U(1,1,:);
u12(:,1)=dat.U(1,2,:);
u22(:,1)=dat.U(2,2,:);
f11(:,1)=dat.F(1,1,:);
f12(:,1)=dat.F(1,2,:);
f21(:,1)=dat.F(2,1,:);
f22(:,1)=dat.F(2,2,:);

output=[dat.x1, dat.y1, dat.x2, dat.y2, dat.u, dat.v, dat.ynorm, dat.alpha', ...
      e11, e12, e22, ...
      u11, u12, u22, ...
      f11, f12, f21, f22, rsquaredx, rsquaredy]';

fprintf(fid,'%f\t%f\t%f\t%f\t%f\t%f\t%f\t%f\t%f\t%f\t%f\t%f\t%f\t%f\t%f\t%f\t%f\t%f\t%f\t%f\n',output);
fclose(fid);
capU1capU2=mean(dat.caplamU1'.*dat.caplamU2');
clear output e11 e12 e22 u11 u12 u22 f11 f12 f21 f22;
```

```
%---------------------------------------------------------------%
%        PLOTTING ROUTINES
% ------------------------------------------------------------ %
flag0=0;             % reference/deformed points and vector plots %
flag1=0;                                % uv displacements %
flag2=0;                                      % E tensor %
flag3=0;                                      % F tensor %
flag4=0;                                      % U tensor %
flag5=0;                                      % R tensor %
flag6=0;                                       % lambdas %
flag7=0;                                      % 3D plots %
flag8=0;                      % separate u and v displacements %
flag9=0;                         % cap lambdas versus U and F %
flag10=1;                                     % composite %
dotsize=15;

% Determine the name of the sample specimen from the current directory
% Used to name the composite graph page
[pathstr,name]=fileparts(pwd);      % pwd is a system variable of the current path
z=strfind(pathstr,'\');
first=upper(pathstr(z(length(z))+1:length(pathstr)));   % specimen number
z=strfind(name,' ');
second=name(z(length(z)):length(name));                 % test time
suptitle=strcat(first,second);

if flag0
          figure;
          set(gcf,'PaperPosition',[0.25 0.25 8 10.5]);
          subplot(3,2,1);
          scatter(dat.x1,dat.y1,'filled');
          hold on;
          scatter(dat.x2,dat.y2);
          title('Reference and Deformed Points');
          xlabel('X-coordinate');     ylabel('Y-coordinate');
          subplot(3,2,2);
          quiver(dat.x1,dat.y1,dat.u,dat.v);
          title('Displacement vectors');
          xlabel('X-coordinate');     ylabel('Y-coordinate');
          subplot(3,2,3);
          quiver(dat.x1,dat.y1,dat.xstr'-dat.x1,dat.ystr'-dat.y1);
          xlabel('x coord');      ylabel('y coord');
          title('U only gradient');
          subplot(3,2,4);
          quiver(dat.x1,dat.y1,fix((dat.xrot'-dat.x1)*10000)/10000,fix((dat.yrot'-dat.y1)*10000)/10000);
          xlabel('x coord');      ylabel('y coord');
          title('R only gradient');
          subplot(3,2,5);
          scatter(dat.x1,dat.y1,'filled');
          hold on;
          scatter(dat.xpred-(mean(dat.xpred)-mean(dat.x1)),dat.ypred-(mean(dat.ypred)-mean(dat.y1)));
          xlabel('x coord');      ylabel('y coord');
          title('Reference and Predicted Points');
          subplot(3,2,6);
          quiver(dat.x1,dat.y1,dat.xpred'-dat.x1,dat.ypred'-dat.y1);
          quiver(dat.x1,dat.y1,dat.xpred'-(mean(dat.xpred)-mean(dat.x1))-dat.x1,...
      dat.ypred'-(mean(dat.ypred)-mean(dat.y1))-dat.y1);
```

```
            xlabel('x coord');      ylabel('y coord');
            title('Predicted Displacement Vectors');
end

if flag1
    figure;
    colormap('gray');
    set(gcf,'PaperPosition',[0.25 0.25 8 10.5]);
    subplot(3,2,1);
    scatter(dat.ynorm,dat.u,dotsize,dat.x1,'filled');
    xlabel('y normalized');    ylabel('u displacement');    grid;
    subplot(3,2,2);
    scatter(dat.ynorm,dat.v,dotsize,dat.x1,'filled');
    xlabel('y normalized');    ylabel('v displacement');    grid;
    subplot(3,2,3);
    scatter(dat.ynorm,dat.dudx,dotsize,dat.x1,'filled');
    xlabel('y normalized');    ylabel('ux');    grid;
    subplot(3,2,4);
    scatter(dat.ynorm,dat.dudy,dotsize,dat.x1,'filled');
    xlabel('y normalized');    ylabel('uy');    grid;
    subplot(3,2,5);
    scatter(dat.ynorm,dat.dvdx,dotsize,dat.x1,'filled');
    xlabel('y normalized');    ylabel('vx');    grid;
    subplot(3,2,6);
    scatter(dat.ynorm,dat.dvdy,dotsize,dat.x1,'filled');
    xlabel('y normalized');    ylabel('vy');    grid;
end

if flag2
    figure;
    colormap('gray');
    set(gcf,'PaperPosition',[0.25 0.25 8 10.5]);
    subplot(3,2,1);
    scatter(dat.x1,dat.E(1,1,:),dotsize,dat.y1,'filled');
    xlabel('x1');    ylabel('E11');    grid;
    subplot(3,2,2);
    scatter(dat.ynorm,dat.E(1,1,:),dotsize,dat.x1,'filled');
    xlabel('y normalized');    ylabel('E11');    grid;
    subplot(3,2,3);
    scatter(dat.x1,dat.E(1,2,:),dotsize,dat.y1,'filled');
    xlabel('x1');    ylabel('E12');    grid;
    subplot(3,2,4);
    scatter(dat.ynorm,dat.E(1,2,:),dotsize,dat.x1,'filled');
    xlabel('y normalized');    ylabel('E12');    grid;
    subplot(3,2,5);
    scatter(dat.x1,dat.E(2,2,:),dotsize,dat.y1,'filled');
    xlabel('x1');    ylabel('E22');    grid;
    subplot(3,2,6);
    scatter(dat.ynorm,dat.E(2,2,:),dotsize,dat.y1,'filled');
    xlabel('y normalized');    ylabel('E22');    grid;
end

if flag3
    figure;
    set(gcf,'PaperPosition',[0.25 0.25 8 10.5]);
    subplot(4,2,1);
```

```
    scatter(dat.x1,dat.F(1,1,:));
    xlabel('x1');    ylabel('F11');    grid;
    subplot(4,2,2);
    scatter(dat.y1,dat.F(1,1,:));
    xlabel('y1');    ylabel('F11');    grid;
    subplot(4,2,3);
    scatter(dat.x1,dat.F(1,2,:));
    xlabel('x1');    ylabel('F12');    grid;
    subplot(4,2,4);
    scatter(dat.y1,dat.F(1,2,:));
    xlabel('y1');    ylabel('F12');    grid;
    subplot(4,2,5);
    scatter(dat.x1,dat.F(2,1,:));
    xlabel('x1');    ylabel('F21');    grid;
    subplot(4,2,6);
    scatter(dat.y1,dat.F(2,1,:));
    xlabel('y1');    ylabel('F21');    grid;
    subplot(4,2,7);
    scatter(dat.x1,dat.F(2,2,:));
    xlabel('x1');    ylabel('F22');    grid;
    subplot(4,2,8);
    scatter(dat.y1,dat.F(2,2,:));
    xlabel('y1');    ylabel('F22');    grid;
end

if flag4
    figure;
    set(gcf,'PaperPosition',[0.25 0.25 8 10.5]);
    subplot(4,2,1);
    scatter(dat.x1,dat.U(1,1,:));
    xlabel('x1');    ylabel('U11');    grid;
    subplot(4,2,2);
    scatter(dat.y1,dat.U(1,1,:));
    xlabel('y1');    ylabel('U11');    grid;
    subplot(4,2,3);
    scatter(dat.x1,dat.U(1,2,:));
    xlabel('x1');    ylabel('U12');    grid;
    subplot(4,2,4);
    scatter(dat.y1,dat.U(1,2,:));
    xlabel('y1');    ylabel('U12');    grid;
    subplot(4,2,5);
    scatter(dat.x1,dat.U(2,1,:));
    xlabel('x1');    ylabel('U21');    grid;
    subplot(4,2,6);
    scatter(dat.y1,dat.U(2,1,:));
    xlabel('y1');    ylabel('U21');    grid;
    subplot(4,2,7);
    scatter(dat.x1,dat.U(2,2,:));
    xlabel('x1');    ylabel('U22');    grid;
    subplot(4,2,8);
    scatter(dat.y1,dat.U(2,2,:));
    xlabel('y1');    ylabel('U22');    grid;
end

if flag5
    figure;
```

```
    set(gcf,'PaperPosition',[0.25 0.25 8 10.5]);
    subplot(4,2,1);
    scatter(dat.x1,dat.R(1,1,:));
    xlabel('x1');    ylabel('R11');    grid;
    subplot(4,2,2);
    scatter(dat.y1,dat.R(1,1,:));
    xlabel('y1');    ylabel('R11');    grid;
    subplot(4,2,3);
    scatter(dat.x1,dat.R(1,2,:));
    xlabel('x1');    ylabel('R12');    grid;
    subplot(4,2,4);
    scatter(dat.y1,dat.R(1,2,:));
    xlabel('y1');    ylabel('R12');    grid;
    subplot(4,2,5);
    scatter(dat.x1,dat.R(2,1,:));
    xlabel('x1');    ylabel('R21');    grid;
    subplot(4,2,6);
    scatter(dat.y1,dat.R(2,1,:));
    xlabel('y1');    ylabel('R21');    grid;
    subplot(4,2,7);
    scatter(dat.x1,dat.R(2,2,:));
    xlabel('x1');    ylabel('R22');    grid;
    subplot(4,2,8);
    scatter(dat.y1,dat.R(2,2,:));
    xlabel('y1');    ylabel('R22');    grid;
end

if flag6
    figure;
    set(gcf,'PaperPosition',[0.25 0.25 8 10.5]);
    subplot(2,1,1);
    scatter(dat.ynorm,dat.U(1,1,:));
    xlabel('ynorm');    ylabel('lambda1');    grid;
    subplot(2,1,2);
    scatter(dat.ynorm,dat.U(2,2,:));
    xlabel('ynorm');    ylabel('lambda2');    grid;
end

[X,Y]=meshgrid(dat.x1,dat.y1);

if flag7
    figure;
    set(gcf,'PaperPosition',[0.25 2.5 8 6]);
    subplot(2,2,1);
    scatter3(dat.x1,dat.y1,dat.u,'filled','k');
    hold on;
    surfc(Xi,Yi,dat.upred,'EdgeAlpha',0.1);
    colormap(summer);
    title('x deformed');
    xlabel('x coord');    ylabel('y coord');
    subplot(2,2,2);
    scatter3(dat.x1,dat.y1,dat.v,'filled','k');
    hold on;
    surfc(Xi,Yi,dat.vpred,'EdgeAlpha',0.1);
    title('y deformed');
    xlabel('x coord');    ylabel('y coord');
```

```
   subplot(2,2,3);
   trisurf(plotmesh,dat.x1,dat.y1,dat.E(1,2,:));
   title('E12');
   xlabel('x coord');    ylabel('y coord');
   subplot(2,2,4);
   trisurf(plotmesh,dat.x1,dat.y1,dat.E(2,2,:));
   title('E22');
   xlabel('x coord');    ylabel('y coord');
end

if flag8
   figure;
   colormap('gray');
   set(gcf,'PaperPosition',[0.25 0.25 8 10.5]);
   subplot(2,1,1);
        quiver(dat.x1,dat.y1,dat.u,zeros(size(dat.u)));
        title('u displacements ONLY');
        xlabel('X-coordinate');     ylabel('Y-coordinate');
   subplot(2,1,2);
        quiver(dat.x1,dat.y1,zeros(size(dat.v)),dat.v);
        title('v displacements ONLY');
        xlabel('X-coordinate');     ylabel('Y-coordinate');

end

if flag9
   figure;
   set(gcf,'PaperPosition',[0.25 0.25 8 10.5]);
   subplot(2,2,1);
   scatter(dat.U(1,1,:),dat.caplamU1);
   xlabel('U11');   ylabel('CapLamU1');    grid;
   subplot(2,2,2);
   scatter(dat.U(2,2,:),dat.caplamU2);
   xlabel('U22');   ylabel('CapLamU2');    grid;
   subplot(2,2,3);
   scatter(dat.U(1,1,:),dat.caplamF1);
   xlabel('U11');   ylabel('CapLamF1');    grid;
   subplot(2,2,4);
   scatter(dat.U(2,2,:),dat.caplamF2);
   xlabel('U22');   ylabel('CapLamF2');    grid;
end

if flag10
        figure;
        set(gcf,'PaperPosition',[0.25 0.25 8 10.5]);
        subplot(3,2,1);
%       scatter(dat.ynorm,dat.U(1,1,:),'filled','k');
%       title('U11 vs Y normalized');
        scatter(dat.ynorm,dat.caplamU1','filled','k');
   hold on; plot(intervals,uoneline); hold off;
        title('capLambda1 vs Y normalized');
%       xlabel('Y normalized');     ylabel('U11');  grid;
   xlabel('Y normalized');     ylabel('capLambda1');  grid;
        subplot(3,2,2);
        scatter(dat.ynorm,dat.U(1,2,:),'filled','k');
        title('U12 vs Y normalized');
```

```
          xlabel('Y normalized');     ylabel('U12');  grid;
          subplot(3,2,3);
%         scatter(dat.ynorm,dat.U(2,2,:),'filled','k');
%         title('U22 vs Y normalized');
          scatter(dat.ynorm,dat.caplamU2','filled','k');
   hold on; plot(intervals,utwoline); hold off;
          title('capLambda2 vs Y normalized');
%         xlabel('Y normalized');     ylabel('U22');  grid;
          xlabel('Y normalized');     ylabel('capLambda2');  grid;
          subplot(3,2,4);
   scatter(dat.ynorm,dat.alpha,'filled','k');
   hold on; plot(intervals,alphaline); hold off;
   title('alpha (degrees)');
          xlabel('Y normalized');      ylabel('alpha');  grid;
          subplot(3,2,5);
   scatter(rsquaredx,rsquaredy,'filled','k');
   axis equal;
   title('R-squared in x vs R-squared in y');
          xlabel('R-squared in x');      ylabel('R-squared in y');  grid;
          subplot(3,2,6);
   scatter(dat.ynorm,dat.E(1,2,:),'filled','k');
          title('E12 vs Y normalized');
   xlabel('Y normalized');      ylabel('E12');  grid;
   ax=axes('Units','Normal','Position',[.1 .1 .85 .85],'Visible','off');
   set(get(ax,'Title'),'Visible','on')
   title(suptitle);       % Setup axes to place a supertitle
   print -dpdf composite.pdf;      % Output figure to a pdf file
%     close;
end

save dat.mat dat;

%---------------------------------------------------------------------%
% Debugging plots
%---------------------------------------------------------------------%
% figure; scatter(dat.x2,dat.y2,'filled'); hold on; scatter(dat.x1+dat.up,dat.y1+dat.vp);
% figure; scatter(dat.x2,dat.y2,'filled'); hold on; scatter(dat.xpred,dat.ypred);
% figure; scatter(dat.x1,ref.botpts); hold on; scatter(dat.x1,ref.toppts);
%     scatter(dat.x1,dat.y1+ref.botpts);
% figure; trisurf(plotmesh,datbak.x1,datbak.y1,zeros(size(datbak.x1)));
% figure; trisurf(plotmesh,dat.x1,dat.y1,zeros(size(dat.x1)));
% hold on;
% scatter(tri.x1,tri.y1);
% quiver(tri.x1,tri.y1,tri.xpred'-tri.x1,tri.ypred'-tri.y1,'k');
% view(0,90);
% daspect([1 1 1]);
% scatter(tri.x2,tri.y2,'k');
% % triplot(plotmesh,datbak.x2,datbak.y2);
% triplot(plotmesh,dat.x2,dat.y2,'k');
maxU11=max(dat.U(1,1,:));
minU11=min(dat.U(1,1,:));
maxU22=max(dat.U(2,2,:));
minU22=min(dat.U(2,2,:));
maxA=max(dat.alpha);
minA=min(dat.alpha);
maxE12=max(dat.E(1,2,:));
```

```
minE12=min(dat.E(1,2,:));
maxcU1=max(dat.caplamU1);
mincU1=min(dat.caplamU1);
maxcU2=max(dat.caplamU2);
mincU2=min(dat.caplamU2);
% disp('max stretch:');
% disp(maxU11);
% disp('min stretch:');
% disp(minU11);
% disp('neutral axis location:');
% disp(dat.naloc);

%-------------------------------------------------------------------%
% Save pertinent data to text file in root directory
%-------------------------------------------------------------------%
datarow=[maxU11,minU11,maxU22,minU22,dat.naloc,mean(rsquaredx),mean(rsquaredy),sr,capU1capU
2,i...
      maxA,minA,maxE12,minE12,maxcU1,mincU1,maxcU2,mincU2];
% fid=fopen('..\..\stats.txt','a');
% fprintf(fid,'%s\t',suptitle);
% fprintf(fid,'%f\t%f\t%f\t%f\t%f\t%f\t%f\t%f\t%f\t%f\t%f\t%f\t%f\t%f\t%f\t%f\t%f',datarow);
% fprintf(fid,'%f\t%f\t%f\t%f\t%f\t%f\t%f\t%f\t%f\t%f\t%f',capu1r2,uoneline');
% fprintf(fid,'\t%f\t%f\t%f\t%f\t%f\t%f\t%f\t%f\t%f\t%f\t%f',capu2r2,utwoline');
% fprintf(fid,'\t%f\t%f\t%f\t%f\t%f\t%f\t%f\t%f\t%f\t%f\t%f\r',alphar2,alphaline');
% fclose(fid);
%-------------------------------------------------------------------%

clear maxU11 minU11 maxU22 minU22 maxA minA maxE12 minE12 maxcU1 mincU1 maxcU2 mincU2;
% figure;
% subplot(2,1,1);
% scatter(dat.x1,dat.delta);
% xlabel('x1 coord');
% ylabel('delta princip rotation degrees');
% grid;
%-------------------------------------------------------------------%
```

REFERENCES

1. AHA, *Heart Disease and Stroke Statistics - 2003 Update*. 2002, American Heart Association: Dallas, Tx.

2. Schoen, F.J., *Pathology of heart valve substitution with mechanical and tissue prostheses*, in *Cardiovascular Pathology*, M.D. Silver, A.I. Gotlieb, and F.J. Schoen, Editors. 2001, Livingstone: New York.

3. Dalshaug, G.B., C.A. Caldarone, and P. Camp, *Aortic Valve Disease and the Ross Operation.* eMedicine, 2003.

4. Alphonso, N., et al., *Midterm Results of the Ross Procedure*. European Journal of Cardio-thoracic Surgery. Vol. 25. 2004. 925-30.

5. Berne, R.M. and M.N. Levy, *Physiology*. 4 ed. 1998, Saint Louis: Mosby.

6. Netter, F.H., *Atlas of Human Anatomy*. 2nd ed. 1997, East Hanover: Navartis. 525.

7. Thubrikar, M., *The Aortic Valve*. 1990, Boca Raton: CRC. 221.

8. Schoen, F., *Aortic valve structure-function correlations: Role of elastic fibers no longer a stretch of the imagination.* Journal of Heart Valve Disease, 1997. **6**: p. 1-6.

9. Alberts, B., et al., *Molecular Biology of the Cell*. 3rd ed. 1994, New York: Garland Publishing.

10. Voet and Voet, *Biochemistry*. 1995, John Wiley and Sons.

11. Vesely, I., *The role of elastin in aortic valve mechanics.* Journal of Biomechanics, 1998. **31**(2): p. 115-123.

12. Schoen, F. and R. Levy, *Tissue heart valves: Current challenges and future research perspectives.* Journal of Biomedical Materials Research, 1999. **47**: p. 439-465.

13. Lovekamp, J. and N. Vyavahare, *Periodate-mediated glycosaminoglycan stabilization in bioprosthetic heart valves.* J Biomed Mater Res, 2001. **56**(4): p. 478-86.

14. Sacks, M., et al., *Loss of flexural rigidity in bioprosthetic heart valves with fatigue: New findings and the relation to collagen damage.* Journal of Biomechanics, submitted.

15. Broom, N.D., *The observation of collagen and elastin structures in wet whole mounts of pulmonary and aortic leaflets.* J Thorac Cardiovasc Surg, 1978. **75**(1): p. 121-30.

16. David, H., et al., *The pulmonary valve. Is it mechanically suitable for use as an aortic valve replacement?* Asaio J, 1994. **40**(2): p. 206-12.

17. Christie, G.W. and B.G. Barratt-Boyes, *Mechanical properties of porcine pulmonary valve leaflets: how do they differ from aortic leaflets?* Ann Thorac Surg, 1995. **60**(2 Suppl): p. S195-9.

18. Sacks, M.S., *Biaxial mechanical evaluation of planar biological materials.* Journal of Elasticity, 2000. **61**: p. 199-246.

19. Fung, Y.C., *Biomechanics: Mechanical Properties of Living Tissues*. 2nd ed. 1993, New York: Springer Verlag. 568.

20. Vesely, I. and R. Noseworthy, *Micromechanics of the fibrosa and the ventricularis in aortic valve leaflets.* Journal of Biomechanics, 1992. **25**(1): p. 101-113.

21. Thubrikar, M.J., et al., *Stress analysis of porcine bioprosthetic heart valves in vivo.* J Biomed Mater Res, 1982. **16**(6): p. 811-26.

22. Vesely, I. and D.R. Boughner, *A multipurpose tissue bending machine.* Journal of Biomechanics, 1985. **18**(7): p. 511-513.

23. Talman, E. and D. Boughner, *Internal shear properties of fresh aortic valve cusps: Implications for normal valve function.* Journal of heart valve disease, 1996. **5**: p. 152-159.

24. Merryman, W.D., et al., *The effects of cellular contraction on aortic valve leaflet flexural stiffness.* Journal of Biomechanics, in-press.

25. Mirnajafi, A., et al., *The effects of collagen fiber orientation on the flexural properties of pericardial heterograft biomaterials.* Biomaterials, 2005. **26**(7): p. 795-804.

26. Gloeckner, D.C., K.L. Billiar, and M.S. Sacks, *Effects of mechanical fatigue on the bending properties of the porcine bioprosthetic heart valve.* Asaio J, 1999. **45**(1): p. 59-63.

27. Engelmayr, G.C., Jr., et al., *The independent role of cyclic flexure in the early in vitro development of an engineered heart valve tissue.* Biomaterials, 2005. **26**(2): p. 175-87.

28. Engelmayr, G.C., et al., *A novel bioreactor for the dynamic flexural stimulation of tissue engineered heart valve biomaterials.* Biomaterials, 2003. **24**(14): p. 2523-32.

29. Sacks, M. and K. Billiar, *Chapter 3: Biaxial Mechanical Behavior of Bioprosthetic Heart Cusps Subjected to Accelerated Testing*, in *Advances in Anticalcific and Antidegenerative Treatment of Heart Valve Bioprostheses*, S. Gabbay and R. Frater, Editors. 1997, Silent Partners: Austin.

30. Billiar, K.L. and M.S. Sacks, *Biaxial mechanical properties of the natural and glutaraldehyde treated aortic valve cusp--Part I: Experimental results.* Journal of Biomechanical Engineering, 2000. **122**(1): p. 23-30.

31. Billiar, K.L. and M.S. Sacks, *Biaxial mechanical properties of the native and glutaraldehyde-treated aortic valve cusp: Part II--A structural constitutive model.* Journal of Biomechanical Engineering, 2000. **122**(4): p. 327-35.

32. Sacks, M.S., D.B. Smith, and E.D. Hiester, *The aortic valve microstructure: effects of transvalvular pressure.* Journal of Biomedical Materials Research, 1998. **41**(1): p. 131-41.

33. van Doorn, C., *The Unnatural History of Tetralogy of Fallot: Surgical Repair is not as Definitve as Previously Thought.* Heart, 2002. **88**: p. 447-448.

34. Olivier, C., *Rheumatic Fever - Is it still a Problem?* Journal of Antimicrobial Chemotherapy, 2000. **45**: p. 13-21.

35. Millar, B.C. and J.E. Moore, *Emerging Issues in Infective Endocarditis.* Emerging Infectious Diseases, 2004. **10**(6): p. 1110-1116.

36. Pelech, A.N. and S.R. Neish, *Sudden Death in Congenital Heart Disease.* Pediatric Clinics of North America, 2004. **51**(5): p. 1257-71.

37. Nishimura, R.A., *Cardiology patient pages. Aortic valve disease.* Circulation, 2002. **106**(7): p. 770-2.

38. Simon, P., et al., *Growth of the pulmonary autograft after the Ross operation in childhood.* European Journal of Cardio-thoracic Surgery, 2000. **19**(2): p. 118-121.

39. Ohye, R.G., et al., *The Ross/Konno Procedure in Neonates and Infants: Intermediate-Term Survival and Autograft Function.* Annals of Thoracic Surgery, 2001. **72**(3): p. 823-830.

40. Al-Halees, Z., et al., *The Ross Procedure is the Procedure of Choice for Congenital Aortic Valve Disease.* Journal of Cardiothoracic Surgery, 2002. **123**(3): p. 437-441.

41. Elkins, R.C., et al., *Pulmonary Autograft in Children: Realized Growth Potential.* Annals of Thoracic Surgery, 1994. **57**: p. 1387-1393.

42. Svensson, L.G., E.H. Blackstone, and D.M. Cosgrove III, *Surgical Options in Young Adults with Aortic Valve Disease.* Current Problems in Cardiology, 2003. **28**(7): p. 417-80.

43. Puvimanasinghe, J.P.A., et al., *Comparison of Outcomes after Aortic Valve Replacement with a Mechanical Valve or a Bioprosthesis using Microstimulation.* Heart, 2004. **90**: p. 1172-1178.

44. Sidhu, P., et al., *Mechanical or Bioprosthetic Valves in the Elderly: A 20-Year Comparison.* Annals of Thoracic Surgery, 2001. **71**(5 Suppl): p. S257-260.

45. Kassai, B., et al., *Comparison of bioprosthesis and mechanical valves, a meta-analysis of randomized clinical trials.* Cardiovascular Surgery, 2000. **8**(6): p. 477-483.

46. Stelzer, P., *The Ross Procedure*. 2003.

47. *Coumadin*. 2002, Bristol-Myers Squibb Company.

48. Concha, M., et al., *The Ross Procedure.* Journal of Cardiac Surgery, 2004. **19**: p. 401-409.

49. Black, J., *Biological Performance of Materials*. 1999, New York: Marcel Dekker Inc.

50. Vyavahare, N., et al., *Mechanisms of bioprosthetic heart valve failure: Fatigue causes collagen denaturation and glycosaminoglycan loss.* Journal of Biomedical Materials Research, 1999. **46**: p. 44-50.

51. Sacks, M.S., *The biomechanical effects of fatigue on the porcine bioprosthetic heart valve.* Journal of long-term effects of medical implants, 2001. **11**(3&4): p. 231-247.

52. Conklin, L.D. and M.J. Reardon, *Technical Aspects of the Ross Procedure.* Texas Heart Institute Journal, 2001. **28**: p. 186-189.

53. Raja, S.G. and M. Pozzi, *Ross Operation in Children and Young Adults: the Alder Hey Case Series.* BMC Cardiovascular Disorders, 2004. **4**(3): p. 1-7.

54. Jaggers, J., et al., *The Ross Procedure: Shorter Hospital Stay, Decreased Morbidity, and Cost Effective.* Annals of Thoracic Surgery, 1998. **65**(6): p. 1553-1557.

55. Oury, J.H., A.C. Eddy, and J.C. Cleveland, *The Ross Procedure: A Progress Report.* The Journal of Heart Valve Disease, 1994. **3**(4): p. 361-364.

56. Gatzoulis, M.A., *Ross procedure: the treatment of choice for aortic valve disease?* International Journal of Cardiology, 1999. **71**: p. 205-206.

57. Stahle, E., *Ross Procedures in Adults - a Valid Option for Whom?* Scandinavian Cardiovascular Journal, 2002. **36**(5): p. 272-274.

58. Oswalt, J.D., et al., *Highlights of a Ten-Year Experience with the Ross Procedure.* Annals of Thoracic Surgery, 2001. **71**: p. S332-5.

59. Gulbins, H., E. Kreuzer, and B. Reichart, *Homografts: a Review.* Expert Reviews in Cardiovascular Therapy, 2003. **1**(4): p. 533-9.

60. Oury, J.H., et al., *The Ross Procedure: Current Registry Results.* Annals of Thoracic Surgery, 1998. **66**(6 Suppl): p. S162-5.

61. Turrentine, M.W., et al., *Biological versus Mechanical Aortic Valve Replacement in Children.* Annals of Thoracic Surgery, 2001. **71**: p. S356-60.

62. Takkenberg, J.J., et al., *Estimated event-free life expectancy after autograft aortic root replacement in adults.* Ann Thorac Surg, 2001. **71**(5 Suppl): p. S344-8.

63. Timoshenko, S. and J. Gere, *Mechanics of Materials*. 1972, New York: D. Van Nostrand. 552.

64. Wells, S.M. and M.S. Sacks, *Effects of fixation pressure on the biaxial mechanical behavior of porcine bioprosthetic heart valves with long-term cyclic loading.* Biomaterials, 2002. **23**(11): p. 2389-99.

65. Gloeckner, D., K. Billiar, and M. Sacks. *The bending behavior of fixed porcine aortic cusp*. in *Third World Congress of Biomechanics*. 1998. Hokaiddo, Japan.

66. Iyengar, A.K.S., et al., *Dynamic in vitro quantification of bioprosthetic heart valve leaflet motion using structured light projection.* Ann Biomed Eng, 2001. **29**(11): p. 963-73.

67. Lee, T.C., et al., *The effect of elastin damage on the mechanics of the aortic valve.* J Biomech, 2001. **34**(2): p. 203-10.

68. Yu, Q., J. Zhou, and Y.C. Fung, *Neutral axis location in bending and Young's modulus of different layers of arterial wall.* Am J Physiol, 1993. **265**(1 Pt 2): p. H52-60.

69. Vesely, I. and D. Boughner, *Analysis of the bending behaviour of porcine xenograft leaflets and of neutral aortic valve material: bending stiffness, neutral axis and shear measurements.* J Biomech, 1989. **22**(6-7): p. 655-71.

70. Talman, E.A. and D.R. Boughner, *Glutaraldehyde fixation alters the internal shear properties of porcine aortic heart valve tissue.* Annals of Thoracic Surgery, 1995. **60**: p. S369-S373.

71. Vesely, I., D.C. Casarotto, and G. Gerosa, *Mechanics of cryopreserved aortic and pulmonary homografts.* J Heart Valve Dis, 2000. **9**(1): p. 27-37.